Elastic and Inelastic Collisions in Ultracold and Astrophysical Environments

Marko Gacesa, Ph.D.

University of Connecticut, 2010

We explore collisions of atomic particles in two different regimes. In the first part of this work, we study atom-atom collisions of alkali metals at ultracold temperatures and conditions typically found in modern experiments. Feshbach resonances induced by external magnetic fields present a way to change collisional properties and exhibit control over cold collisions. We perform a fully quantum coupled-channel calculation in molecular orbital formalism to calculate collisional properties and characterize Feshbach resonances in ultracold Li+Na and Li+Rb systems. Furthermore, we use the results of these calculations as a foundation to propose a novel scheme for formation of stable ultracold molecules in their lowest rovibrational level. The formation scheme relies on the fact that the photoassociation rate becomes greatly enhanced in the vicinity of a Feshbach resonance, resulting in a large increase of the number of produced excited molecules. Efficient production of stable ultracold molecules is a prerequisite for realization of various proposed platforms for quantum computing with neutral atoms and molecules. In addition, we suggest a way to exploit specifics of the photoassociation rate behavior near its minimum for a precision measurement experiment to detect hypothetical variation of the electron-proton mass ratio in time.

The second part of this study examines ion-atom collisions in our solar system. Highly charged ions present in the solar wind collide with neutrals, capture one or more electrons into high excited states and deexcite, radiating energetic X-ray and UV photons. In particular, we study X-ray emissions charge-exchange collisions between fully stripped C^{6+}, N^{7+}, and O^{8+} solar wind ions and heliospheric hydrogen. We analytically solve the two-center Schrödinger equation and construct electronic potential curves for the aforementioned molecular ions. Subsequently, we compute polarization of the X-rays emitted in a single-step deexcitation following charge-exchange collisions and construct a polarization map for the ecliptic plane, as observed from Earth. Our analysis indicates that the heliospheric charge-exchange X-rays are slightly polarized, with the polarization P close to ten percent for the optimal line-of-sight.

Elastic and Inelastic Collisions in Ultracold and Astrophysical Environments

Marko Gacesa

B.S. Physics, University of Zagreb, Croatia, 2004

M.S. Physics, University of Connecticut, Storrs, CT, 2006

A Dissertation

Submitted in Partial Fullfilment of the

Requirements for the Degree of

Doctor of Philosophy

at the

University of Connecticut

2010

APPROVAL PAGE

Doctor of Philosophy Dissertation

Elastic and Inelastic Collisions in Ultracold and Astrophysical Environments

Presented by

Marko Gacesa, B.S. Phys., M.S. Phys.

Major Advisor

Robin Côté

Associate Advisor

Vasili Kharchenko

Vasili Kharchenko

Associate Advisor

William C. Stwalley

William C. Stwalley

University of Connecticut

2010

to Isaac Asimov and Gene Roddenberry for inspiration,

Εμπεδοκλη̃ζ and Paracelsus for striking the foundation

ACKNOWLEDGEMENTS

Many people supported me in various ways during my years at UConn. First, I would like to thank Robin Côté for offering me an opportunity to work in his group, as well as his guidance, ideas and discussions, and the friendly and easy going approach that created a really pleasant working environment. I can only hope that I have managed to absorb at least some aspects of his approach to physics, and that I will be able to apply it someday myself.

Bill Stwalley was the first AMO physicist whom I met when I came to UConn. He was my advisor during my first year, and he was kind enough to let me participate in his group's discussions since. I was impressed by the breadth of his knowledge of atomic and molecular physics, which commonly materialized as his ability to point out to me the connections between what it seemed like completely different topics. I am very grateful for this extra insight into problems, as well as for the advising role that Bill played later.

I would also like to thank Vasili Kharchenko for inviting me to work on an interdisciplinary project on the intersection of atomic physics and astrophysics, as well as for his advices and help along the way. Being trained partly as an astrophysicist myself, I have enjoyed working on the project and learned a lot from Vasili about the field of space physics and the role that atomic physics plays in it.

Michael Rozman was in charge of leading a group of linux system administrators at the physics department. Several years I had been a member of the sysadmin group, at first to fulfill my assistantship duties and later to keep up with current happenings in the linux world. We helped maintain the department's computer system, but also worked on very interesting computer-related projects and I thank Michael, Richard Jones and other linux gurus for sharing their knowledge and tricks.

Help that I received from the graduate students and postdocs who overlapped with me in Robin's group has been significant. Philippe Pellegrini, who joined Robin's group a few months before me as a postdoc, taught me a lot about computational aspects of the AMO physics, as well as how to start with an abstract theory and obtain results that could be compared to an experiment. Later, that role was supplemented by the one of a good friend, with whom I enjoyed discussing physics, philosophy and random things, not necessarily in that order, in the place called Ted's. I am grateful for having a chance to work, and share common frustrations regarding numerics, codes, and a few other things, with the other members of Robin's group, Beth Taylor-Juarros, Ionel Simbotin, Jovica Stanojevic, Zoran Pavlovic, Nolan Samboy, Jason Byrd, Sandipan Banerjee, Elena Kuznetsova, Subhas Ghosal, and Diego Valente. All of them remain in my mind inseparable from the entire experience of being a graduate student at UConn.

In particular, I learned much from Ionel, whose understanding of collisional physics and scattering theory was at a level well above that of an average graduate student. Jason joined the group several years after me and immediately started working on structure calculations. We often discussed various computer-related topics, including the computational aspects of ab-initio calculations, occasionally combined with a digression to *EVE*. Jason calculated molecular potentials for several diatomic and molecule-molecule systems that we were trying to describe and the capability to do so in-house proved really useful.

Beth was already a senior graduate student when I joined Robin's group, and I am thankful to her for the fact that she was willing to share some of her experiences, which later helped me with some of the non-research aspects of graduate school. Subhas joined Robin's group after Philippe left, about a year after Lena, both as postdocs. I had a good and productive time working with them. Lena was a quantum optics theorist, and as we worked together on two projects related to quantum computation with neutrals, I was trying to learn more about the qubits and quantum computers while calculating the cross sections. Unfortunately, we did not overlap much since she was mostly situated at the ITAMP in Cambridge at that time. On the other hand, I helped Subhas to perform a full time-dependent calculation of Feshbach-optimized photoassociation rates, as an extension of our previous work. I am grateful to him for his keen eye for details and the home-made Indian food.

My friends, some of them graduate students themselves, made my time in grad school more enjoyable, and without them the time spent here would have felt much longer and lonelier. In particular, I would like to thank Ken and Elly, Marco and Erin, Adolfo, Li Fang, Yifei, Kuang He, Jimmy James, Sam, Franz, Javier, Otim, Kalum, Andrew, Ila, Marek, Dajun, John Haga, Renuka, and Selini.

On a more personal note, I am indebted to my partner Jadranka for her love and support.

Finally, I would like to thank my family for their encouragement and understanding. My parents, Miro and Anci, instilled me with their creativity, optimism, and moral values that helped to shape me into an individual that I have become. I am certain that without their influence and emotional support I would not have been set on this path.

TABLE OF CONTENTS

LIST OF FIGURES

LIST OF TABLES

Chapter 1

Introduction

Collisions have occupied a central place in physics since its early days and much of our understanding of fundamental particles and their interactions has been derived from scattering experiments. While the hypothesis of "fundamental indivisable particles," or atoms, existed from the ancient times, the first conclusive experiments which related macroscopic and microscopic physics were conducted by Bernoulli (1739). Even though Boyle (1662) and Mariotte (1667) found the relation between the pressure and volume of a gas, Bernoulli was most likely the first person to realize that the pressure of a gas was a collective net effect of collisions between the "gas particles" and the container. In the second half of the nineteenth century the kinetic theory of gases was developed by, among others, Maxwell, Boltzmann, Krönig and Clausius, who strived to find general laws applicable to all gases. They based the theory on a concept that all physical parameters of a gas such as energy, momentum and mass move around within the gas because of particle collisions which occur at an averaged velocity based on the statistical distribution of the sample (Maxwell treated the particles as rigid classical "billiard balls"). Successes of classical kinetic theory in predicting macroscopic behavior of gases were also a confirmation that underlying assumptions, including the mechanism of particle collisions, were correct. Later, deviations from the theory for real gases were observed, only to be resolved by the quantum theory.

With the development of quantum mechanics and atomic theory, the rich structure of atomic particles was revealed and treatment of atomic collisions became a much more complex problem than envisioned by the pioneers of kinetic theory of gases. Notable triumphs of scattering theory in the early twentieth century include work of Ernest Rutherford (1911). He is perhaps best known for the Gold foil experiment, where he deduced the orbital model of the atom, with electrons orbiting around the positively charged nucleus, by observing the distribution of scattered alpha particles off thin gold foil. Soon after Niels Bohr combined the results of Rutherford's experiment with his own quantum theory of light and derived a theory of hydrogen atom, advancing atomic physics and physics in general into the modern era.

Discussing "collisions in physics" is almost meaningless in modern physics: the topic is simply too broad and spans over different areas of physics and energy scales. In fact, different collisional energies emphasize different physics and require different models. In this work, we will narrow down the topic to two specific topics: the ultracold collisions of atoms and ion-atom charge-exchange collisions at non-relativistic energies.

1.1 Ultracold collisions

Not so long ago, pioneering work by J. Dalibard and C. Cohen-Tannoudji (1985) [1,2] and W. D. Phillips, J. V. Prodan and H. J. Metcalf [3], demonstrated that light can be used to trap and cool atoms to submilliKelvin temperatures, initiating a shift towards atomic and molecular physics at ultracold temperatures. As new phenomena, such as Bose-Einstein (BEC) condensation, matter-wave coherence, Efimov states and Fermi degenerate gases, were subsequently explored, collisions maintained a central role. In a more recent review article [4] Weiner, Bagnato, Zilio and Julienne state:

> "Cold and ultracold collisions occupy a strategic position at the intersection of several powerful themes of current research in chemical physics, in atomic, molecular and optical physics, and even in condensed matter."

This statement is certainly true, if not too broad. Perhaps the first direct consequence of this effect that comes to mind in the domain of ultracold physics is Bose-Einstein condensation. Namely, to cool an atomic gas to the temperature at which it undergoes the Bose-Einstein condensation, we must utilize evaporative cooling in addition to laser cooling [5]. The reason is simple: the momentum transfer achieved by laser light in a trap during the optical cooling cycle can greatly reduce translational motion of the atoms but it cannot maintain the required phase space density for condensation. To perform the evaporative cooling the atoms are loaded into an approximately harmonic magnetic trap and its potential is lowered using a radio-frequency field, which removes the hottest atoms, while the rest of the sample thermalizes via elastic collisions. However, "unfavorable" collisions heat the trapped gas, ejecting pairs of atoms from the shallow magnetic trap. Such collisions are the main factor in determining the sample's maximum lifetime in a trap. The s-wave two-body scattering length plays a crucial role during the condensation as well as in determining the condensate's properties [6]. Its sign determines if the gas can be cooled beyond the optical limit and condensed, while modern mean-field theories, which predict the condensate's lifetime, size and dynamics, as well as kinetic theories that describe formation of the condensate, base the interaction term on the atom-atom scattering length a. A good overview of existing BEC theories is given in [7].

Another important aspect of particle collisions at ultracold temperatures is the study of weak long-range forces. Atomic collisions at ultracold temperatures happen very slowly. This allows very long interaction times during a collision. Weak long-range forces acting between the atoms, such as the electric dipole-dipole interaction, that are usually negligible can become very important. Consequently, this makes ultracold collisions an ideal system to study such forces. External electromagnetic fields introduce additional couplings between atoms and can be used both to study atomic or molecular structure and to control the outcome of collisions. Perhaps the best known example of the latter is the application of the magnetic field to induce a Feshbach resonance and modify the scattering length [8]. This is, in principle, possible to realize in all systems where the average collision energy of atoms is not greater than a few percent of the atomic hyperfine splittings. Magnetic Feshbach resonances have been used in numerous experiments and remain a tool of choice in the experiments where either enhancing the elastic collision rate [4], or tuning a BEC [9] are required.

Photoassociation spectroscopy of ultracold molecules has been a particularly successful tool for conducting such studies experimentally [10–12]. Photoassociation is a process where a bound rovibrational molecular state is excited by a laser which is resonant with a lower-energy molecular state that becomes accessible during the collision of two atoms. The low energies at which the collision takes place make it possible to resolve the rotational spectra in a very high resolution often comparable to the natural linewidth. If the wavefunctions of the initial and photoassociated state overlap favorably (have large Franck-Condon factors), the process is very efficient. In addition, photoassociation can be used to create molecules in their ground state [13]. This usually requires two steps, where molecules are first formed in an excited state and then transferred to the ground state via either spontaneous or stimulated emission. For example, the stimulated Raman process has been used successfully to produce RbCs [14,15] and KRb [16,17] molecules in their lowest rovibrational level, and its application to other heteronuclear alkali molecules is currently being investigated.

Forming ultracold molecules in their lowest energy rovibrational state is not only interesting for spectroscopic measurements. Such molecules are long-lived and stable in traps, which makes them suitable for realizing qubits and quantum gates [18,19]. The possibility of using ground-state ultracold molecules as a platform for quantum computation, especially when combined with optical lattices and methods to address individual lattice sites [20], opened up a new and exciting venue for research. Moreover, speaking of 'forming molecules' evokes the basic idea of chemistry, and, indeed, a subset of atomic physicists and physical chemists investigate chemical reactions in ultracold gases and how to control them by electromagnetic fields (see *e.g.*, Refs. [21,22] and references therein). These topics constitute some of the mainstream research directions in ultracold atomic and molecular physics that are closely related to the research presented in this thesis. For a more complete overview of current developments in the field, however, we point the reader to the review articles referenced above. In particular, a good overview of directions and future applications (some of which have already been realized!) of ultracold molecules is given in Ref. [12].

1.2 Ion-atom charge-exchange collisions in space

While ion-atom collisions and charge exchange are being actively investigated in the ultracold regime [23–25] (and references therein), this is not the topic of our research. Instead, we apply the same underlying scattering theory to study a much 'hotter' system: charge-exchange between solar wind ions and neutral atoms in our solar system (or, more generally, the circumstellar space). In this context, we will call such an environment 'cold,' to respect the jargon used in astrophysical literature. It was a surprise to observe that such a cold environment emits in UV and X-ray spectrum. Such energetic radiation is expected from very hot and violent systems, such as neutron stars, binary stars, supernova remnants or black holes.

Let us present a bit of history. The first observation of X-ray and EUV emission from a comet (Hyakutake, C/1996 B2) was made in March 21-24, 1996 by Krasnopolsky and Mumma with the Extreme Ultraviolet Explorer (EUVE) satellite [26]. A follow up observation by ROSAT confirmed that the comet was, indeed, a source of X-rays [27]. Charge-exchange collisions between highly-charged solar wind heavy ions and neutral atoms and molecules present in the cometary atmospheres were first proposed as a possible mechanism responsible for the X-ray emission by Cravens [28]. Subsequent studies confirmed the radiative cascade produced by the captured electron from excited states of solar wind ions as the mechanism responsible for the process [29]. As better observational data became available, it became possible to identify structures in the observed spectra, confirming the charge-exchange hypothesis. Currently, it is believed that charge-exchange is responsible for close to 90% of cometary X-ray and EUV emissions

[30,31] in our Solar system. Soft X-rays below 2 keV and EUV emissions were also detected from the majority of cold solar system objects including planets and planetary satellites, the Io plasma torus, the rings of Saturn, the exospheres of Earth and Mars, and the heliosphere [32].

The role played by charge-exchange processes in the interaction of the solar wind with the interstellar medium [33–35] has also been studied recently. There is an increasing amount of evidence that the existing models of the hot Local Bubble may need revision to correctly account for the charge-exchange radiation [36,37]. These exciting discoveries encouraged us to explore the role of polarization in charge-exchange X-ray emissions.

1.3 Organization of this work

This thesis is organized as follows. In the four chapters following the introductory chapter the focus is on collisions of atomic pairs at ultracold temperatures in an external magnetic field. In Chapter 2, we review the coupled-channel theory of cold collisions in a magnetic field and introduce the notation that will be used throughout the thesis. In Chapter 3 we present a detailed theoretical study of collisional properties of ultracold Li-Na and Li-Rb mixtures. To ensure that our calculations are accurate, we first construct new molecular potentials that can reproduce published experimental and theoretical results. In the next step, we calculate properties of Feshbach resonances, scattering lengths and inelastic rates.

A new efficient method for forming ultracold molecules is proposed in Chapter 4 and applied to the previously studied systems. The method exploits the properties of the atom-atom scattering wavefunction near a Feshbach resonance to enhance molecular photoassociation rates. In Chapter 5, based on a special property of the enhanced formation rate derived in Chapter 4, we propose a precision measurement experiment to detect variation of electron-proton mass in time. Chapter 6 briefly describes a theory of charge-exchange atom-ion collisions. A special attention is given to exactly solvable three-particle systems and electronic potentials for CH^{6+}, NH^{7+} and OH^{8+} molecular ions are calculated from first principles. In Chapter 7 we calculate the polarization of X-rays emitted in charge-exchange collisions that take place in our solar system, between characteristic solar wind ions and hydrogen. We conclude in Chapter 8, by emphasizing the most important results of these projects and discussing future directions.

Chapter 2

Theory of ultracold two-body collisions

Scattering theory is a mature and established theory presented in detail in numerous specialized textbooks, such as Refs. [38–40]. Therefore, only an overview relevant to the study of atomic collisions in external fields is presented here. While the general expressions given in this chapter are valid for a broad range of energies, the emphasis is on the atom-atom collisions in the ultracold regime. Moreover, the majority of the final expressions are presented in a form in which they can be directly applied. In addition, instead of introducing the theory from a more general Lippmann-Schwinger operator formalism, we choose the Schrödinger differential equation as the starting point. Such presentation most certainly lacks the beauty and generality of a more abstract theory but remains more in line with the majority of articles in current prime literature in atomic and molecular physics. The last two references cited, however, offer such an approach, and we refer the interested reader to them for a more complete picture.

2.1 Two-body multichannel scattering

A collision of two atoms can be described as an extension of a free particle theory where an interaction potential corresponding to all the Coulombic interactions of the component particles is introduced and its effects on the free particle wavefunction are studied. We start from the time-independent Schrödinger equation

$$H|\Psi\rangle = E|\Psi\rangle, \tag{2.1.1}$$

where H is the total Hamiltonian for the system, E is the eigenenergy, and $|\Psi\rangle$ is the two-particle quantum state of interest.

In a general case, we consider two colliding atoms, labeled a and b, to be structureless particles connected by a vector $\vec{R} = \vec{r}_a + \vec{r}_b$ and moving with relative momentum $\vec{k}$ in the scattering potential $V(\vec{R})$. We will assume that the scattering potential depends only on the relative position of the colliding particles and that the total wavefunction Ψ can be separated in two parts. The first part describes the center-of-mass motion and second part describes the relative motion of the atoms.

This model is valid both in free space or if an external trapping potential is present. To justify that, we take a closer look at the trapping potential and relevant length scales. A typical trapping potential can be described well by a harmonic potential of the form $V = \frac{1}{2}m\omega^2R^2$, where m is the mass of the atoms in the center-of-mass coordinate system and ω is the angular frequency of the trapping field. This potential is quadratic in R and still separable, while anharmonic terms proportional to R^3 and higher order powers are typically at least two orders of magnitude weaker than the leading terms and can therefore be neglected.

We can now rewrite Eq. (2.1.1) in a more specific form

$$\left(-\frac{\hbar^2}{2\mu}\nabla^2 + H_{\text{int}} + V(R)\right)|\Psi\rangle = E|\Psi\rangle, \tag{2.1.2}$$

where the term H_{int} contains the internal energy of the molecule and interaction with external fields and E is the energy associated with the *relative* motion of the colliding particles.

A multichannel approach is usually required because of the internal degrees of freedom which can be excited, leading to a different outcome of the collision. We first write the multicomponent scattering state for the relative motion in terms of the incident plane wave and the scattered spherical wave:

$$|\Psi_m\rangle = e^{i\vec{k}_m\cdot\vec{R}}|\chi_m\rangle + \sum_n \frac{e^{i\vec{k}_n\cdot\vec{R}}}{R} f_{mn}(\vartheta,\varphi)|\chi_n\rangle. \tag{2.1.3}$$

Here, $|\chi_m\rangle$ is the internal state of both particles, f_{mn} is the scattering amplitude, m is the incident state and n is the final state after the collision. The collision is considered elastic if the initial and final states remain the same $(m = n)$, and inelastic if they change in collision $(m \neq n)$.

We can perform a partial wave expansion of $e^{i\vec{k}\cdot\vec{R}}$ into spherical harmonics to account for the orbital motion of the colliding atoms and the corresponding angular degrees of freedom. The resulting expression is

$$|\Psi_i\rangle = \frac{1}{R}\sum_f \psi_f^{(i)}(R) Y_{\ell_f}^{m_f}(\vartheta,\varphi)|\chi_{n_f}\rangle, \tag{2.1.4}$$

where $\psi_f^{(i)}(R)$ is a radial wavefunction for the channel f obtained as the ith solution to Eq. (2.1.2). Here we introduced the concept of a *channel* by forming a combination of an internal state $|\chi_{n_f}\rangle$ with a specific spherical harmonic $Y_{\ell_f}^{m_f}(\vartheta,\varphi)$. The internal state can consist of any number of quantum states depending on the system, such as spin, hyperfine structure, and other pairwise interactions. The channel index f is unique and includes *all* quantum numbers for the particular combination of angular and internal states. A frequently used notation in terms of channels present in collisions of two atoms is $|f_1 f_2\rangle$, where $|f_i\rangle = |\chi_{n_{f_i}}\rangle|\ell m_\ell\rangle_{f_i}$, includes all quantum numbers for the i^{th} atom, where $i = 1, 2$. This notation is, clearly, not uniquely defined: depending on symmetries relevant for the problem, different definitions of channel index are possible. By solving the equation

$$H_{\text{int}}|\chi_{n_f}\rangle = E_k|\chi_{n_f}\rangle, \tag{2.1.5}$$

we can obtain E_k, the threshold energy for a linear combination of internal states (minimum one) that diagonalize the Hamiltonian H_{int}. Channels can have different threshold energies E_k, and the difference between the collision energy $E - E_k$ can be positive or negative. For $E - E_k \geq 0$ the channel is *open* and accessible in collision while for $E - E_k < 0$ the channel is *closed.* We also define the channel wavenumber $k_f = \sqrt{2\mu(E - E_f)}$ for the channel f. If an external field is included in the H_{int} and it changes the threshold energy, we call the set of states that corresponds to that particular energy "field dressed." Field-dressing can be induced by static electric or magnetic fields, as well as by an optical pulse; it represents a useful formalism for visualizing effects of the fields on the system.

Inserting the partial wave expansion given by Eq. (2.1.4) into Eq. (2.1.2) and projecting the resulting equation onto $\langle \phi_{f'} | = \langle Y_{\ell'_{k'}}^{m'_{f'}} \chi_{n'_{f'}} |$ gives an infinite set of coupled differential equations

$$\sum_f \left[\delta_{fi} \left(-\frac{\hbar^2}{2\mu} \frac{\partial^2}{\partial R^2} + \frac{\hbar^2 \ell_f (\ell_f + 1)}{2\mu R^2} - E + E_f \right) + V_{fi}(\vec{R}) \right] \psi_f^{(i)} = 0. \qquad (2.1.6)$$

Here, δ_{fi} is Kronecker's delta and $V_{fi}(R) = \langle \phi_{f'} | V(R) | \phi_f \rangle$ is the interaction potential which will be analyzed in detail in specific cases in Chapter 3. We will use the convention that the i^{th} entrance channel is associated with the i^{th} eigenenergy.

Before this system of coupled-channel equations can be solved, the total number of equations has to be reduced from an infinite number to the minimum number required to describe the physical behavior of the system and capture all interesting effects. Depending on the complexity of the system and the level of detail required, the number of equations can vary between a minimum of two and several thousand. Once obtained, the system of equations is solved numerically using either a multichannel propagator method or a spectral method. Numerical techniques are discussed in more detail below.

In the ultracold regime, at or below a few milliKelvin, the s-wave scattering almost completely determines the outcome of the collision. In practice, there is rarely a need to consider more than the first four partial waves. This greatly reduces the number of coupled equations and simplifies the problem. At the same time, the complexity of the problem increases elsewhere: cold collisions are very slow and sensitive to the weak and long-range internuclear forces.

To obtain a meaningful solution of the Eq. (2.1.6), we need to apply the following boundary conditions

$$\begin{aligned} \psi_f^{(i)}(R=0) &= 0, \\ \psi_f^{(i)}(R\to\infty) &= \sqrt{\frac{2\mu}{\pi\hbar^2 k_i}}\left(\frac{e^{-i(k_iR-\ell_i\pi/2)}\delta_{fi} - e^{i(k_iR-\ell_i\pi/2)}S_{fi}}{2i}\right), \end{aligned} \quad (2.1.7)$$

with $k_i = \sqrt{2\mu E_i/\hbar^2}$, and S is the scattering S-matrix [39]. The S-matrix contains information about both the scattered and the unscattered part of the wavefunction, and all physical observables measured in experiments can be expressed in terms of it.

The boundary conditions can be used in Eq. (2.1.6), which is then solved for S_{fi}. Another important operator matrix in scattering theory is the T-matrix, or transfer matrix, which is defined as [41]

$$T_{fi} = i(S_{fi} - \delta_{if}). \quad (2.1.8)$$

While both S-matrix and T-matrix operators can be used when solving a collisional problem, their physical interpretation is different. The S-matrix operator acts on an incoming state and propagates it

$$\hat{S}|\psi_0\rangle = |\psi_0\rangle + |\psi_{\text{scat}}\rangle, \quad (2.1.9)$$

so that the final state can be written in terms of the incident and scattered waves, $|\psi_0\rangle$, and $|\psi_{\text{scat}}\rangle$, as in Eq. (2.1.3). In general, the S-matrix is complex. Consequently, in practical calculations involving inelastic collisions, it is commonplace to work with the K-matrix, which is real-valued [39]. Similarly, the T-matrix operator acts on the incident wave and propagates it but it accounts only for the scattered fraction of the total wavefunction

$$\hat{T}|\psi_0\rangle = -i|\psi_{\text{scat}}\rangle. \tag{2.1.10}$$

In a multichannel collision the partial scattering cross section from an incoming channel i scattered to a channel f can be expressed in a simple form using the T-matrix:

$$\sigma_{fi} = \frac{\pi}{k_i^2}|T_{fi}|^2. \tag{2.1.11}$$

More specifically, σ_{fi} describes the ratio of the incident flux in channel i to the scattering flux in channel f, where the flux is usually defined per unit area. In binary collisions σ_{fi} can also be interpreted as a probability that the incoming particle in the initial state i will exit the collision in the state f. This is often expressed using the rate constant defined as

$$K_{if} = v_i\sigma_{fi} \tag{2.1.12}$$

where v_i is the initial velocity of the colliding particles.

More insight into the problem can be gained by rewriting the asymptotic boundary conditions given in Eq. (2.1.7) in terms of real-valued spherical Bessel functions and the K-matrix for large R. We have

$$\psi^{(i)}(R \to \infty) \propto \sum_f k_f R \left(j_{\ell_f}(k_f R)\delta_{fi} - n_{\ell_f}(k_f R) K_{fi} \right), \tag{2.1.13}$$

where the spherical Bessel functions are proportional to the solution of Eq. (2.1.6) for $V_{fi} = 0$:

$$\begin{aligned} \langle R|\psi_f^{(i)}\rangle &\propto k_f R \, j_{\ell_f}(k_f R) \\ &\propto k_f R \, n_{\ell_f}(k_f R), \end{aligned} \tag{2.1.14}$$

Here j_ℓ is regular and n_ℓ irregular spherical Bessel function. The K-matrix is real-valued and often more practical to use than the S-matrix or the T-matrix when numerically solving a coupled-channel scattering problem. For the large argument, spherical Bessel functions behave as simple trigonometric functions

$$\begin{aligned} j_{\ell_f}(k_f R) &\propto \frac{1}{k_f R} \sin(k_f R - \ell_f \pi/2) \\ n_{\ell_f}(k_f R) &\propto \frac{1}{k_f R} \cos(k_f R - \ell_f \pi/2). \end{aligned} \tag{2.1.15}$$

Substituting these solutions in Eq. (2.1.13) and using trigonometric identities results in the following expression for the channel i

$$\psi_i^{(i)} \sim \sin(k_i - \ell_i \pi/2 + \eta_i). \tag{2.1.16}$$

The resulting equation introduces the *scattering phase shift* η_i for the channel i for the diagonal terms K_{ii} of the K-matrix. A different manipulation of trigonometric identities transforms Eq. (2.1.16) into

$$\psi_i^{(i)} \sim \cos\eta_i \left[\sin(k_i - \ell_i \pi/2) + \tan\eta_i \cos(k_i - \ell_i \pi/2) \right], \tag{2.1.17}$$

which clearly shows the relation between diagonal K-matrix elements, K_{ii}, and the tangent of the phase shift, $\tan\eta_i$, a result that can be easily derived for a single-channel elastic scattering problem in one dimension. Partial cross section can also be related to the phase shifts as

$$\sigma_{ii} = \frac{4\pi}{k_i^2}\sin^2\eta_i. \tag{2.1.18}$$

Finally, to account properly for energetically closed channels, we need to introduce a different boundary condition. The channel f is closed if $E - E_f < 0$, resulting in an imaginary solution for k_f. To obtain the wavefunction in real space we need to impose an exponentially decaying boundary condition for large R in this channel. The closed-channel wavefunction has the form

$$\psi_f^{(i)}(R \to \infty) \propto e^{-k_f R}. \tag{2.1.19}$$

The required boundary condition for the channel f is constructed as a linear combination of other open- and closed-channel solutions.

2.2 Feshbach resonances

A quasibound state or resonance occurs when the energy in an open channel (above the continuum) is close to or matches the energy of a bound level, or at which a bound level could have occurred. In a single-channel case such a scenario is possible if a potential barrier exists, leading to shape resonances [41]. A Feshbach resonance occurs in a multichannel case when weak coupling exists between the open and closed channel. To illustrate this we consider a two-channel system with coupling $V_{12} = V_{21}$ (required condition to retain hermicity of the Hamiltonian) and rewrite Eq. (2.1.6):

$$\begin{aligned}\left(-\frac{\hbar^2}{2\mu}\frac{\partial^2}{\partial R^2} + V_1(R)\right)\psi_1(R) + V_{12}(R)\psi_2(R) = E\psi_1(R),\\ \left(-\frac{\hbar^2}{2\mu}\frac{\partial^2}{\partial R^2} + V_2(R)\right)\psi_2(R) + V_{21}(R)\psi_1(R) = E\psi_2(R).\end{aligned} \tag{2.2.1}$$

We assume that channel 1 is open, with the threshold energy $E = 0$, channel 2 is closed, and that E_0 is the energy of the resonant bound state with corresponding wavefunction ψ_0. These coupled equations can be formally solved using the Green's function method [41].

We obtain the position and the *additional phase shift in the open channel* that define the resonance, E_R and δ:

$$\begin{aligned}E_R &= E_0 + \Delta,\\ \delta &= -\arctan\left(\frac{\Gamma/2}{E - E_R}\right),\end{aligned} \tag{2.2.2}$$

where Δ is the energy shift of the resonance from E_0, the energy of the uncoupled bound state in the closed channel, and Γ is the width of the resonance:

$$\begin{aligned}\Delta &= \langle\psi_0|V_{21}\hat{G}V_{12}|\psi_0\rangle,\\ \Gamma &= 2\pi|\langle\psi_0|V_{21}|\psi_{\text{reg}}\rangle|^2.\end{aligned} \tag{2.2.3}$$

Here, $\hat{G}$ is the Green's operator and ψreg is the regular solution to the corresponding homogeneous differential equation [41]. These parameters are related:

the width of the resonance is determined by the energy Γ so that the phase δ increases by $\pi/4$ and $3\pi/4$ for $E = E_R - \Gamma/2$ and $E = E_R + \Gamma/2$ respectively.

The scattering length in the vicinity of a Feshbach resonance can be parametrized as [42]

$$a = a_{\mathrm{bg}}\left(1 - \frac{\Gamma}{E - E_R}\right). \tag{2.2.4}$$

Both Γ and E_R are, in fact, energy dependent since the Green's function for the problem is a function of energy. Nevertheless, the definitions given above are commonly used in the literature related to diatomic ultracold collisions [4]. A more detailed approach includes analysis of the pole structure of δ and its dynamics as a function of energy [39,40]. In a multichannel system with weak couplings between channels, such as in atomic collisions in the presence of external fields, more than one Feshbach resonance often exists and their parameters are calculated by completely solving the scattering problem, a task typically accomplished numerically.

The effect of external fields, namely a constant magnetic field, on the resonances is discussed below and in subsequent chapters Feshbach resonances are calculated for several alkali metal atom pairs.

2.3 Angular momentum representations

The time-independent formalism used to treat atom-atom collisions is similar to the one used to describe physics of diatomic molecules. In both cases, to model the problem correctly, we need to choose an appropriate set of quantum numbers, while keeping in mind that two different coordinate systems can be used, the molecule-fixed coordinates and the fixed laboratory coordinates. One of the consequences is that several different sets of quantum numbers are used, based on the relative importance of the interaction terms and the regime that is being described. Hund's cases [43] give very good guidelines for typical cases considered.

We consider a collision (or a diatomic molecule) ab, where a and b are two atoms. For the purpose of describing the theory, we will assume that the atoms are distinguishable; the symmetrization of the wavefunction to correctly account for (in)distinguishable particles is discussed in detail in a separate section below. A detailed description of angular momenta and different coupling schemes for diatomic systems is given by Lefebvre-Brion and Field [43]. For the purposes of this work, we will restrict ourselves to commonly used angular momentum representations and corresponding quantum numbers relevant in the ultracold regime.

One possible representation is the *short-range representation*, where we consider Born-Oppenheimer molecular potentials to be the dominant part of the interaction. We have

$$(\text{angular part})_{\text{short range}} \equiv |Sm_S, Im_I\rangle|\ell m_\ell\rangle, \tag{2.3.1}$$

where $\vec{S} = \vec{s_a} + \vec{s_b}$ and $\vec{I} = \vec{i_a} + \vec{i_b}$ are the total electronic and nuclear spin, respectively, $\vec{\ell}$ is the total orbital angular momentum as defined above, and m_α

is the projection of the quantum number α on the space-fixed quantization axis. This representation is suitable for small internuclear separations where the Born-Oppenheimer potentials are diagonal in a total electronic spin basis. Spectroscopic notation at short range is based on this representation and identifies molecular potentials as singlet or triplet, based on the total electronic spin.

For large internuclear separations small corrections to molecular potentials due to the hyperfine interactions and interactions with external fields become important. Different angular momentum representations that include the total quantum number f for the atom i ($i = \{a, b\}$) become better suited for diagonalizing the Hamiltonian. One such representation is the *uncoupled hyperfine representation*

$$(\text{angular part})_{\text{uncoupled}} \equiv |f_a m_{f_a}, f_b m_{f_b}\rangle |\ell m_\ell\rangle, \tag{2.3.2}$$

where the hyperfine quantum number for the atom i ($i = \{a, b\}$), is $\vec{f}_i = \vec{s}_a + \vec{i}_a$. In the absence of external fields the hyperfine Hamiltonian can be expressed in a simpler form in the *coupled hyperfine representation* given by

$$(\text{angular part})_{\text{coupled}} \equiv |(f_a f_b) f m_f\rangle |\ell m_\ell\rangle. \tag{2.3.3}$$

This representation is also useful if the external magnetic field can be treated as a small perturbation. If the dipole-dipole interaction term is included, the fully uncoupled angular momentum representation can be used since the total

Hamiltonian is block diagonal in it. This basis is defined as

$$(\text{angular part})_{\text{fully uncoupled}} \equiv |s_a m_{s_a} i_a m_{i_a}\rangle |s_b m_{s_b} i_b m_{i_b}\rangle |\ell m_\ell\rangle. \tag{2.3.4}$$

In this thesis the uncoupled hyperfine representation is used when describing general properties of systems, while we use the short range representation in conjunction with the Feshbach projection formalism. The fully uncoupled representation is used to calculate magnetic dipole-dipole matrix elements and other second-order effects with similar tensorial character.

2.3.1 Identical particles and symmetrization

The symmetrization postulate of quantum mechanics states that particles with spin equal to an integer multiple of $\hbar$ (bosons) can have only symmetric states, while the particles with spin equal to a half odd-integer multiple of $\hbar$ (fermions) can have only antisymmetric states. A third type of symmetry or partial symmetry states does not exist in nature [44]. Consequences of the symmetrization postulate are, among others, the Pauli exclusion principle and the indistinguishability of scattering events for identical particles. To account for the latter we need to allow the spatial wave function to be symmetric or antisymmetric under particle exchange ($\vec{r} \longrightarrow -\vec{r}$).

The total two-particle wavefunction must be symmetrized with respect to the exchange of internal atomic coordinates and spatial inversion of the coordinate system. This can be accomplished by applying the two-particle symmetrization operator $\hat{O} = (1 + (-1)^p P_{12})$ to the total wavefunction, where $(-1)^p$ is the phase factor with $p = 0$ for bosons and $p = 1$ for fermions. The radial part of the wavefunction is trivially symmetric since it is a function of the internuclear distance (spatial coordinate) R. The remaining angular and spin parts, $|\ell m_\ell\rangle|f m_f\rangle = Y_\ell^{m_\ell}(\vartheta, \varphi)\chi_f$, contain all the information about the symmetry of a particular state. In the center-of-mass frame the symmetrization operator for the angular part of the wavefunction is equivalent to the parity operator P_{12}, which can be applied to it resulting in

$$P_{12}|\ell m_\ell\rangle = (-1)^\ell |\ell m_\ell\rangle. \tag{2.3.5}$$

Using the angular momentum representations introduced in the previous section we can proceed with the symmetrization. This is illustrated in the uncoupled hyperfine representation. We apply the total symmetrization operator $\hat{O}$ to the angular part of the wavefunction given in Eq. (2.3.2):

$$\hat{O}|f_a m_{f_a}, f_b m_{f_b}\rangle|\ell m_\ell\rangle = |f_a m_{f_a}, f_b m_{f_b}\rangle|\ell m_\ell\rangle + (-1)^{p+\ell}|f_b m_{f_b}, f_a m_{f_a}\rangle|\ell m_\ell\rangle \tag{2.3.6}$$

The symmetry of the coupled hyperfine representation can be easily derived from the obtained expression by recoupling hyperfine components of the angular momenta and by using the identity relation for the 3-j coupling coefficients [45].

The resulting expression is

$$\begin{aligned}\hat{O}|(f_a f_b) f m_f\rangle|\ell m_\ell\rangle &= |(f_a f_b) f m_f\rangle|\ell m_\ell\rangle + \\ &\quad (-1)^{p+\ell+f_a+f_b-f}|(f_b f_a) f m_f\rangle|\ell m_\ell\rangle.\end{aligned} \tag{2.3.7}$$

We can obtain selection rules directly from symmetrized expressions. If the spin part of the total wavefunction is indistinguishable, it follows from Eq. (2.3.6) that the collision of the identical atoms is permitted only if $(-1)^{p+\ell} = 1$. This implies that only even (odd) partial waves need to be considered for bosons (fermions), simplifying the problem significantly. From the symmetrized coupled hyperfine representation given in Eq. (2.3.7) we can obtain selection rules by setting $f_a = f_b$. Detailed derivations of symmetrized representations and a more complete list of selection rules is given in Ref. [46].

2.4 Two-body Hamiltonian

In general, the total Hamiltonian for a two-atom collision is rather complicated. A detailed derivation of the exact Hamiltonian in the molecule-fixed coordinate system is given in Ref. [47]. The problem can be simplified without a significant loss of accuracy by decoupling nuclear and electronic motion and neglecting all couplings between them. This is called the Born-Oppenheimer approximation [48], and it is made possible because we can separate the much faster electronic motion from the slower nuclear motion during a non-relativistic collision; we assume that electrons instantanously adjust to any change of relative position of nuclei. Lefebvre-Brion and Field [43] give a detailed overview of the Born-Oppenheimer approximation in diatomic molecules and possible corrections to it. The description of diatomic collisions remains complex even after this simplification is introduced and 14 different terms can be identified in the Hamiltonian [49].

At ultracold temperatures, however, colliding atoms remain in the ground state and many of these terms are very small and can be neglected. In ultracold collisions it is easy to distinguish between the short-range regime for small internuclear separations which is dominated by molecular electronic interaction potentials, and the long-range regime where the internuclear separation is large. At short range, total electronic spin is well defined, locked in the singlet or triplet configuration, and precessing around the total angular momentum $\vec{F}$. At large internuclear separation, hyperfine interactions become dominant and at ultracold temperatures they are often larger than the collision energy. In this regime electronic spins are mostly coupled to the corresponding nuclear spins and precess around the total atomic angular momentum of individual atoms. Consequently, spin-exchange collisions are possible between two hyperfine states, implying that it is possible that atoms enter the collision in one hyperfine state and exit in another. External electric and magnetic fields introduce additional couplings between the fields and electronic and nuclear spins. The Zeeman and Stark interactions are at long range commonly of the same order as hyperfine couplings and have to be considered simultaneously, leading to interesting collisional physics specific to ultracold temperatures.

2.4.1 Born-Oppenheimer potentials in $T \to 0$ limit

As mentioned above, the Born-Oppenheimer Hamiltonian contains separated nuclear and electronic terms, $H_{BO} = H_N + H_e$. Since all couplings between the nuclear and electronic motion are neglected, Born-Oppenheimer molecular potentials can be constructed by evaluating electronic eigenenergies of H_e for a set of frozen internuclear separations. The resulting curves are called molecular potentials or molecular potential energy curves and are commonly used to describe atom-atom interactions. The same approximation can be extended to atom-molecule or molecule-molecule collisions, where the electronic eigenstates depend on more than one coordinate and the resulting potentials are multidimensional surfaces. Fig. (2.1) shows the two energetically lowest molecular potentials for the LiNa molecule.

Obtaining accurate Born-Oppenheimer potentials usable in the ultracold regime is a joint effort between theory and experiment. From the theoretical side *ab-initio* methods, which consider all possible electronic interactions in many-electron atoms as well as their excitations, can be used to calculate the short-range part of the potentials, typically up to 20-30 Bohr. Such calculations are rather sophisticated and involve a number of methods mostly based on either the Hartree-Fock approach or configuration interaction [50]. For larger internuclear separations the overlap of the atoms' electronic clouds decreases exponentially, which can be described well by the exchange energy term [51]

$$V_{\text{exch}} = \pm A R^{\alpha} e^{-\beta R}, \tag{2.4.1}$$

where the positive solution is used for the triplet spin state and negative for the singlet. The coefficients α and β are given in terms of binding energy for the valence electron for "one-electron" alkali metal atoms.

The van der Waals or dispersion interaction consist of attraction or repulsion of induced electric dipoles and higher-order multipoles. The fluctuation of charge density surrounding the atom A due to the electron motion temporarily induces an electric dipole moment in the charge distribution of the atom B, which then interacts with the first atom. The same holds true for higher order moments. The dispersion interaction can be accurately described by a perturbative series expansion in $1/R$, with dispersion coefficients C_n, where the positive integer n corresponds to the power of $1/R$. For two alkali ground-state atoms, the van der Waals interaction is given by

$$V_{\text{vdW}} = -\frac{C_6}{R^6} - \frac{C_8}{R^8} - \frac{C_{10}}{R^{10}}. \tag{2.4.2}$$

The relative importance of different terms in the long-range expansion is shown in Fig. (2.1) (inset). For diatomic collisions of alkali atoms it is usually sufficient to consider the total long-range interaction to be a sum of the exchange energy term and the van der Waals potential, $V_{lr} = V_{exch} + V_{vdW}$. Different functional

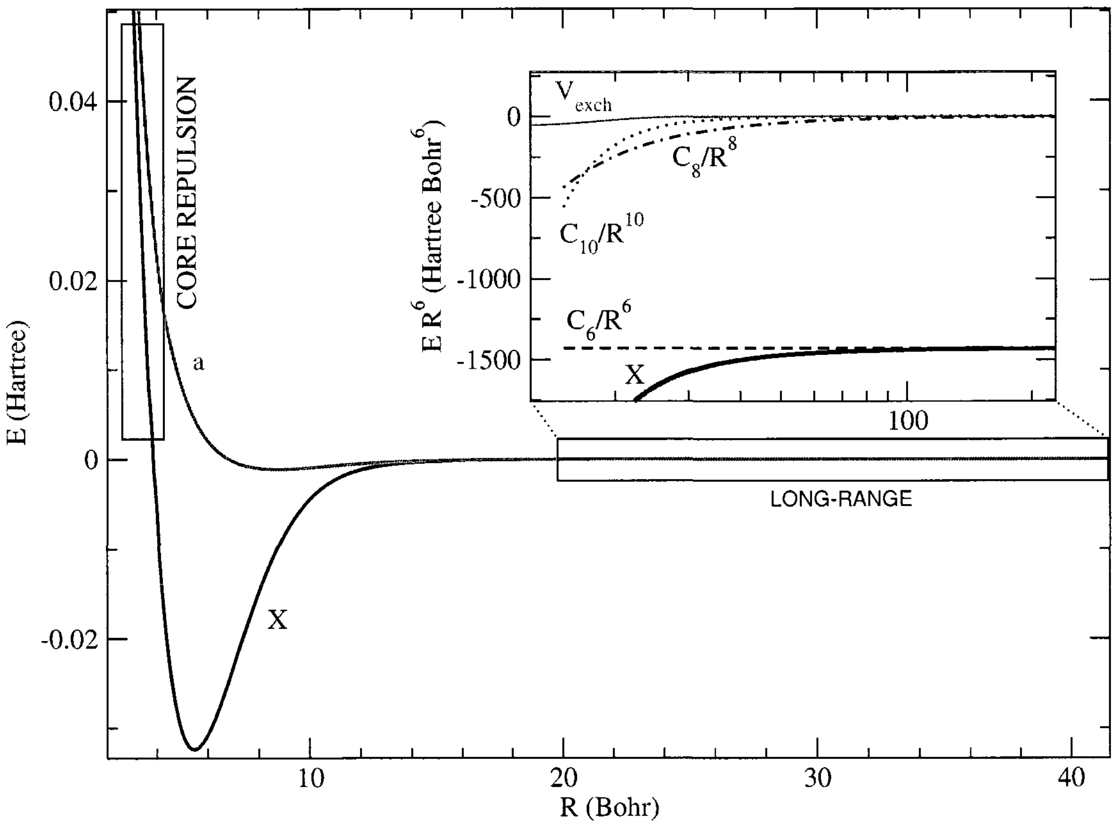

Fig. 2.1: $X^1\Sigma^+$ and $a^3\Sigma^+$ molecular potentials for the LiNa molecule.

Inset: The long-range part of the singlet potential is compared to the dispersion terms. The dominant contribution comes from the C_6/R^6 (dashed line), while the other terms can affect the bound levels close to the dissociation limit.

forms of exchange energy that offer a smoother continuation of both the short-range and the dispersion potential have been studied by different authors [52]. In addition, for very large internuclear separations of the order of thousands of Bohr radii, it is necessary to include retardation effects, relativistic corrections that account for the time required for interactions to propagate. The retardation effects will, for example, change the nature of the factor C_6/R^6 into that of C_7/R^7 for very long range interactions. More detail about the retardation effects can be found in Ref. [53]. Since the retardation effects become important only for truly spatially extended molecules, and even then are very difficult to distinguish from uncertainties associated with other terms, we will restrict ourselves to the form given in Eqs. (2.4.1) and (2.4.2) when describing long-range interactions in cold scattering calculations.

2.4.2 Hyperfine interaction

The hyperfine structure of atomic energy levels is a result of the interaction of the electron spin with the nuclear spin. Hyperfine energy level splitting is typically 2-3 orders of magnitude smaller than the fine structure, which is caused by the interaction of the electron spin and orbital angular momentum, and has to be considered separately for every fine structure level. In the ultracold regime the hyperfine interaction becomes comparable to the long-range molecular potentials and has to be considered in collisions.

A complete description of the hyperfine interaction is complicated for nuclei with spin $i > 1/2$ due to the existence of the higher order multipole terms [54]. To first order, however, higher order terms average to zero and contribute only as second-order effects to the hyperfine interaction. They can be safely neglected for spherically symmetric alkali atoms. The hyperfine interaction can therefore be modeled by the “Fermi contact term“ [55,54]

$$H_{\mathrm{hf}} = -\frac{8\pi}{3}|\Psi_e(0)|^2\langle\vec{\mu}_e\vec{\mu}_n\rangle, \tag{2.4.3}$$

where $\vec{\mu}_e$ and $\vec{\mu}_n$ are the electronic and nuclear magnetic moments, respectively. The evaluation of Ψ_e can be avoided and replaced with measured splittings of hyperfine energy levels [54]. The new form is

$$H_{\mathrm{hf}} = \alpha_{\mathrm{hf}}(f^2 - s^2 - i^2), \tag{2.4.4}$$

where $\vec{f} = \vec{s} + \vec{i}$ for an atom and α_{hf} is the hyperfine constant which can be expressed in terms of hyperfine level splittings Δ as

$$\alpha_{\mathrm{hf}} = \pm\frac{\Delta}{2i+1}. \tag{2.4.5}$$

The sign of α_{hf} is positive for “normal” energy level ordering of hyperfine states, $E(f = i + s) > E(f = i - s)$ and negative for “inverted” ordering, $E(f = i + s) < E(f = i - s)$. The total hyperfine Hamiltonian for two colliding atoms is a sum of hyperfine terms for both atoms:

$$H_{\mathrm{hf}} = \alpha_{\mathrm{hf}}^{(a)}(\vec{f_a}^{\,2} - \vec{s_a}^{\,2} - \vec{i_a}^{\,2}) + \alpha_{\mathrm{hf}}^{(b)}(\vec{f_b}^{\,2} - \vec{s_b}^{\,2} - \vec{i_b}^{\,2}). \tag{2.4.6}$$

Good examples of normal and inverted hyperfine structure are given in Refs. [56,57].

2.4.3 The spin-spin interaction

The interaction of magnetic dipoles associated with the spins of two different electrons is called the spin-spin interaction or magnetic dipole-dipole interaction. In general, the expression for the interaction term is rather complicated [43]. For two alkali metal atoms, only the spin of the valence electron of each atom can be considered to form a magnetic dipole which interacts with the dipolar field created by the second atom. This is a very good description in alkali atoms. The resulting interaction in a vector form is [58]

$$H_{ss} = -\frac{3(\hat{R}\cdot\hat{\mu}_a)(\hat{R}\cdot\hat{\mu}_b) - \hat{\mu}_a\cdot\hat{\mu}_b}{R^3}, \tag{2.4.7}$$

where μ_a and μ_b are the dipole moments of atom a and b, respectively, R is the internuclear separation and $\hat{R}$ is the unit vector with origin in atom a and aligned with the internuclear axis (all in the molecular coordinate system). The magnetic dipole-dipole interaction is anisotropic and long-range, decreasing slower with internuclear separation than the leading term of the van der Waals interaction. For small internuclear separations, $R \to 0$, the vibrational wavefunction exponentially goes to zero as the molecular potential becomes repulsive (electrons repel each other), preventing a possible divergence of the dipole-dipole term.

The magnetic dipole-dipole interaction can be rewritten in terms of second-order tensor operators [46,56]

$$H_{ss} = -\frac{\sqrt{6}\alpha^2}{R^3} \sum_q (-1)^q C_q{}^{(2)} (s_a{}^{(1)} \otimes s_b{}^{(1)})^2_{-q}, \tag{2.4.8}$$

where $C_q{}^{(2)} = \sqrt{\frac{4\pi}{5}} Y_{2q}(\theta, \phi)$ is a reduced second-order spherical harmonic that acts on the angular part of the wavefunction, $(s_a{}^{(1)} \otimes s_b{}^{(1)})^2_{-q}$ is a rank 2 tensor formed by contracting two electron spin vectors, and α is the fine structure constant. The H_{ss} operator is a scalar which, in the absence of external fields, commutes with the square of the total angular momentum f^2, with $\vec{f} = \vec{f_a} + \vec{f_b}$. The $C_q{}^{(2)}$ operator connects orbital angular quantum numbers with $\Delta\ell = 2$, of which the coupling of s and d partial waves is the most important for ultracold collisions and is sometimes included in the total Hamiltonian.

The spin-spin Hamiltonian is diagonal and easily evaluated in the $|S\Sigma\rangle$ basis, where $\Sigma = \Sigma_a + \Sigma_b$ is the projection of the total electronic spin onto the internuclear axis in the molecular coordinates [43]. The expression becomes much more complicated in the commonly used hyperfine coupled molecular basis $|Fm_F\rangle$.

The resulting matrix element is [59]:

$$\begin{aligned}\langle \alpha_a f_a m_{f_a} \ell m_\ell | H_{ss} | \alpha'_a f'_a m'_{f_a} \ell' m'_\ell \rangle &= (-1)^{-m_\ell + m'_\ell + 1} \left(\frac{\mu^2 \sqrt{6}}{R^3} \right) \\ &\times \langle l m_\ell | C^{(2)}_{m_\ell - m'_\ell} | l' m'_\ell \rangle \langle \alpha_a f_a m_{f_a} | D^{(1)\star}_{\Delta_a 0} | \alpha'_a f'_a m_{f'_a} \rangle \\ &\times \langle \alpha_b f_b m_{f_b} | D^{(1)\star}_{\Delta_b 0} | \alpha'_b f'_b m_{f'_b} \rangle \begin{pmatrix} 1 & 1 & 2 \\ \Delta_a & \Delta_b & m_\ell - m'_\ell \end{pmatrix}, \end{aligned} \tag{2.4.9}$$

where

$$\begin{aligned}\langle \ell m_\ell | C^{(2)}_{m_\ell - m'_\ell} | \ell' m'_\ell \rangle &= (-1)^{m_\ell} \sqrt{(2\ell+1)(2\ell'+1)} \\ &\times \begin{pmatrix} \ell & 2 & \ell' \\ 0 & 0 & 0 \end{pmatrix} \begin{pmatrix} \ell & 2 & \ell' \\ -m_\ell & m_\ell - m'_\ell & m'_\ell \end{pmatrix}, \end{aligned} \tag{2.4.10}$$

and

$$\begin{aligned}\langle \alpha_a f_a m_{f_a} | D^{(1)\star}_{\Delta_a 0} | \alpha'_a f'_a m_{f'_a} \rangle &= \sqrt{(2f_a+1)(2f'_a+1)} (-1)^{f'_a + m_{f_a} + 1} \\ &\times \begin{pmatrix} f'_a & 1 & f_a \\ m'_{f_a} & \Delta_a & -m_{f_a} \end{pmatrix} \langle \alpha_a f_a || D^{(1)\star}_{\Delta_a 0} || \alpha'_a f'_a \rangle. \end{aligned} \tag{2.4.11}$$

The abbreviated notation $\Delta_a = m_{f_a} - m'_{f_a}$ and $\Delta_b = m_{f_b} - m'_{f_b}$ is used in the expression above. The reduced matrix element $\langle \alpha_a f_a || D^{(1)\star}_{\Delta_a 0} || \alpha'_a f'_a \rangle$ includes all remaining relevant quantum numbers represented by α. Once the quantum numbers that define the state are known, the reduced matrix element can be calculated in a rather straightforward way by applying the Wigner-Eckart theorem [45]. For details see also Refs. [59,60].

2.5 External fields

Most atoms have a non-zero internal (nuclear and electronic) spin, which can be oriented using external electric and magnetic fields, increasing control over their interaction. The external fields break the degeneracy of atomic hyperfine structure due to the Stark and Zeeman effect, leading to a multitude of collisional channels that become accessible in experiments. In case of diatomic collisions, based on their dependence on the magnetic field, we distinguish high-field and low-field seeking states. This is important in experiments with cold gases since different designs of a magneto-optical traps are needed to trap high-field and low-field seekers [4].

Electric and magnetic fields are treated using the same formalism, with a few important distinctions. The electric field is a true vector field and it can couple states of different parity [58], unlike the magnetic field which is a pseudovector which couples states of the same parity. Both Stark and Zeeman interaction terms are given as scalar products of a dipole moment with an external field. Their effects on the system are very different as the Stark interaction term depends on the position of the charges, while the Zeeman term depends on the gradient of the field. The use of a magnetic field in ultracold experiments is more widespread since it offers a simple way to control the interaction strength between the individual atomic species via Feshbach resonances [9]. The effects of the Zeeman interaction on atoms and diatomic molecules, as well as Feshbach resonances, are discussed in the remainder of this section.

2.5.1 The Zeeman effect

The Zeeman interaction term of the diatomic Hamiltonian is given by

$$H_B = -[g\mu_B(\vec{s_a} + \vec{s_b}) + \mu_N(g_{N_a}\vec{i_a} + g_{N_b}\vec{i_b})] \cdot \vec{B}, \tag{2.5.1}$$

where g is the g-factor for the electron, μ_B is the Bohr magneton, $g_{N_{a,b}}$ are the nuclear gyromagnetic moments for atoms a and b, μ_N is the nuclear magneton, and $\vec{s}$ and $\vec{l}$ are electronic spin and orbital quantum numbers. If an electric field is not present, we can choose an arbitrary direction of the quantization axis. A typical choice is to assume the orientation of the magnetic field B along the z-axis, $\vec{B} = B\hat{z}$. The exact evaluation of the Zeeman term depends on the choice of the molecular basis. To illustrate this, we take the first term (electronic spins) and write the expression for the matrix element in the coupled molecular hyperfine basis:

$$\begin{aligned} \langle \alpha f m_f | H_B | \alpha' f' m_f' \rangle &= -\mu_B B \sqrt{2f+1} (-1)^{f'+m_f+1} \begin{pmatrix} f' & 1 & f \\ m_f' & 0 & -m_f \end{pmatrix} \\ &\times \langle \alpha f || D_0^{(1)\star} || \alpha' f' \rangle. \end{aligned} \tag{2.5.2}$$

From the symmetry argument (second row in the 3-j symbol) in Eq. (2.5.2), it follows that $m_f = m_f'$, implying that the Zeeman term preserves the projection of the spin quantum number during the collision. The reduced matrix element depends on the coupling scheme [59]. In Hund's case (a), where the electronic spin and angular momentum are coupled to the intermolecular axis, a commonplace case in diatomic alkalis, the reduced matrix element for the s-wave ($l = 0$) is

$$\begin{aligned}\langle \alpha f || D_0^{(1)\star} || \alpha' f' \rangle &= \frac{1}{2}\sqrt{(2s+1)(2s'+1)(2f'+1)}(-1)^{1+s+s'+i+f-m_s} \\ &\times \begin{Bmatrix} f & f' & 1 \\ s' & s & i \end{Bmatrix} \begin{pmatrix} s & 1 & s' \\ -m_s & 0 & m_s' \end{pmatrix}. \end{aligned} \tag{2.5.3}$$

The expression for the matrix element for the second term from the Eq. (2.5.1) has the same form, except that all electron spins are replaced with nuclear spins. An analogous expression can be derived for other coupling schemes [59]. More detail about coupling schemes and expressions for molecular collisions can be found in Refs. [45,60].

2.5.2 Magnetic Feshbach resonances

A magnetic field can be used to directly shift bound levels of a molecule and match them to the energy of the open channel, inducing a Feshbach resonance [61,62]. This property makes Feshbach resonances a tool of choice in a variety of experiments currently conducted in ultracold atomic and molecular physics. Feshbach resonances are invaluable for studying strongly interacting ultracold Bose [42,63] and Fermi gases [64], as well as systems with mixed symmetries [65]. They can also be used for efficient conversion of ultracold atoms into weakly bound molecules and back, a technique applicable to an entire ensemble [9]. Moreover, Feshbach spectroscopy can be used to set tight limits on the energy of the last bound state in molecules, leading to an accurate determination of its long-range interaction potential and scattering properties [66].

2.6 Theory of Feshbach-optimized photoassociation

In this section we briefly outline the theory behind a new optical method for efficient formation of ultracold diatomic molecules [67]. The method, which we call Feshbach-Optimized Photoassociation (FOPA), is based on photoassociation (PA) of two ultracold atoms [11,13] in a magnetic field tuned to a Feshbach resonance. The main difference between the non-perturbed PA and FOPA is the initial state: instead of an unperturbed continuum state, a nearly-resonant continuum Feshbach state is used as the starting point. Such "Feshbach wavefunction" has a significantly different nodal amplitudes than a typical continuum wavefunction. Namely, its short-range part is greatly enhanced due to the resonant coupling, resulting in a much more favorable overlap (and Franck-Condon factors) with vibrational wavefunctions in excited molecular states.

We can calculate the PA rate coefficient $K^v_{\rm PA}$ for an optical dipolar transition into the vibrational level v in an excited state according to the expression [68,69]

$$K^v_{\rm PA} = \langle v_{\rm rel}\sigma^v_{PA}\rangle, \tag{2.6.1}$$

where $v_{\rm rel}$ is the relative velocity of the colliding atomic pair, and σ^v_{PA}, is the PA cross section. The bracket stands for averaging over the distribution of $v_{\rm rel}$, where the velocity distribution is taken to be the Maxwell-Boltzmann distribution at the temperature T.

At low laser intensity I and ultracold temperatures only the s-wave contributes significantly and the maximum rate coefficient (neglecting saturation) can be expressed as [70]

$$K^{v}_{\mathrm{PA}} = \frac{8\pi^3}{h^2}\frac{I}{c}\frac{e^{-1/2}}{Q_T}|\langle\phi_{v,J=1}|D(R)|\Psi_{\epsilon,\ell=0}\rangle|^2\ , \tag{2.6.2}$$

where $Q_T = (2\pi\mu k_B T/h^2)^{3/2}$, and $D(R)$ is the appropriate dipole moment for the transition between the initial $|\Psi_{\epsilon,\ell=0}\rangle$ and final $|\phi_{v,J=1}\rangle$ states corresponding to the s-wave ($\ell = 0$) continuum wave function of the colliding pair and the populated bound level (v, $J = 1$) wave function. k_B, h, and c, are the Boltzmann and Planck constants, and the speed of light in vacuum, respectively.

We determine $|\Psi_{\epsilon,\ell=0}\rangle$ by solving the Hamiltonian for a pair of atoms in a magnetic field [9,71]:

$$H = \frac{p^2}{2\mu} + V_C + \sum_{j=1}^{2} H^{\mathrm{int}}_j\ . \tag{2.6.3}$$

Here, $V_C = V_0(R)P^0 + V_1(R)P^1$ is the Coulomb interaction, decomposed into singlet (V_0) and triplet (V_1) molecular potentials, with the associated projection operator P^0 and P^1. The internal energy of the atom j consists of the hyperfine and Zeeman contributions, respectively:

$$H^{\mathrm{int}}_j = \frac{a^{(j)}_{\mathrm{hf}}}{\hbar^2}\vec{s}_j \cdot \vec{i}_j + (\gamma_e \vec{s}_j - \gamma_n \vec{i}_j) \cdot \vec{B}, \tag{2.6.4}$$

where, for the atom j, $\vec{s}_j$ and $\vec{i}_j$ are the electronic and nuclear spin, $a^{(j)}_{\mathrm{hf}}$ is the hyperfine constant, and $\vec{B}$ is the magnetic field. The nuclear gyromagnetic factor

γ_n is the majority of alkali metal atoms about three orders of magnitude smaller than the electronic gyromagnetic factor γ_e, it can often be neglected. The Hamiltonian of a two-particle system in a magnetic field is described in detail earlier in this chapter. The coupled-channel Hamiltonian given in Eq. (2.6.3) can be diagonalized by standard numerical methods, such as, for example Johnson's log-derivative propagator for multichannel systems [72] or the mapped Fourier grid adapted for the long-range potentials [73].

The solution is projected onto the coupled molecular hyperfine basis in order to incorporate singlet and triplet molecular potentials:

$$|\Psi_{\epsilon,\ell=0}\rangle = \sum_{\alpha=1}^{N} \psi_\alpha(R)\{|f_1, m_{f_1}\rangle \otimes |f_2, m_{f_2}\rangle\}_\alpha \,, \tag{2.6.5}$$

where $\vec{f}_j = \vec{i}_j + \vec{s}_j$ is the total spin of atom j, and m_{f_j} its projection on the magnetic axis. Here, $\psi_\alpha(R)$ stands for the radial wavefunction associated with channel α labeled by the quantum numbers f_i, m_{f_i}; the Hamiltonian, given in Eq. (2.6.3), couples N channels with the total projection $m_f = m_{f_1} + m_{f_2}$.

2.6.1 Analytic expression for the photoassociation rate

It is possible to derive an analytical solution to Eq. (2.6.3), as was done for a system with two coupled channels by Pellegrini *et al.* [67]. An effective model of a two-channel system, where the continuum wavefunction ψ_1 associated with the open channel 1 (potential V_1) is coupled to the wavefunction ψ_2 associated with the closed channel 2 (V_2) (here we use the same notation as in Ref. [41]), can be represented by

$$-\frac{\hbar^2}{2\mu}\frac{d^2}{dR^2}\begin{pmatrix}\psi_1\\ \psi_2\end{pmatrix}+\begin{pmatrix}V_1 & V_{12}\\ V_{21} & V_2\end{pmatrix}\begin{pmatrix}\psi_1\\ \psi_2\end{pmatrix}=E\begin{pmatrix}\psi_1\\ \psi_2\end{pmatrix}, \tag{2.6.6}$$

where, μ is the reduced mass for the system, and, for clarity, the constants that equal to unity, such as the reduced Planck's constant $\hbar$, are included in the equations in this section. Here, we assume that both coupling terms, V_{12} and V_{21}, are real numbers, and fix the threshold energy E_1 of channel 1 at $E = 0$. If the couplings were switched off, the solution for the open channel 1 would be $\psi_1 \to \psi_{\mathrm{reg}}$ while the closed channel 2 would have a bound state $\psi_2 \to \psi_0$ with energy E_0.

A resonance occurs when E is near the energy E_0 of ψ_0. The analytical solutions for Eq. (2.6.6) are then [41]

$$\begin{aligned}\psi_1(R) &= \psi_{\mathrm{reg}}(R)+\tan\delta\ \psi_{\mathrm{irr}}(R)\ ,\\ &\overset{R\to\infty}{=} \frac{1}{\cos\delta}\sqrt{\frac{2\mu}{\pi\hbar^2 k}}\sin(kR+\delta_{\mathrm{bg}}+\delta)\ , &(2.6.7)\\ \psi_2(R) &= -\sqrt{\frac{2}{\pi\Gamma}}\sin\delta\ \psi_0(R)\ . &(2.6.8)\end{aligned}$$

Here, δ_{bg} and δ are the background and resonant phase shifts, respectively, and k is the wavenumber, $k=\sqrt{2\mu E}/\hbar$. The asymptotic regular and irregular solutions are defined as

$$\begin{aligned}\psi_{\mathrm{reg}} &= \sqrt{\frac{2\mu}{\pi\hbar^2 k}}\sin(kR+\delta_{\mathrm{bg}}),\\ \psi_{\mathrm{irr}} &= \sqrt{\frac{2\mu}{\pi\hbar^2 k}}\cos(kR+\delta_{\mathrm{bg}}). &(2.6.9)\end{aligned}$$

Finally, the width of the resonance $\Gamma = \Gamma(E)$ is allowed to vary slowly with E.

In principle, scanning the magnetic field B is equivalent to scanning the collisional energy E, since the energy E_0 of the bound state in channel 2 is shifted by the Zeeman interaction. Up to the first order in k, the s-wave phase shifts are related to the scattering length a as $\tan(\delta + \delta_{\mathrm{bg}}) = -ka$, with $\delta_{\mathrm{bg}} = -ka_{\mathrm{bg}}$, and the scattering length can be expressed as [71]

$$a = a_{\mathrm{bg}} \left(1 - \frac{\Delta}{B - B_0} \right) , \tag{2.6.10}$$

where a_{bg} is the background scattering length of the atom pair (which can slowly vary with B), B_0 is the resonant magnetic field, and Δ is the width of the resonance related to $\Gamma(E)$ [71]. Introducing the analytical solutions into Eq. (2.6.2) leads to

$$K_{\mathrm{PA}}^{v} = K_{\mathrm{off}}^{v} \left| 1 + C_1 \tan\delta + C_2 \sin\delta \right|^2 , \tag{2.6.11}$$

where

$$K_{\mathrm{off}}^{v} = \frac{8\pi^3}{h^2} \frac{I}{c} \frac{e^{-1/2}}{Q_T} |\langle \psi_v | D | \psi_{\mathrm{reg}} \rangle|^2, \tag{2.6.12}$$

is the off-resonant rate coefficient ($\delta = 0$) with ψ_v being the final (target) state. The coefficients C_1 and C_2 are defined as

$$\begin{aligned} C_1 &= \frac{\langle \psi_v | D | \psi_{\mathrm{irr}} \rangle}{\langle \psi_v | D | \psi_{\mathrm{reg}} \rangle}, \\ C_2 &= -\sqrt{\frac{2}{\pi\Gamma}} \frac{\langle \psi_v | D | \psi_0 \rangle}{\langle \psi_v | D | \psi_{\mathrm{reg}} \rangle} \end{aligned} \tag{2.6.13}$$

The coefficient C_1 relates to the open channel 1, while the coupling to the bound state ψ_0 in the closed channel 2 is given by C_2. We note that the main contribution to K_{PA}^{v} near B_0 comes from C_1, due to the fact that $\tan\delta$ diverges at the resonance while $\sin\delta$ remains finite.

The relative importance of the coefficients depends on the nodal structure of ψ_v, ψ_{reg}, ψ_{irr}, and ψ_0. Unless R_{out} of ψ_v accidentally coincides with a node in ψ_{reg} or ψ_{irr}, the overlap integrals of ψ_v with both ψ_{reg} and ψ_{irr} are of the same order, leading to $|C_1| \sim 1$. The relative size of C_2 can be controlled by the target level v. For a deeply bound level, R_{out} is at short separation where the overlap with ψ_{reg} is small while the overlap with ψ_0 can be substantial leading to $|C_2| \gg |C_1|$. For very extended levels v, R_{out} of ψ_v is at large separation and the overlap with ψ_0 less important, leading to $|C_2| \ll |C_1|$.

Chapter 3

Scattering properties and Feshbach resonances in ultracold heteronuclear alkali metal dimers

This chapter describes the calculations of Feshbach resonances and scattering properties of diatomic alkalis. We performed full quantum coupled-channel scattering calculations for Li+Na and Li+Rb mixtures, using the model and numerical techniques outlined in the previous chapter. These particular mixtures were selected for their richness and experimental availability, not necessarily in this order. For lithium, isotopes of different symmetry (*i.e.*, ^{6}Li is a composite fermion and ^{7}Li a composite boson) exist. When lithium is paired with another alkali, a bosonic, fermionic or bose-fermi ultracold mixture is formed, which makes it possible to design experiments to study either a molecular BEC or a two-component bose-fermi mixture.

Since scattering properties in the ultracold regime are strongly dependent on molecular potentials, our calculation had to be performed for the best available sets of potential surfaces. We used experimental trap-loss measurements for

^{6}Li+^{23}Na [65] and ^{6,7}Li+Rb [74,75] to modify the existing molecular potentials and to correctly reproduce the structure of observed Feshbach resonances. In addition, for Li+Rb mixtures, theoretical calculations are available for selected channels and isotopes [75,76]. Using these results, we calculated the positions and widths Feshbach resonances in all collisional channels, as well as other scattering properties of these systems.

We have published calculated positions of Feshbach resonances and scattering lengths for ^{6}Li+^{23}Na and ^{7}Li+^{23}Na mixtures presented in this section [77].

3.1 Coupled-channel calculation of scattering properties

In this section we construct a system of coupled-channel equations and solve it for ultracold collision of two alkali atoms in an external magnetic field. A detailed explanation of the individual interaction terms and the physics involved can be found in chapter 2. To better illustrate some aspects of the problem, we use real physical parameters corresponding to the Li+Na mixture. The outlined procedure is easily applicable to other heteronuclear diatomic alkali metals, although the final size of the system of equations depends on the nuclear spin of the atoms and may vary. For all alkali metal atoms the electronic spin $s_j = 1/2$, leading to the molecular electronic spin $s = 0$ (singlet) or $s = 1$ (triplet). If the wavefunction is properly symmetrized with respect to the exchange of nuclei, the same procedure can be used for collisions of homonuclear atoms.

For two alkali atoms of relative momentum $\vec{p}$ and reduced mass μ colliding in a magnetic field, the effective two-body Hamiltonian can be written as [71,78,79]

$$H = \frac{p^2}{2\mu} + \sum_{j=1}^{2} H_j^{\text{int}} + V^c + V^d, \tag{3.1.1}$$

where V^c is the Coulomb interaction, V^d the magnetic dipole-dipole interaction, and H_j^{int} the internal energy of atom j ($j = 1, 2$), consisting of the hyperfine and Zeeman contributions, respectively (see chapter 2).

The internal atomic Hamiltonian is

$$H_j^{\text{int}} = \frac{a_{\text{hf}}^{(j)}}{\hbar^2} \vec{s}_j adot \vec{i}_j + (g_e \beta s_z^{(j)} - g_N \beta_N i_z^{(j)}) B, \tag{3.1.2}$$

where $\vec{s}_j$ and $\vec{i}_j$ are the electronic and nuclear spin for the atom j, $\vec{B} = B\hat{z}$ is the external magnetic field, which we choose to point in the $\hat{z}$-direction, $a_{\text{hf}}^{(j)}$ is the hyperfine constant for the atom j, $\beta = e\hbar/2m_e$ and $\beta_N = e\hbar/2M$ are Bohr and nuclear magnetons defined for electronic and nuclear mass, m_e and M. $g_e = 2.002319$ is the electron spin g-factor [80], and g_N is the nuclear spin g-factor for a particular nucleus. Hyperfine constants for the considered diatomic mixtures are listed in Table 3.1. While higher-order interaction terms exist in a complete description of a diatomic system, it has been shown that this form of effective Hamiltonian can reproduce observable physical quantities to the promille level [81].

At ultracold temperatures, collisional physics is dominated by the s-wave ($l = 0$ partial wave) collisions. However, for some alkali dimers, Feshbach resonances

	a_{hf} (MHz)	nucl. spin i
^{6}Li	152.173	1
^{7}Li	401.752	3/2
^{23}Na	885.813	3/2
^{39}K	230.860	3/2
^{40}K	-285.7308	4
^{41}K	127.007	3/2
^{85}Rb	1011.910	3/2
^{87}Rb	3417.341	5/2

Table 3.1: Hyperfine constants and nuclear spin of alkali metal atoms considered in collisions.

induced by higher partial waves were observed in experiments [9]. We consider both s- and p-wave collisions in our analysis.

The collision entrance channel is determined by the atoms' initial Zeeman states. To evaluate the hyperfine terms we choose the uncoupled hyperfine basis defined as

$$|f_1, m_{f_1}; f_2, m_{f_2}\rangle \equiv |f_1, m_{f_1}\rangle \otimes |f_2, m_{f_2}\rangle, \tag{3.1.3}$$

where $\vec{f_j} = \vec{s_j} + \vec{i_j}$ is the total spin of the atom j, m_j is its projection onto the molecular axis, and atoms are indicated by a and b. This basis set is suitable for modeling the problem at large distances in the limit of two separated atoms. At smaller separations a coupled molecular basis $|(si)fm_f\rangle$ becomes more appropriate. Here, $\vec{s} = \vec{s}_1 + \vec{s}_2$, $\vec{i} = \vec{i}_1 + \vec{i}_2$, $\vec{f} = \vec{f}_1 + \vec{f}_2$, and m_f is the projection of the total angular momentum f.

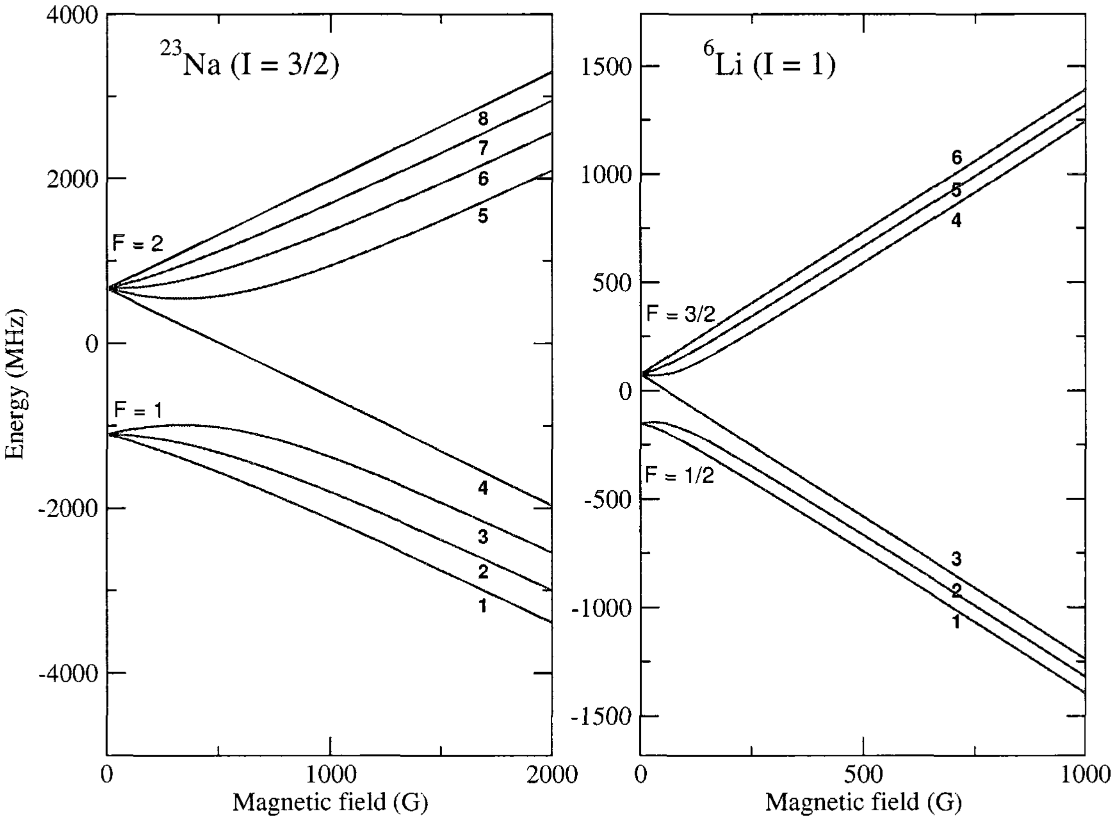

Fig. 3.1: Atomic hyperfine structure of ^{6}Li and ^{23}Na. Channels $|\alpha\rangle$ and $|\beta\rangle$ are indicated on the curves.

Once the bases are defined, one can express Eq. (3.1.1) in a matrix form, leading to the following matrix equation for the system

$$\frac{d^2}{dR^2}\mathbf{F}(R) = \frac{2\mu}{\hbar^2}\mathbf{C}(R)\mathbf{F}(R), \tag{3.1.4}$$

where the coupling coefficient matrix $\mathbf{C}(R)$ is defined as

$$\mathbf{C}^{(\alpha',\beta')}_{(\alpha,\beta)}(R)\frac{\delta(R-R')}{RR'} = \langle R(\alpha,\beta)|V^c|R'(\alpha',\beta')\rangle, \tag{3.1.5}$$

and $\mathbf{F}(R)$ is the matrix in which columns correspond to a complete set of linearly independent solutions. We follow the standard labeling of channels used in the literature related to interactions involving hyperfine structure in a magnetic field, such as in Ref. [82]. The idea is to label molecular hyperfine states as a combination of atomic hyperfine states, starting from the energeticaly lowest state. For example, for Li+Na mixture, we have: $|\alpha\beta\rangle$, with $\alpha = 1, \ldots, 6$ for ^{6}Li, $\alpha = 1, \ldots, 8$ for ^{7}Li, and $\beta = 1, \ldots, 8$ for ^{23}Na, all in the increasing order of energy. In such "channel index" notation the lowest energy channel is $|11\rangle$. We illustrate this in Figure 3.1 for hyperfine states of ^{6}Li and ^{23}Na in a magnetic field.

The interaction potential due to the Coulombic interactions of the component particles, which depends only on the magnitude of the internuclear separation R, can be decomposed into singlet and triplet contributions:

$$V^c(R) = V_s(R)P_s + V_t(R)P_t, \tag{3.1.6}$$

where V_s (V_t) stands for the singlet (triplet) molecular potential and P_s (P_t) is the associated projection operator [41,83]. It is important to emphasize how these operators connect electronic states so we next analyze them in more detail and discuss some of their properties.

The singlet and triplet projection operators can be written as

$$\begin{aligned} P_s &= |s = 0 \; m_s = 0\rangle\langle s = 0 \; m_s = 0|, && (3.1.7) \\ P_t &= |1 \; {-1}\rangle\langle 1 \; {-1}| + |10\rangle\langle 10| + |11\rangle\langle 11|, && (3.1.8) \end{aligned}$$

where quantum numbers for P_t are also s and m_s, as for P_s.

Projection operators commute with total electron spin $s = s_1 + s_2$, but not with the electron spin of a single atom. In addition, they trivially commute with the nuclear spin i (they do not act on it; spin and nuclear quantum numbers are defined in mutually orthogonal subspaces of the Hilbert space for the problem). It follows that the projection operators commute with the hyperfine quantum number $f = f_1 + f_2$, but not with f_1 or f_2. From these arguments it follows that the exchange transition can occur only between the states for which m_f, the projection of the total angular momentum f, is conserved. Physically, the system remains invariant under rotations with respect to the axis of the magnetic field in the collisions.

Therefore, the projection m_f determines the channels which can couple to satisfy the symmetry requirement $m_f = m_{f_1} + m_{f_2}$. In the matrix notation used above, providing the coupled molecular hyperfine basis is used, the channels will be grouped in diagonal block matrices according to their m_f symmetry, without off-diagonal elements that would connect different blocks. Each m_f block of the Hamiltonian can be diagonalized separately, which simplifies numerical evaluation. Clearly, m_f symmetry of the entrance channel determines a subset of channels with the same m_f that need to be included in the calculation. For example, in case of ^{6}Li+^{23}Na there is a total of 6×8 channels. This reduces to an 8-channel problem for the entrance channel $|11\rangle$, as only the channels with $m_f = 3/2$ remain coupled.

Only singlet and triplet electronic potentials are relevant for the calculation of Feshbach resonances and other collisional properties at ultracold temperatures. For all mixtures considered here, molecular potentials were constructed by smoothly connecting their inner part to the long-range expansion

$$V_{\mathrm{LR}} = -\frac{C_6}{R^6} - \frac{C_8}{R^8} - \frac{C_{10}}{R^{10}} \pm V_{\mathrm{exch}} \tag{3.1.9}$$

where ± stands for the triplet and singlet potential, respectively. The exchange energy V_{exch} is described using either the simple form

$$V_{\mathrm{exch}} = C_{\mathrm{ex}} e^{-bR}, \tag{3.1.10}$$

or the Smirnov-Chibisov expression [51]

$$V_{\mathrm{exch}} = A_{\mathrm{ex}} R^{\alpha} e^{-\beta R}. \tag{3.1.11}$$

Here, C_{ex}, b, A_{ex}, α and β are real constants.

The details of the molecular potential construction will be discussed in detail for individual systems in subsequent sections.

3.1.1 Solving the coupled-channel system

We solved Eq. (3.1.4) numerically for different values of magnetic field using log-derivative propagator [84] to obtain the **S**-matrix, from which we extract the phase shift $\eta(k)$ of the initial entrance channel for the radial wavefunction. The scattering length a is calculated using [38]

$$k \cot \eta(k) = -\frac{1}{a}, \tag{3.1.12}$$

where, $k = \sqrt{2\mu E}/\hbar$ is the wavenumber associated with the pair of colliding atoms of relative energy E.

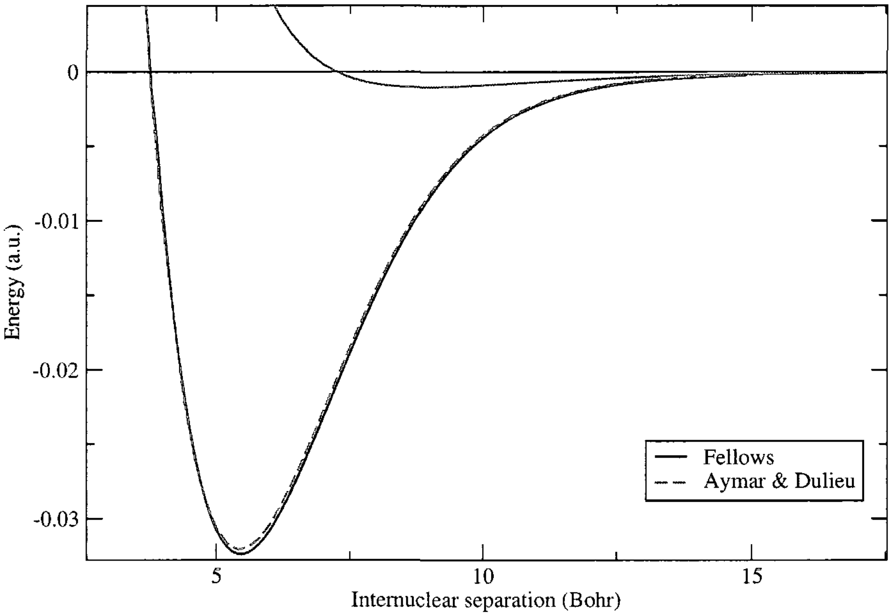

Fig. 3.2: LiNa molecular potentials used in the calculation (thick lines). Dashed red line is Aymar & Dulieu singlet potential curve.

3.2 ^{6}Li+^{23}Na and ^{7}Li+^{23}Na mixtures

3.2.1 Molecular potentials

We used the singlet potential by Fellows [85], constructed from accurate spectroscopic data via the inverse perturbation approach (IPA). Spectroscopic measurements were not carried out for the triplet potential; we instead used the *ab initio* potential computed using the *CIPSI* package [86], which was adjusted to match the atomic dissociation energy of Li(2s) + Na(3s) at infinity. For the long range form of both potentials, we adopted the dispersion coefficients (C_n) and exchange energy (C_ex and b) of Fellows [85] (case a).

Next, we repeated the scattering calculation using singlet and triplet *ab-initio* potentials [86] with the long-range part constructed using dispersion coefficients C_6, C_8 and C_{10} calculated by Derevianko and colleagues [87,88]. Both sets of molecular potentials are illustrated in Figure 3.2. We choose the first set of molecular potentials, the singlet by Fellows [86] and the triplet by Aymar & Dulieu [85], since they more accurately reproduced known scattering properties of the Li+Na mixture.

3.2.2 *s*-wave Feshbach resonances

We first calculated the positions of Feshbach resonances for the least energetic hyperfine state $|\alpha\beta\rangle = |11\rangle$ of ^{6}Li+^{23}Na. Since there is no inelastic spin relaxation for this channel (it is the lowest energy channel already) and the only possible decay is via 3-body interactions, it is especially attractive for trapping experiments. Stan *et al.* [65] have measured the positions of three Feshbach resonances for this state and we used their results to calibrate the singlet and triplet potentials. This was a necessary step since, as expected, we were not able to reproduce correct scattering lengths nor the resonances by using the published potentials.

For each molecular potential we varied the inner wall by shifting data points for separations less than the equilibrium separation R_e according to

$$R_{\text{shifted}} = R + s\frac{R - R_e}{R_c - R_e}, \qquad (3.2.1)$$

where s corresponds to the shift of the zero-energy classical turning point R_c.

The slope of the repulsive inner wall changes as s changes, which affects the phase shift of the scattered wavefunction. We scanned the shifts for the singlet and triplet, s_s and s_t, until the best agreement with the measured resonances [65] was achieved for the smallest shifts. Positions and widths of Feshbach resonances are very sensitive to molecular potentials, requiring high resolution in s, up to 1 part in 10^{-4}, in order to reach good agreement with measurements. Such a task, while numerically intensive, illustrates the precision of Feshbach spectroscopy, which can be used to significantly improve existing molecular potentials. The best agreement with measured Feshbach resonances [65] was achieved for $s_s = 0.06170$ a.u. (singlet) and $s_t = -0.32878$ a.u. (triplet).

It may also be worth noting that we obtained a very good agreement with the experimental results only after we included the coupling with nuclear spin and the magnetic dipole-dipole interaction. Neglecting second-order terms results in agreement within ± 5 Gauss for the measured resonances, as opposed to $\sim \pm 0.1$ Gauss when the second order effects are accounted for. Results with and without second-order effects are illustrated and compared in Figure 3.4.

Our results, for the entrance channel $|11\rangle$ and magnetic field up to 2000 Gauss, are illustrated in Figure 3.6 and summarized in Table 3.2. Note that we predict four additional Feshbach resonances at higher values of magnetic field, at 1097, 1186, 1766 and 1850 Gauss.

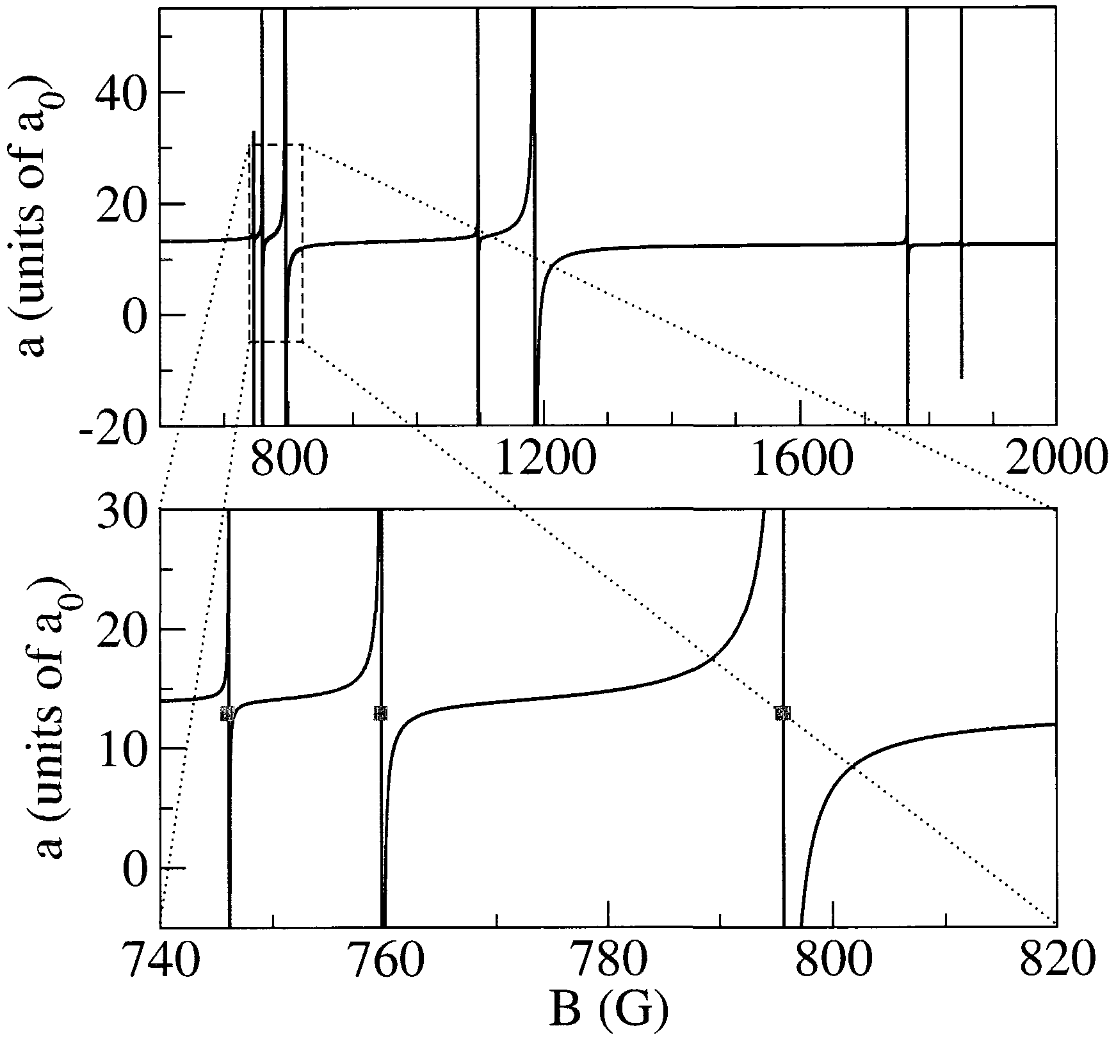

Fig. 3.3: *Top:* Scattering length for ^{6}Li+^{23}Na in the entrance channel $|11\rangle$. Positions and widths of the resonances are given in Table 3.2. *Bottom:* Zoom on the first three resonances. Squares indicate measured resonances.

B_0^{th} (G)	B_0^{exp} (G)	Δ (G)	a_{bg} (a_0)
746.13	746.0 ± 0.4	0.044	14.003
759.69	759.6 ± 0.2	0.310	13.864
795.61	795.6 ± 0.2	2.177	13.002
1096.68		0.153	13.902
1185.70		8.726	12.673
1766.13		0.156	12.500
1850.13		0.019	12.499

Table 3.2: Calculated s-wave Feshbach resonances for the entrance channel $|11\rangle$ and B up to 2000 Gauss in ^{6}Li+^{23}Na. The resonance width Δ and the background scattering length a_{bg} are given for the resonances and experimental data is shown for reference. Parameters a_{bg} and Δ were obtained by fitting to the form $a(B) = a_{\text{bg}}\left(1 - \frac{\Delta}{B-B_0}\right)$.

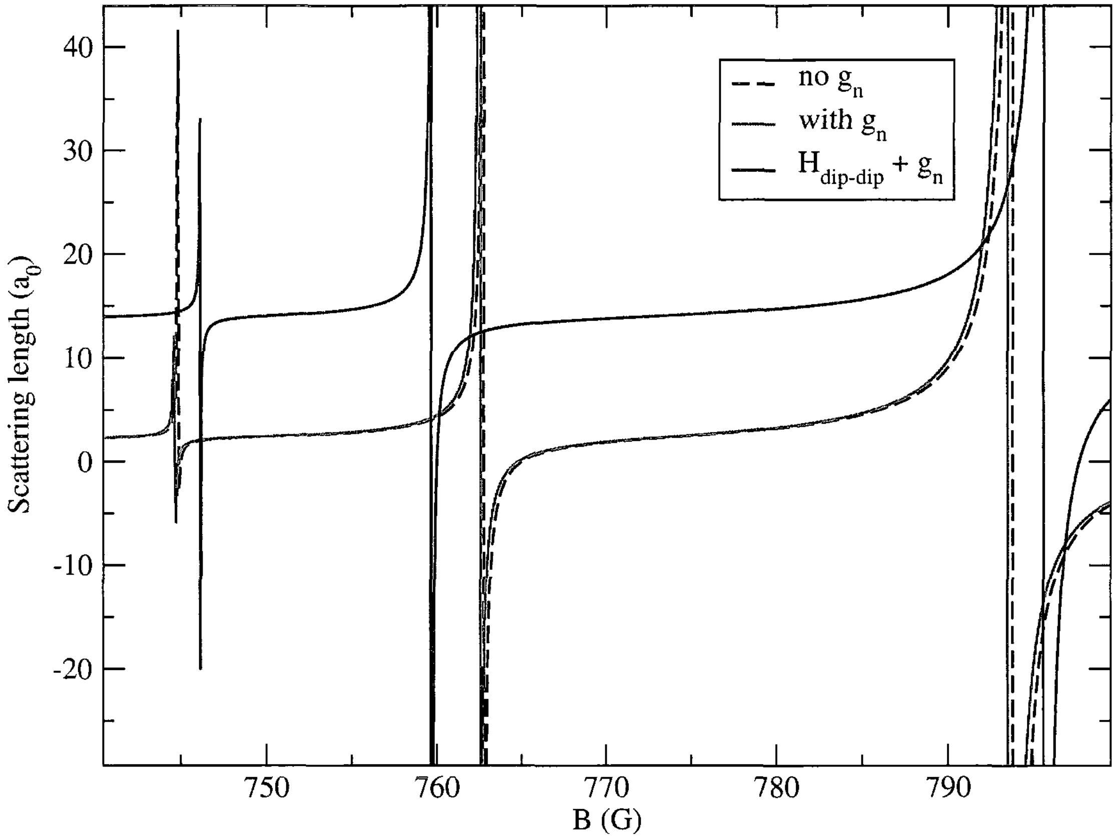

Fig. 3.4: *Top:* Calculated scattering length for ^{6}Li+^{23}Na in the entrance channel $|11\rangle$ with and without second-order effects included.

3.2.3 Singlet and triplet scattering lengths

Once the potentials were adjusted to accurately reproduce measured Feshbach resonances, we calculated the singlet (a_S) and triplet (a_T) scattering lengths, as well as the energy of the last vibrational level ($E_{\text{last}}^{S,T}$) for both ^{6}Li+^{23}Na and ^{7}Li+^{23}Na mixtures (see Table 3.3). Molecular potentials for the ^{7}Li+^{23}Na mixture were obtained by mass-scaling neglecting non-adiabatic terms caused by the isotope shifts, possibly introducing small uncertainties in the calculated positions of Feshbach resonances [55,57].

Stan *et al.* [65,89] reported favorable thermalization rates for the ^{6}Li+^{23}Na mixture and relied on efficient thermalization to sympathetically cool ^{6}Li with ^{23}Na to ultracold temperatures. Our results are in agreement with the estimate based on these rates. From their experimental thermalization rate the MIT group estimated the ratio of pure triplet elastic collision between ^{23}Na-^{23}Na (σ_{AA}) and ^{6}Li+^{23}Na (σ_{AB}) to be $\sigma_{AA}/\sigma_{AB} \sim 100$ [89,90], where $\sigma_{AA} = 8\pi a^2_{\mathrm{Na-Na}}$ and $\sigma_{AB} = 4\pi a^2_{\mathrm{Li+Na}}$, with $a_{\mathrm{Na-Na}} = 85\ a_0$ for the triplet scattering length of Na. One then estimates $|a_{\mathrm{Li+Na}}| = 12\ a_0$ for the pure triplet case. This estimate is also in agreement with the value of $|a_T| \approx 15\ a_0$, obtained assuming a thermalization time of $\tau_{\mathrm{tot}} \sim 4\tau \sim 15$ seconds, where the relationship between τ and a is given in [91]. The uncertainty in the scattering length was determined by adjusting the inner wall of the potentials to match the uncertainty of the resonances (Table 3.2). Alternatively, we shifted the triplet potential below the last bound state by ±140 MHz [65], and then adjusted the inner wall of both the singlet and triplet curves to match the experimental position of the resonances. We illustrate dependence of scattering length on shifts s_s and s_t in Figure 3.5. The scattering lengths were larger without second-order effects included, which would indicate higher thermalization rates than measured. The last triplet bound level was then found to be $E^T_{\mathrm{last}} = -5720 \pm 16$ MHz, as compared to the estimated value of $E^T_{\mathrm{last}} = -5550 \pm 140$ MHz of Stan *et al.* [65].

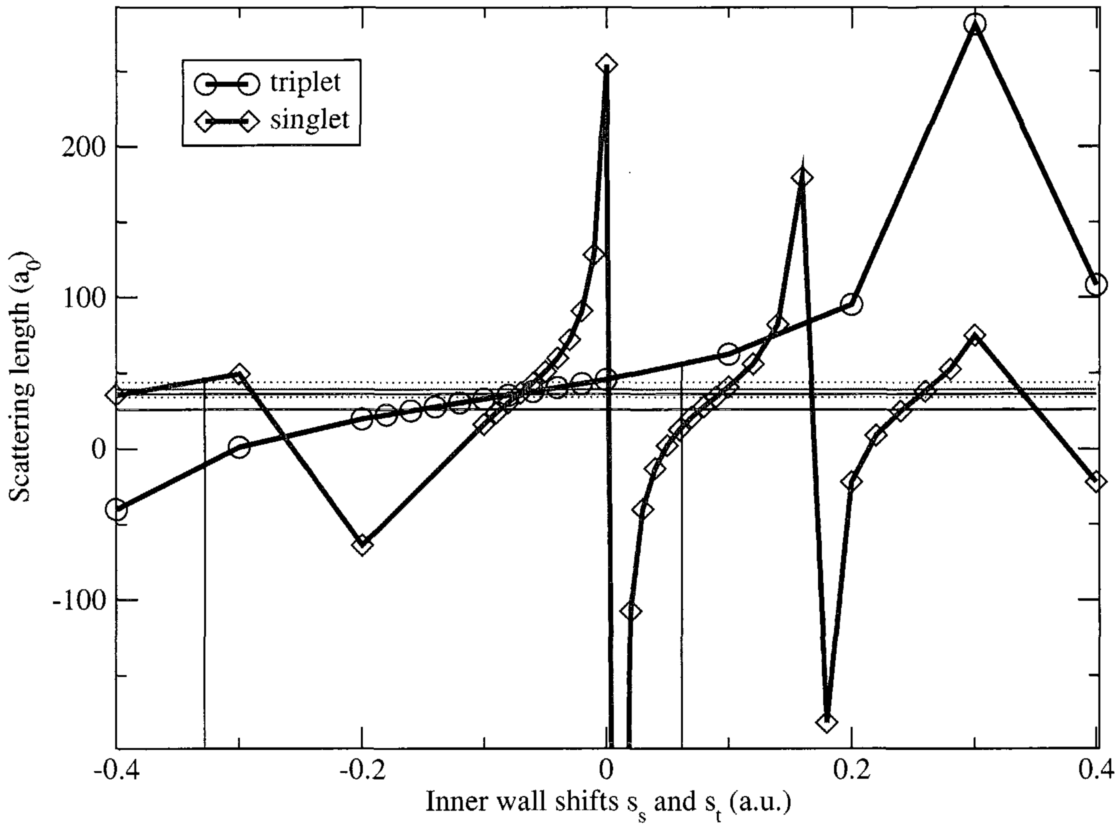

Fig. 3.5: Variation of the scattering length for the ^{6}Li+^{23}Na singlet and triplet potentials. The second-order effects are not included. Estimates of scattering lengths from thermalization times are indicated by pairs of horizontal straight and dotted lines obtained for $|a_S| = 12\ a_0$ and $|a_T| = 15\ a_0$. Two vertical lines indicate potential shifts for which the best match with measured Feshbach resonances was obtained. The periodically repeating character of the scattering length is due to the addition or disappearing of a vibrational level as the potential well changes.

	Present work		Ref. [91]
	^{7}Li+^{23}Na	^{6}Li+^{23}Na	^{6}Li+^{23}Na
a_S	39.7 ± 0.5	15.9 ± 0.3	39.2
a_T	36.1 ± 0.3	12.9 ± 0.6	31.1
v^S_{last}	47	45	
v^T_{last}	12	11	
E^S_{last} (MHz)	-1505 ± 3	-1.6 ± 0.2	
E^T_{last} (MHz)	-7112 ± 12	-5720 ± 16	

Table 3.3: ^{6,7}Li+^{23}Na singlet (S) and triplet (T) scattering lengths in units of a_0, the last vibrational level, and the corresponding binding energy. Uncertainties are explained in the text.

The same procedure was repeated after varying the C_6 coefficient by ±5%, and the results were within the uncertainties given in Table 3.3. Note that Feshbach resonances are very sensitive to the energy of the last vibrational level, which thus can be determined very precisely, while the total number of levels can only be estimated since it depends on the entire potential, which is usually not known to sufficient accuracy. For the adjusted triplet state of ^{6}Li^{23}Na, we found 11 vibrational levels (see Table 3.3).

Using our adjusted singlet and triplet potential curves, we performed a similar calculation for all entrance channels for ^{6}Li+^{23}Na and ^{7}Li+^{23}Na. Predicted

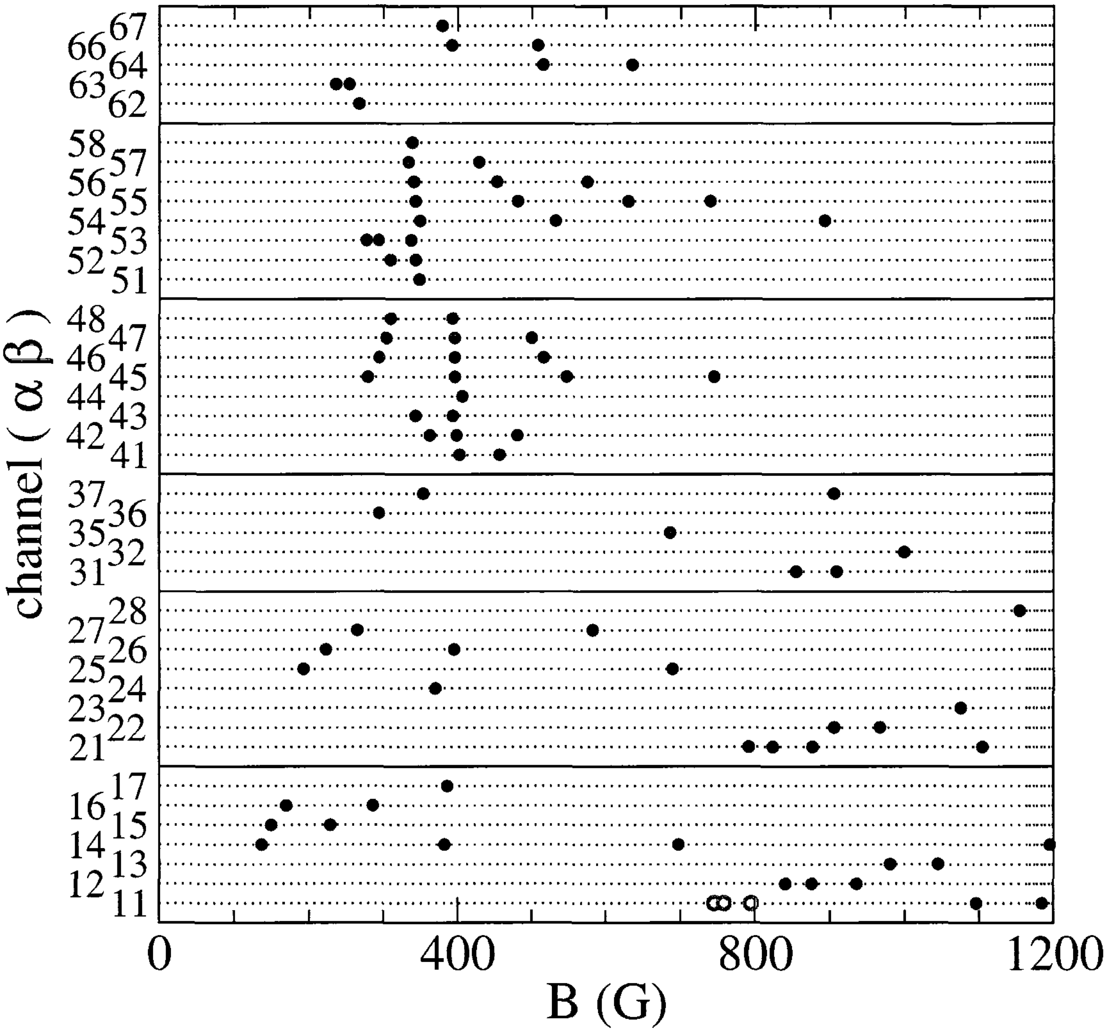

Fig. 3.6: Feshbach resonances in ^{6}Li+^{23}Na for different collisional entrance channels. The collisional entrance channels $\alpha\beta$ for which the resonances exist are shown. Open circles for channel $|11\rangle$ were observed experimentally.

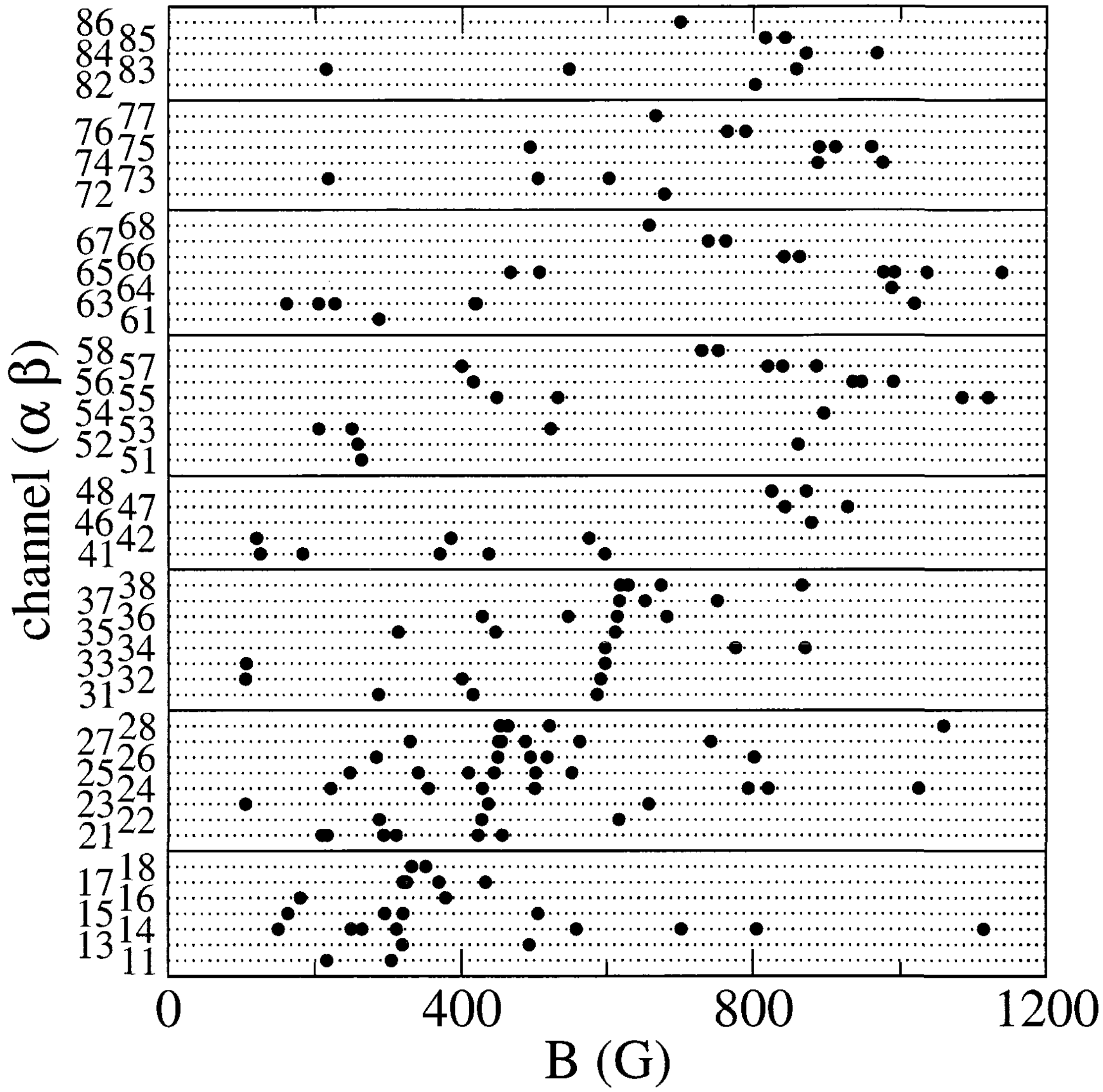

Fig. 3.7: Feshbach resonances in ^{7}Li+^{23}Na for different collisional entrance channels. The collisional entrance channels $\alpha\beta$ for which the resonances exist are shown.

positions of Feshbach resonances are shown schematically in Figures 3.6 and 3.7. It appears that the ^{7}Li+^{23}Na mixture has several experimentally attainable Feshbach resonances for the high-field seeking hyperfine states.

3.2.4 Asymptotic bound-state model

It is possible to qualitatively estimate positions of Feshbach resonances by looking at the asymptotic form of the two-particle Hamiltonian (Eq. (3.1.1)) for large internuclear separation $R \to \infty$. In this limit molecular potentials $V(R)$ vanish and we are left with the coupled-channel system for infinite R. This system is very simple to solve since it contains no dependence on R. By diagonalizing the asymptotic Hamiltonian we obtain energies that depend on the magnetic field. As for the full problem, the projection of the total magnetic quantum number m_F remains a constant of the motion throughout the collision, and determines mutually non-interacting subspaces. In the other words, the interaction between the two hyperfine states, including the incoming channel, can occur only if they have the same m_F.

In order to determine the positions of Feshbach resonances, we consider another set of identical asymptotic solutions shifted by the energy of the last bound vibrational level in both singlet and triplet potentials. The two sets depend on the magnetic field and their intersections will give the approximate positions of Feshbach resonances. We recall that a Feshbach resonance occurs when the en-

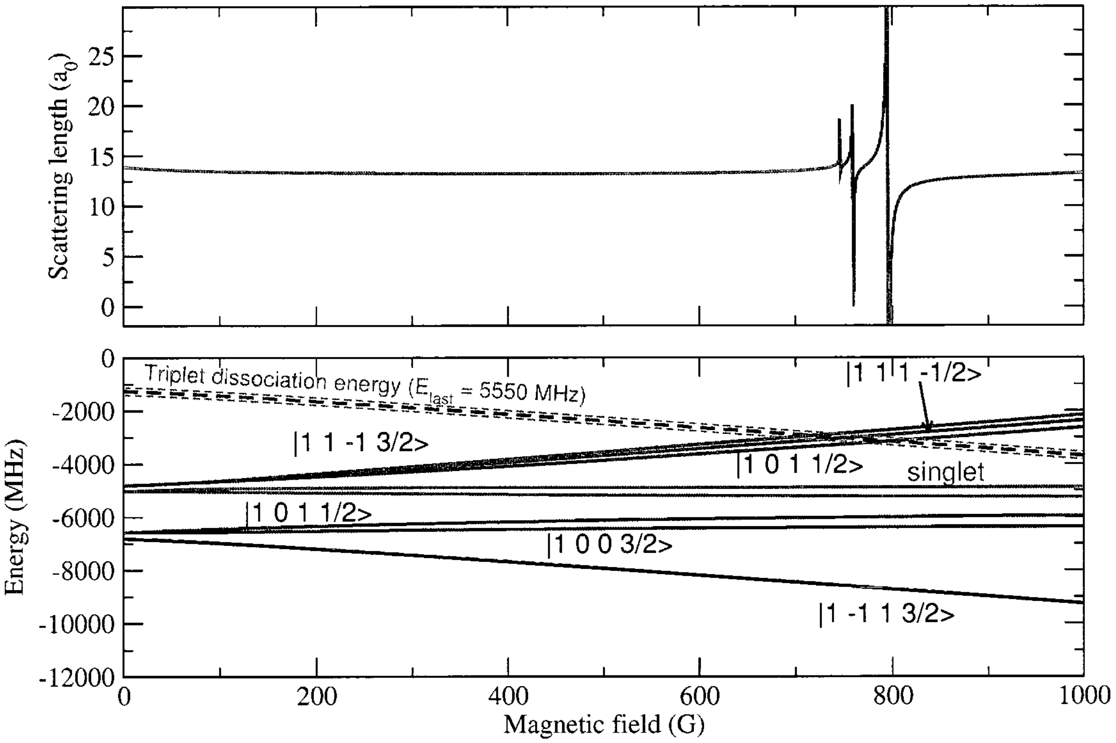

Fig. 3.8: *Top:* Feshbach resonances for the entrance channel $|11\rangle$ of ^{6}Li+^{23}Na (full calculation). *Bottom:* Asymptotic molecular hyperfine states for the same entrance channel (solid lines). Triplet states are identified in the basis $|Sm_S m_{i_{\mathrm{Li}}} m_{i_{\mathrm{Na}}}\rangle$. The lowest energy state (dashed black line) is shifted by the triplet dissociation energy of the last bound level and its uncertainties are indicated (dashed red lines).

ergy of one channel (usually the open channel) matches that of another (closed) channel. While in the complete description of the problem, the hyperfine energies will be affected by the molecular potentials, the asymptotic model can be used to determine the number of Feshbach resonances and approximate magnetic fields at which they are expected to occur. This model is sometimes called the *asymptotic bound-state model* [65,76,71].

Figure 3.8 compares the asymptotic model to the full coupled-channel calculation for channel $|11\rangle$ of ^{6}Li+^{23}Na mixture. Three intersections of the lowest hyperfine state shifted by the dissociation energy of the last bound level in the triplet potential (given in dashed line) approximately correspond to the Feshbach resonances at 745, 754.6 and 795.6 G. While the locations of the resonances are not exact, they are very useful for establishing a number of expected resonances and identifying resonant hyperfine states. When the diagram is extended to higher magnetic fields, two pairs of hyperfine states also intersect the shifted state, indicating that four more resonances are present, in agreement with the full calculation (see Table (3.2)). The asymptotic model is a very useful tool in the often complicated analysis of Feshbach resonances, as we illustrated for ^{6}Li+^{23}Na mixture.

3.2.5 p-wave Feshbach resonances

We used the molecular potentials constructed and tested in the previous section to expand our study of Li+Na mixtures to include p-wave Feshbach resonances. To do this, we included the angular momentum operator $\hat{L}^2/2\mu R^2$ in the Hamiltonian Eq. (3.1.1). If we expand the molecular basis to include quantum numbers ℓ and m_ℓ, we obtain an extra diagonal term equal to $\ell(\ell+1)/2\mu R^2$. The coupling between $\ell = 0$ and $\ell = 1$ partial waves is zero, which makes it possible to calculate scattering properties separately for s- and p-waves.

Currently, there are no published experimental data for p-wave resonances in Li+Na mixtures so it was impossible to make a direct comparison of calculated and measured resonances. However, a similar calculation for other alkali mixtures, namely Li+Rb, gave us a very accurate result that was within 1 Gauss of observed p-wave resonances (see the Section 3.3 below). Considering this very good agreement with the experimental results, and those obtained for the s-wave resonances, we expect a similar agreement for the p-wave resonances. Calculated p-wave Feshbach resonances for ^{6}Li+^{23}Na and ^{7}Li+^{23}Na are listed in Tables 3.4 and 3.5, respectively. As for the s-wave resonances, most Feshbach resonances are found in the lower hyperfine state, and there are similarities between the resonant structure. For example, three s-wave resonances found between 750 and 800 G in channel $|11\rangle$ also appear as p-wave resonances, as both are caused by the hyperfine channels $|1\ 1\ 1\ -1/2\rangle$, $|1\ 1\ -1\ 3/2\rangle$, and $|1\ 0\ 1\ 1/2\rangle$, all in $|s\ m_s\ m_{i_{Li}}\ m_{i_{Na}}\rangle$

basis, except that in the p-wave case the hyperfine energies are perturbed by a different kinetic energy term, *i.e.*, centrifugal barrier.

3.2.6 Inelastic decay rates

Decay modes of spin-polarized gases have been a subject of study even before the first successful experimental realizations of trapped gases in the milliKelvin regime. Stoof *et al.* [82] were among the first to perform a coupled-channel calculation of spin-exchange and dipole relaxation rates in hydrogen, a system that was being investigated as a candidate for cooling and forming a BEC. Examining spin-exchange relaxation between hyperfine states and relaxation rates is important for estimating the lifetime of a trapped atom or a molecule in a particular state. A majority of trap loss occurs via two-body collisions, leading to a spin-exchange in which a trapped object changes its state from one favorable for trapping to one that cannot be trapped, *i.e.*, from a high-field seeking to a low-field seeking state, and is ejected from the trap. The external magnetic field affects the hyperfine structure and relaxation rates. In several studies, as prospects of creating BECs in magneto-optical traps were investigated, decay rates in a magnetic field were calculated for different diatomic alkali mixtures. For example, inelastic relaxation in an external magnetic field was calculated for Cs_2 [61], and Li_2 systems [92] .

We calculated inelastic decay rates for ^{6,7}Li+^{23}Na mixtures in a magnetic field. The inelastic rate can be calculated from the S-matrix which was obtained

$\vert\alpha\beta\rangle$	B_0 (G)	$\vert\alpha\beta\rangle$	B_0 (G)	$\vert\alpha\beta\rangle$	B_0 (G)	$\vert\alpha\beta\rangle$	B_0 (G)
11	542	21	577	31	542	61	1165
	555		599		629		1246
	570		635		670		
	770		777		773*	62	1416
	870		884		896		
	1390		942		967		
	1480		1383*		1409*		
			1427		1468		
12	622	22	679	32	762		
	648		726		914		
	692		865		1075		
	864		986*	33	1101		
	974		1051				
	1026			41	1245		
	1494				1349*		
13	754	23	845	51	1166		
	809		1053		1245		
	1005				1351*		
14	993	24	1317	52	1417		
	1275						

Table 3.4: Calculated p-wave Feshbach resonances up to 2000 G in ^{6}Li+^{23}Na for all entrance channels. Quasiresonances are indicated by stars.

$\|\alpha\beta\rangle$	B_0 (G)	$\|\alpha\beta\rangle$	B_0 (G)
11	21	31	43*
	37		120
			319
12	25	32	118
	40		323
	117		614*
13	43	33	328
	130		420
21	25	41	266*
	39		393
	110		
22	42	42	296*
	114		393
	325		
23	118	43	248
	360		
	452	81	789

Table 3.5: Calculated p-wave Feshbach resonances up to 2000 G in ^{7}Li+^{23}Na for all entrance channels. Quasiresonances are indicated by stars.

by solving the coupled-channel system described by Eq. (3.1.4). We used the zero-temperature expression for the relaxation rate [82,92]

$$G_{\alpha\beta\to\alpha'\beta'} = \lim_{k_{\alpha\beta}\to 0} \frac{\pi\hbar}{\mu k_{\alpha\beta}} |S_{\alpha'\beta',\alpha\beta}(k_{\alpha\beta}) - \delta_{\{\alpha'\beta'\},\{\alpha\beta\}}|^2. \tag{3.2.2}$$

Here, μ is the reduced mass of the colliding atoms, $\hbar k_{\alpha\beta}$ is the relative momentum of the incoming particles in channel $|\alpha\beta\rangle$, and S is the scattering matrix. Off-diagonal elements of the S-matrix between the channels for which the spin-exchange is allowed contain information about the rate. We calculated inelastic rates for s-wave collisions and neglected the dipole-dipole interaction which could connect partial waves with $\Delta\ell = 2$, such as s- and d-waves.

The calculated inelastic rates for ^{6}Li+^{23}Na mixture are illustrated in Figures 3.9 to 3.13. Several features are shared in all the figures. The maxima of the inelastic rates are the smallest for spin relaxation from channels $1x$, where $x = 2..8$, ranging from 3×10^{-19} to 3×10^{-18} cm^3/s up to between 10-100 G where they are unaffected by magnetic Feshbach resonances. The largest rates of the order of 10^{-12} cm^3/s are obtained for higher-energy hyperfine states, that tend to decay faster, as well as for resonant magnetic fields. In general, resonant profiles can be easily identified and are present in many channels for magnetic fields greater than 10 G. If we assume a typical density of trapped ultracold gas of $n_{\mathrm{Li}} \sim n_{\mathrm{Na}} \sim 10^{12}$ cm^{-3} and volume of 1 mm^3, we can estimate the number of decay events per second from channel α to channel β as $N = n_{\mathrm{Li}} n_{\mathrm{Na}} V G_{\alpha\beta}$. This gives us $10^3 - 10^9$ s^{-1} atom-atom relaxation events for the highest inelastic rates.

Results of a similar analysis of inelastic rates for ^{7}Li+^{23}Na mixture are shown in Figures 3.14 to 3.17. Here, to simplify presentation of the results, we have taken into account only the total inelastic rate, defined as a sum of inelastic decay rates from a particular channel to all channels allowed by the m_f symmetry.

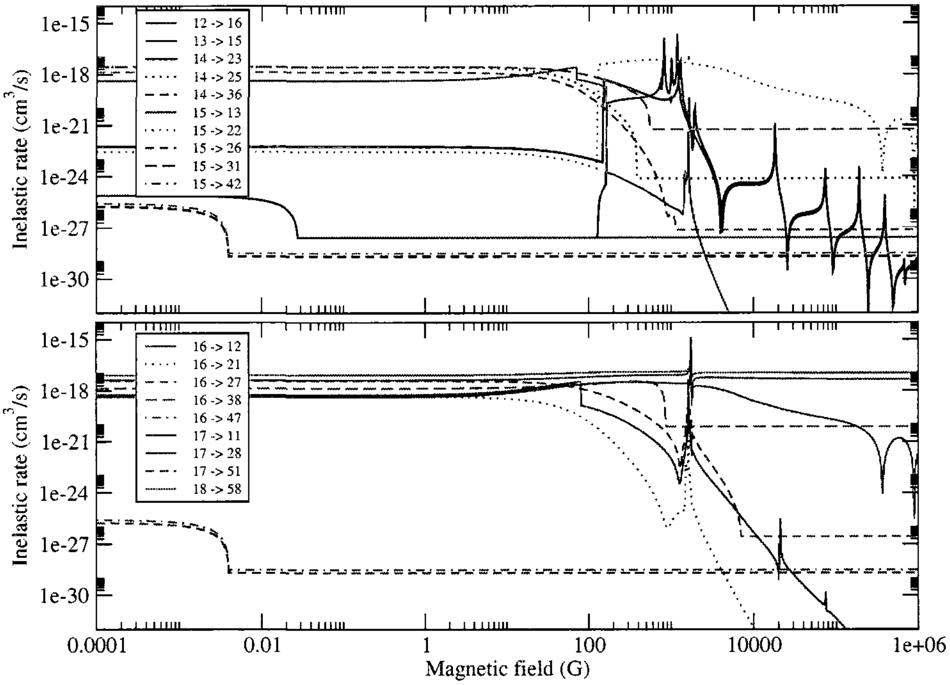

Fig. 3.9: Inelastic rates $G_{\alpha\beta}$ for ^{6}Li+^{23}Na from channels $|11\rangle$ to $|18\rangle$.

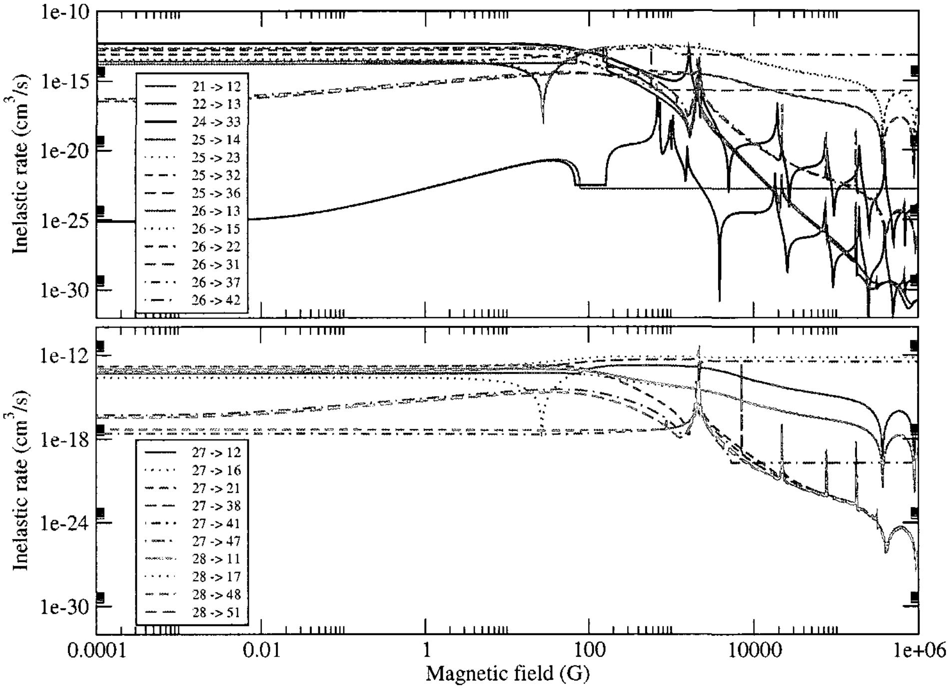

Fig. 3.10: Inelastic rates $G_{\alpha\beta}$ for ^{6}Li+^{23}Na from channels $|21\rangle$ to $|28\rangle$.

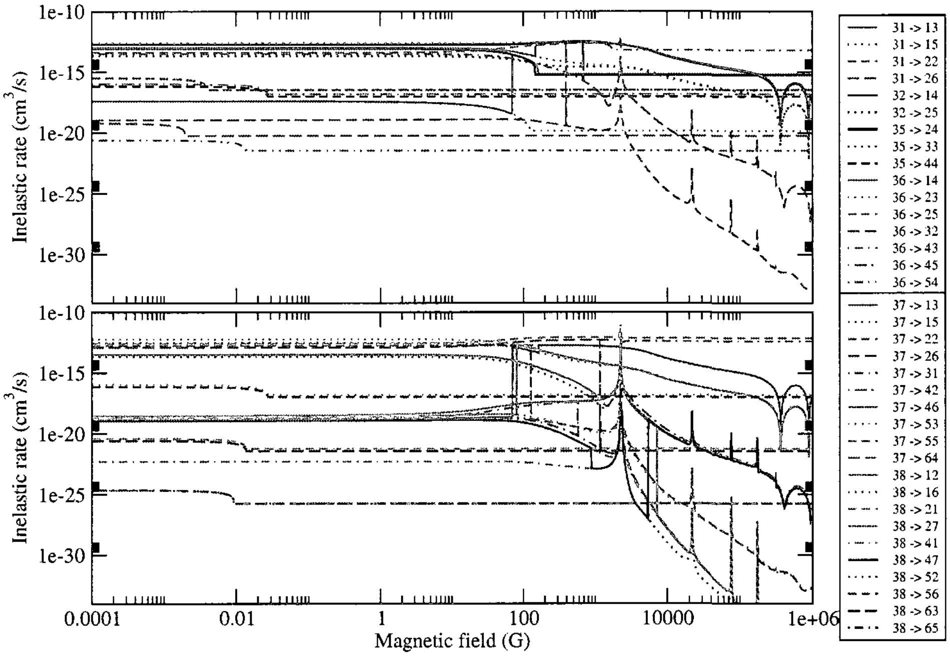

Fig. 3.11: Inelastic rates $G_{\alpha\beta}$ for ^{6}Li+^{23}Na from channels $|31\rangle$ to $|38\rangle$.

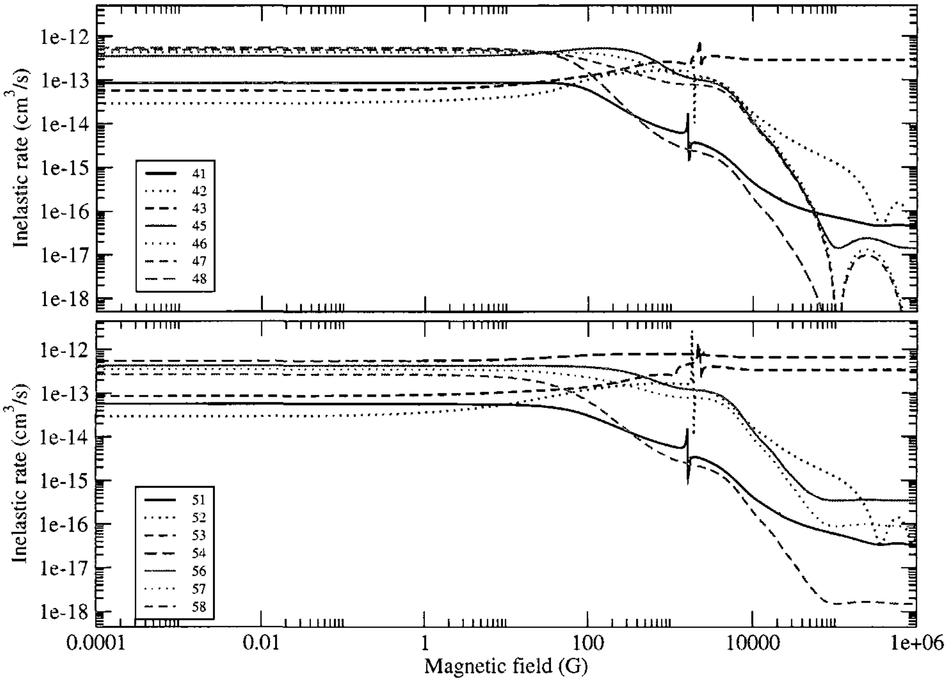

Fig. 3.12: Total inelastic rates $G_{\alpha\beta}$ for ^{6}Li+^{23}Na from channels $|4x\rangle$ and $|5x\rangle$.

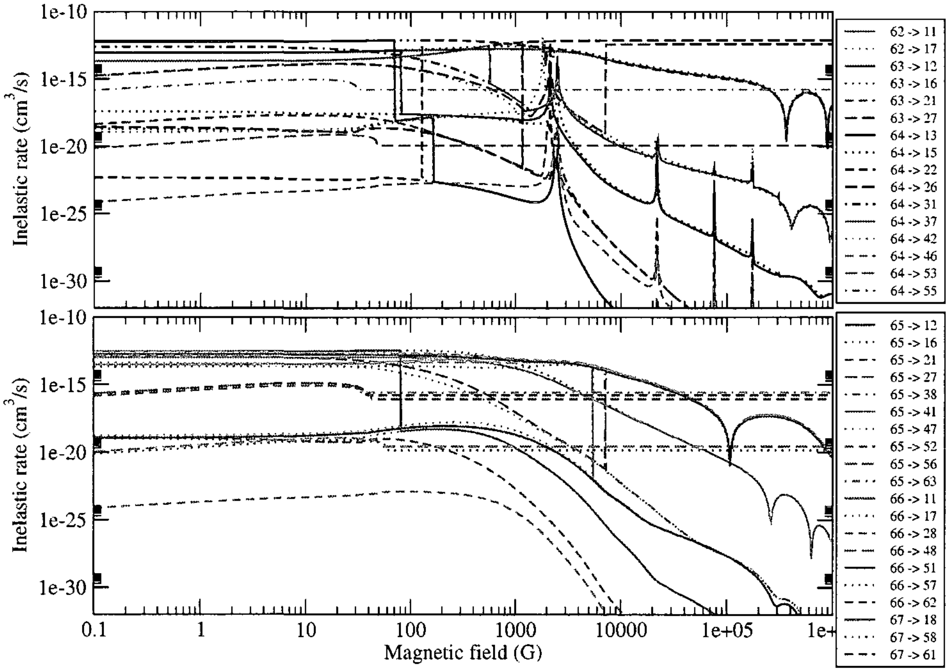

Fig. 3.13: Inelastic rates $G_{\alpha\beta}$ for ^{6}Li+^{23}Na from channels $|61\rangle$ to $|68\rangle$.

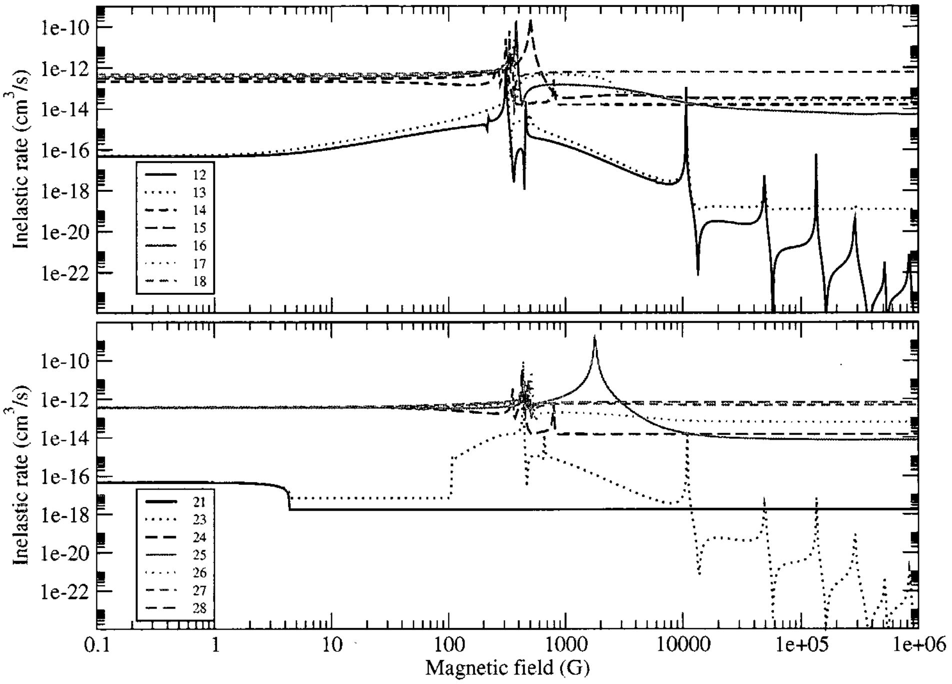

Fig. 3.14: Total inelastic rates $G_{\alpha\beta}$ for ^{7}Li+^{23}Na for channels $|1x\rangle$ and $|2x\rangle$.

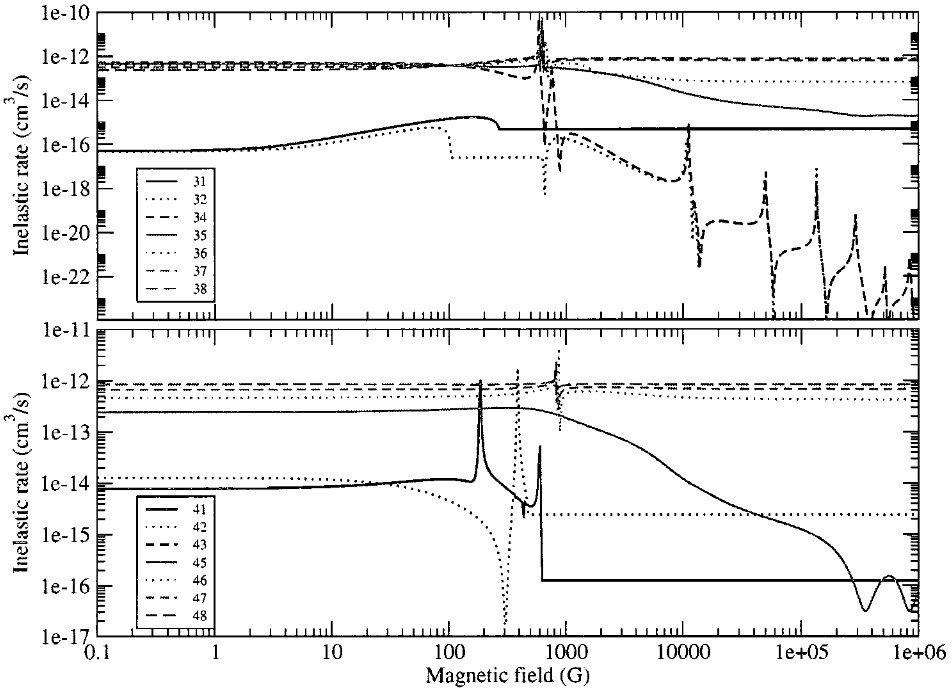

Fig. 3.15: Total inelastic rates $G_{\alpha\beta}$ for ^{7}Li+^{23}Na for channels $|3x\rangle$ and $|4x\rangle$.

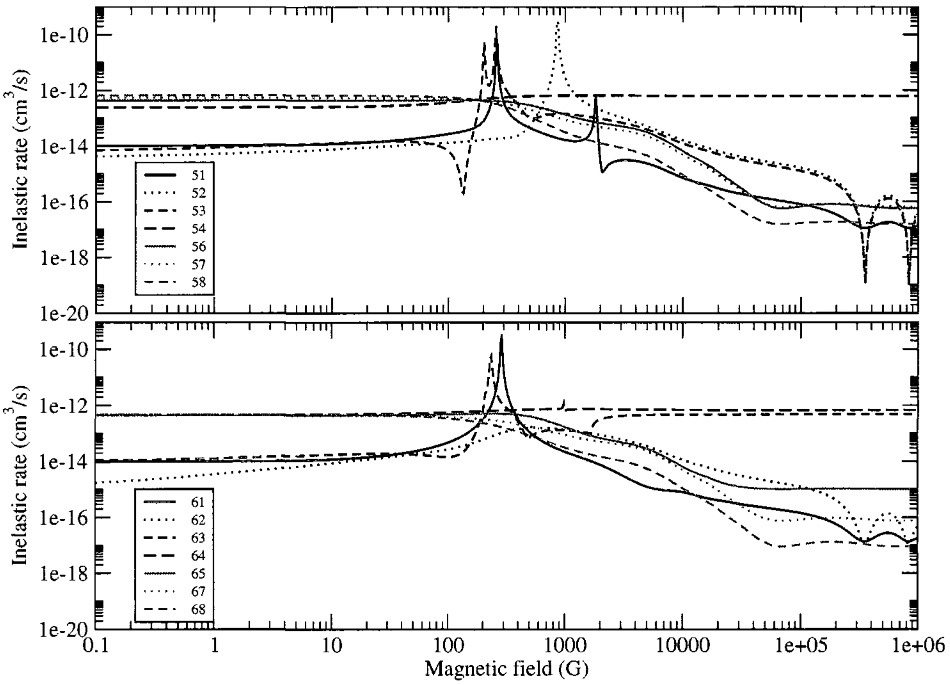

Fig. 3.16: Total inelastic rates $G_{\alpha\beta}$ for ^{7}Li+^{23}Na for channels $|5x\rangle$ and $|6x\rangle$.

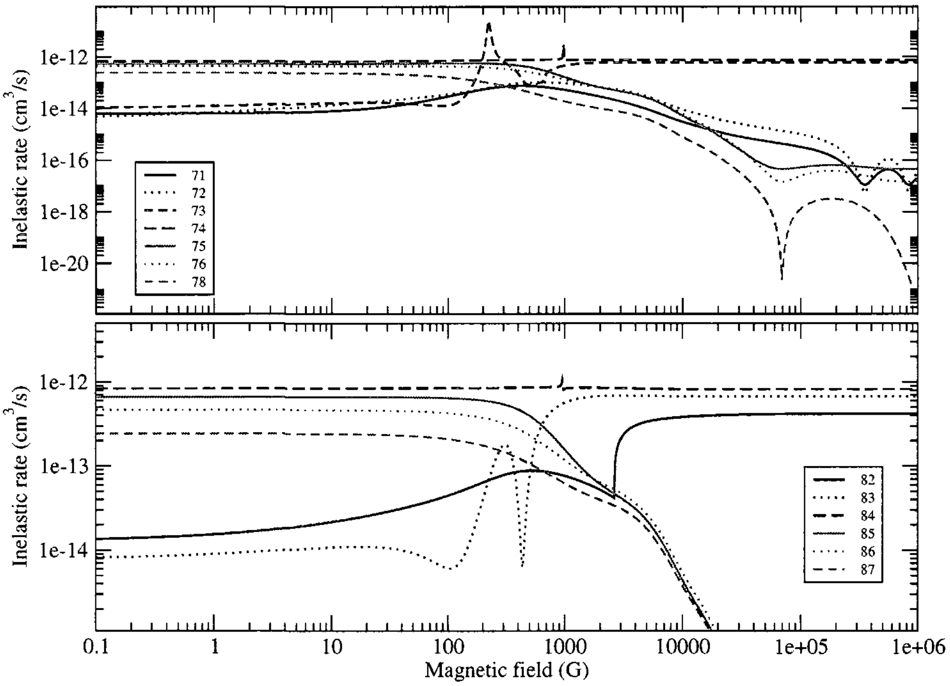

Fig. 3.17: Total inelastic rates $G_{\alpha\beta}$ for ^{7}Li+^{23}Na for channels $|7x\rangle$ and $|8x\rangle$.

3.3 Scattering properties of Li+Rb mixtures

We performed a similar calculation and analysis of scattering properties for an ultracold Li+Rb mixture. Several experimental and theoretical studies of Li+Rb mixtures have been done, resulting in more available information about this system than about Li+Na. Suitable hyperfine states and strategy for cooling ^{6}Li+^{87}Rb were identified [93], followed by a successful effort to produce ultracold Li+Rb molecules [94]. The same group also experimentally determined Feshbach resonances in trapped ^{6}Li+^{87}Rb [74] and ^{7}Li+^{87}Rb [75]. On the theory side, Côté and colleagues [95] studied a sympathetic cooling route that could overcome fermion-hole heating and estimated scattering lengths of ^{6,7}Li+^{87}Rb. Scattering parameters for the Li+Rb system were calculated using variable-phase theory on an *ab-initio* potential [96]. More recently, Li *et al.* performed a coupled-channel calculation of magnetic Feshbach resonances in ^{6}Li+^{87}Rb mixtures [76].

We started from the best currently available molecular potentials, which we adjusted in the same way as it was done for Li+Na (described above), to reproduce known Feshbach resonances. We used the adjusted potentials to calculate scattering lengths, positions and widths of Feshbach resonances in all hyperfine channels and inelastic decay rates. The calculation was done for two different isotopic mixtures, ^{6}Li+^{87}Rb, and ^{7}Li+^{87}Rb, where we used mass-scaling to obtain molecular potentials while neglecting the isotope shift.

3.3.1 Molecular potentials

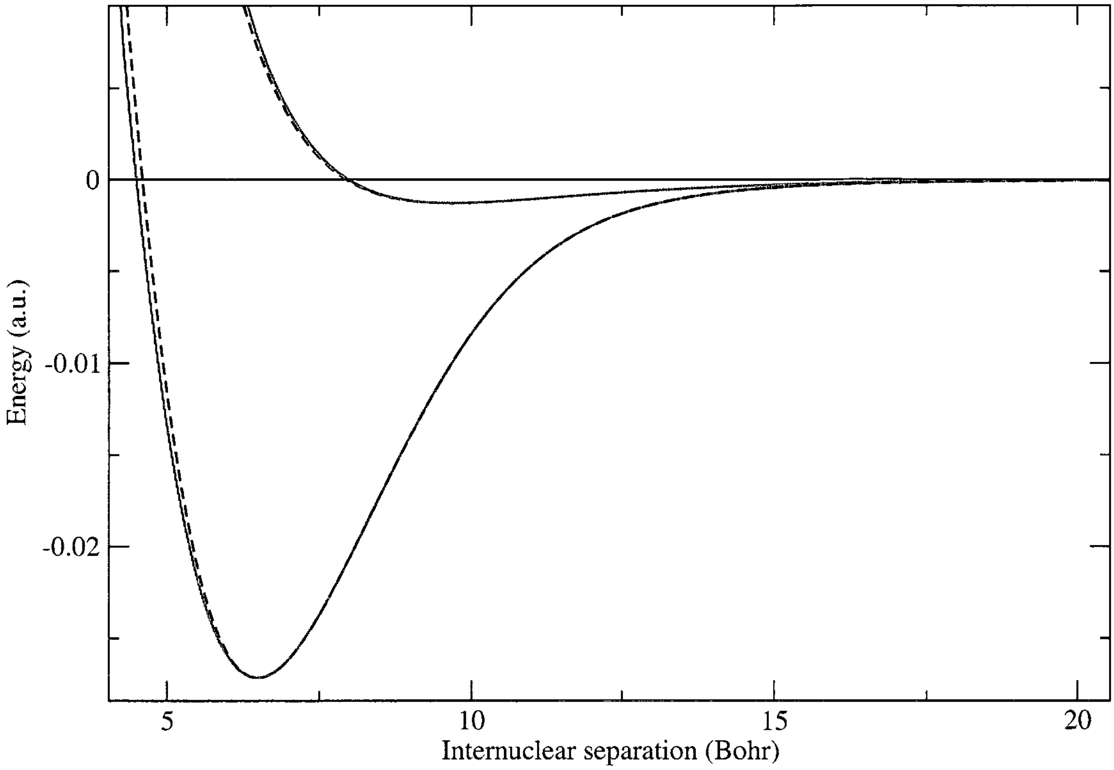

Fig. 3.18: LiRb singlet and triplet potentials used in the calculation. Original (dashed lines) and adjusted potentials (red solid lines) are shown.

We performed a coupled-channel calculation using recently constructed *ab-initio* molecular potential by Korek *et al.* [97], as well as an older *ab-initio* potential by the same author [98]. The older potential was obtained through a full CI calculation, while their newer work focused on modeling the spin-orbit interaction in excited states. The newer potential also has more numerical noise for points at internuclear separations larger than 17 a_0. While we repeated the calculation of basic scattering properties for both potentials, the newer potential required larger adjustments to the inner wall in order to reproduce the correct scattering lengths, hence the decision to use the older potential.

The long-range part of the potential was constructed using dispersion coefficients $C_6 = 2545$, $C_8 = 2.34 \times 10^5$ and $C_{10} = 2.61 \times 10^7$ reported in Refs. [87,88]. The Smirnov-Chibisov form [51], $V_{exch} = AR^{\alpha}e^{-\beta R}$ was used to model the exchange energy with the coefficients $A = 0.0058$, $\alpha = 4.9417$, and $\beta = 1.1836$ (in a.u.). Both singlet and triplet potentials *ab-initio* points were joined to the long range form at $R_0 = 13.5\ a_0$. The potentials are illustrated in Figure 3.18, where both the original and adjusted curves are shown.

3.3.2 Feshbach resonances in ^{6}Li+^{87}Rb

We started by adjusting the singlet and triplet potentials in the same way as for Li+Na. The repulsive wall shifts for the singlet and triplet, s_s and s_t, were varied until we reproduced correct positions of measured Feshbach resonances for the least energetic hyperfine state, $|\alpha\beta\rangle = |11\rangle$ of ^{6}Li+^{87}Rb [74]. The best agreement was for shifts $s_s = -0.1030\ a_0$ and $s_t = 0.0315\ a_0$, and the new potentials were constructed according to Eq. 3.2.1. Positions and widths of Feshbach resonances are very sensitive to molecular potentials: a variation of 1 part in 10^{-4} in the inner wall shift s can significantly influence their positions. For Li+Rb mixtures we did not need to include the magnetic dipole-dipole interaction in order to obtain a good agreement with experimental measurements. Feshbach resonances in the

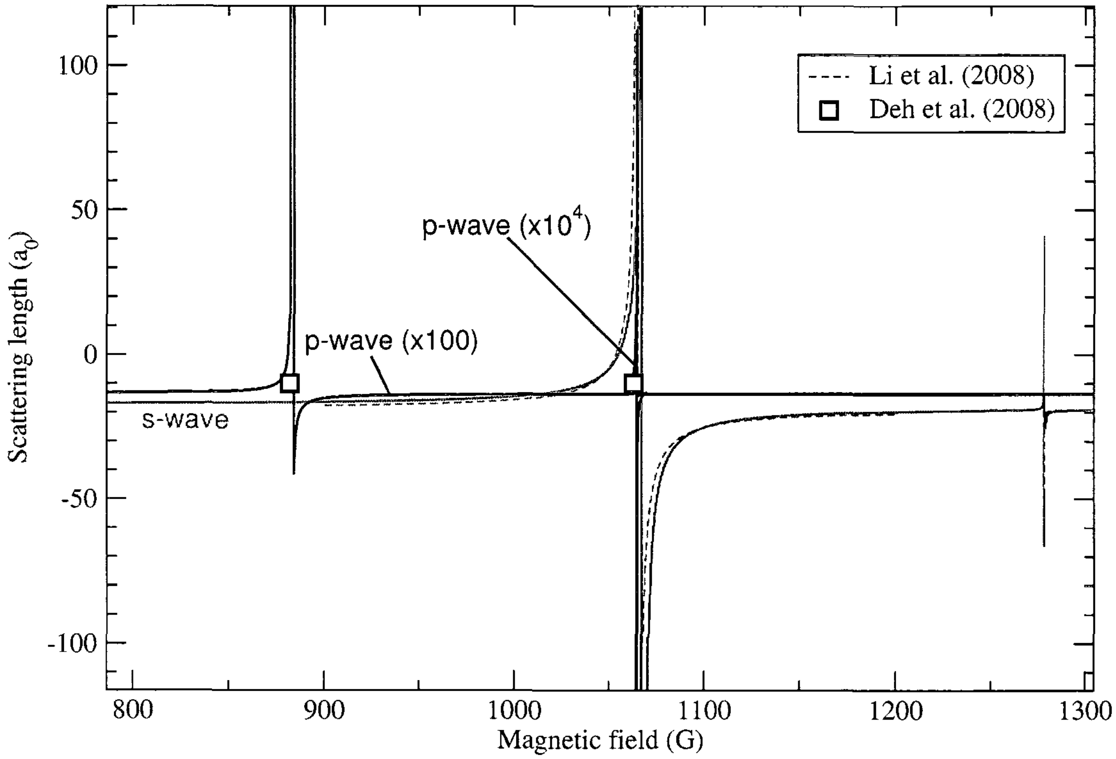

Fig. 3.19: Scattering length for ^{6}Li+^{87}Rb for the entrance channel $|11\rangle$ (solid line). Experimental data (squares) and s-wave Feshbach resonances reconstructed from Li *et al.* (2008) (dashed line) are shown for comparison.

$\lvert\alpha\beta\rangle$	B_0 (G)	ℓ	$\lvert\alpha\beta\rangle$	B_0 (G)	ℓ
11	883	1	31	812	1
	1064	1		964	0
	1067	0		972	1
	1278	0		1158	0
12	891	1	32	976	1
	1068	0		1153	0
	1098	1			
21	776	1			
	923	1			
	927	0			
	1112	0			
	1117	1			
	1331	0			
22	932	1			
	1110	0			
23	1581	1			

Table 3.6: Calculated Feshbach resonances up to 2000 G in ^{6}Li+^{87}Rb for all entrance channels.

channel $|11\rangle$ are illustrated in Figure 3.19 together with previously published data [74,76]. Feshbach resonances found for magnetic fields up to 2000 G are listed in Table 3.6. We have not listed "quasi-resonances" which were included in the table presented by Li *et al.* [76], who reported that they were not able to calculate the width of some resonances because they "exhibited a suppressed oscillation due to comparable coupling to inelastic channels." We indeed found the same features, but decided not to report them as Feshbach resonances because their origin is different and some of them are not really resonances but the result of strong coupling between channels due to an interplay between shape resonances and Feshbach resonances. A detailed theoretical treatment clarifying this point is presented in Marcelis *et al.* [99], while a more formal treatment of general theory, explaining the relation between resonances and the complex poles of the S-matrix and their dynamics, is given in Refs. [39,40].

3.3.3 Feshbach resonances in ^{7}Li+^{87}Rb

To find Feshbach resonances in ^{7}Li+^{87}Rb we performed the calculation with the correct nuclear spin for ^{7}Li and the scaled reduced mass for the system. Feshbach resonances have been detected experimentally in channel $|11\rangle$ of ultracold ^{7}Li+^{87}Rb mixtures [75]. These authors performed a theoretical analysis in the same system using two different models and found large disagreements in predicted positions and widths of the resonances. They have concluded that mass scaling *ab-initio* potentials adjusted to reproduce correctly Feshbach resonances in ^{6}Li+^{87}Rb could not reproduce scattering properties of ^{7}Li+^{87}Rb. A possible explanation is that due to the very small binding energy of the last vibrational level in the ground state of ^{7}Li+^{87}Rb, the system is extremely sensitive to small corrections in the potential. In addition, neither model has been able to assign the experimentally detected resonance at 535 G.

We first calculated the resonances for the elastic channel $|11\rangle$ at the temperature of T = 900 nK, and obtained two s-wave resonances at 669 and 736 G, and two p-wave resonances at 487 and 537 G. A comparison with the published results of two models [75] shows that our resonances are all shifted towards higher magnetic fields by 86, 100, 92, and 99 G for Model I, or 73, 99, 91 and 98 G for Model II (see description of the Models in [75]), starting from the highest magnetic field. We then readjusted the inner wall to try to reproduce the experimental resonances. The exact match with the results of Model II was achieved for the singlet inner wall shift $s_s(^{7}\mathrm{Li}^{87}\mathrm{Rb}) = -0.092\ a_0$, a change of $+0.009\ a_0$ from the value for the ^{6}Li^{87}Rb. However, it was not possible to find parameters of the potential that would correctly reproduce measured Feshbach resonances in both isotopomers. Note that we also did not find the fifth resonance at 535 G.

As a consequence of this analysis we can conclude that either an expansion of the model to include the isotopic shift or, possibly, three-body processes, is necessary, or a reinterpretation of the experiment is required. Since the fifth

$\|\alpha\beta\rangle$	B_0 (G)	l	$\|\alpha\beta\rangle$	B_0 (G)	l
11	388	1	31	559	1
	446	1		605	1
	570	0		651	1
	667	0		733	0
				771	0
21	462	1		869	0
	511	1			
	547	1	41	685	1
	647	0		739	1
	670	0		839	0
	766	0		946	0
22	688	1	42	893	1
	912	0		1114	0
23	1456	0	43	1422	0

Table 3.7: Calculated Feshbach resonances up to 2000 G in ^{7}Li+^{87}Rb for all entrance channels.

resonance at 535 G was not found by us nor by the other two groups [75], it could indicate the latter scenario.

Finally, using the readjusted singlet potential ($s_s = -0.092$) we calculated Feshbach resonances in other channels (Table 3.7).

3.3.4 Inelastic spin-exchange rates

Using the two sets of adjusted molecular potentials for the ^{6,7}Li+^{87}Rb mixtures constructed in previous sections, we calculated their inelastic spin-exchange rates. No previous studies reported the inelastic rates, although Marzok *et al.* [75] discussed a short lifetime of ^{7}Li+^{87}Rb mixture in the $|21\rangle$ state that prevented them from experimentally detecting Feshbach resonances. Furthermore, the unassigned resonance at 535 G in the same system might be caused by a three-body process or 'contamination' of the prepared $|11\rangle$ state with one or more higher-energy channels due to, for example, the impurity of the rf filtering. Comparing inelastic rates for different channels could help distinguish among these processes.

Calculated inelastic rates for ^{6}Li+^{87}Rb are illustrated in Figures 3.20 to 3.22, and for ^{7}Li+^{87}Rb in Figures 3.23 to 3.26. For each channel only the total inelastic rates, which we find by summing all nonzero decay rates for that particular channel, are shown.

The rates exhibit several universal features. In ^{6}Li+^{87}Rb, for magnetic fields below 1 G, the rates are mostly unaffected by the field, except in case of the least energetic channels $|12\rangle$, $|13\rangle$, and $|21\rangle$. The rate for channels $|12\rangle$ and $|13\rangle$ is identical in the low-field region, where it first decreases from roughly 2.6×10^{-15} cm^3/s until it becomes about 3.5×10^{-16} cm^3/s for $B = 0.027$ G, then remains constant until 76 G when it suddenly increases by a factor of 100. The other common property is that the rates are several orders of magnitude higher for higher channels. For channels $|1\beta\rangle$, this ratio is, on average, about 10^4. The experimentally attainable region below 10^4 G contains numerous resonances which are reflected in the inelastic rates. The smallest rates for such magnetic fields, aside from the channels which do not decay via two-body spin-spin relaxation, range between 2.6×10^{-15} and 10^{-14} cm^3/s. If we assume a high density of 10^{12} atoms cm^{-3} of both species and a trap volume of 1 mm^3, these rates correspond to about $10^6 - 10^7$ interspecies relaxations per second, resulting in very long lifetimes. In realistic conditions we can expect much lower densities of atoms in a particular combination of hyperfine states, easily reducing this number by several orders of magnitude.

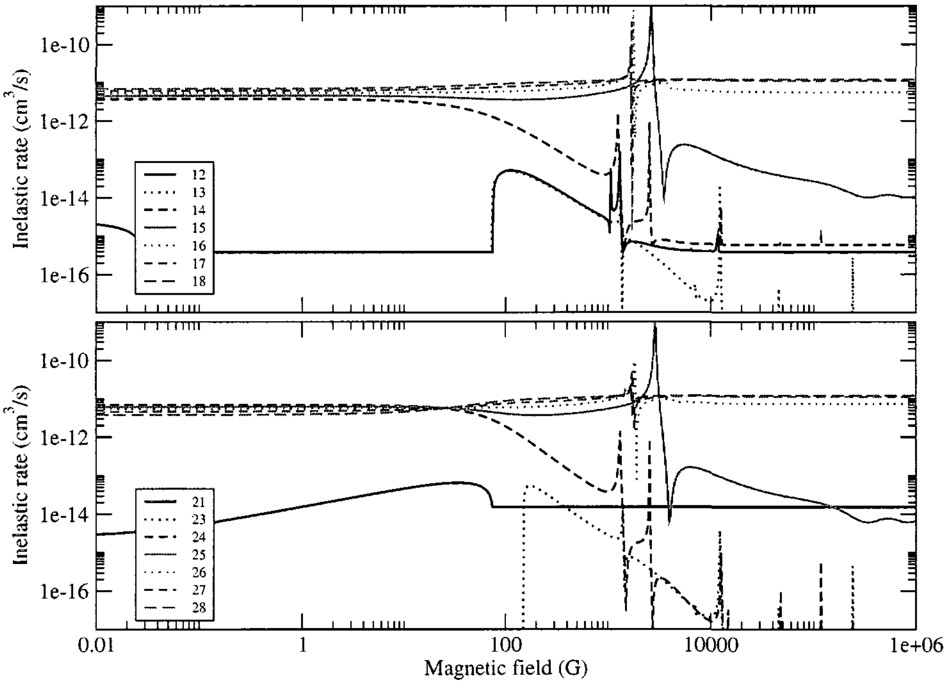

Fig. 3.20: Total inelastic rates $G_{\alpha\beta}$ for ^{6}Li+^{87}Rb for channels $|1x\rangle$ and $|2x\rangle$.

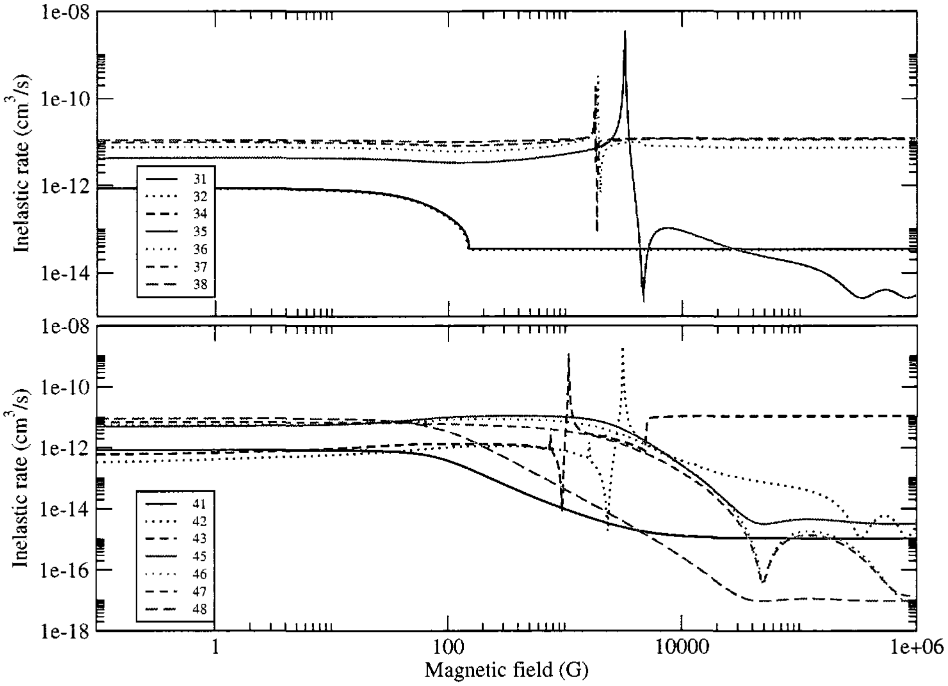

Fig. 3.21: Total inelastic rates $G_{\alpha\beta}$ for ^{6}Li+^{87}Rb for channels $|3x\rangle$ and $|4x\rangle$.

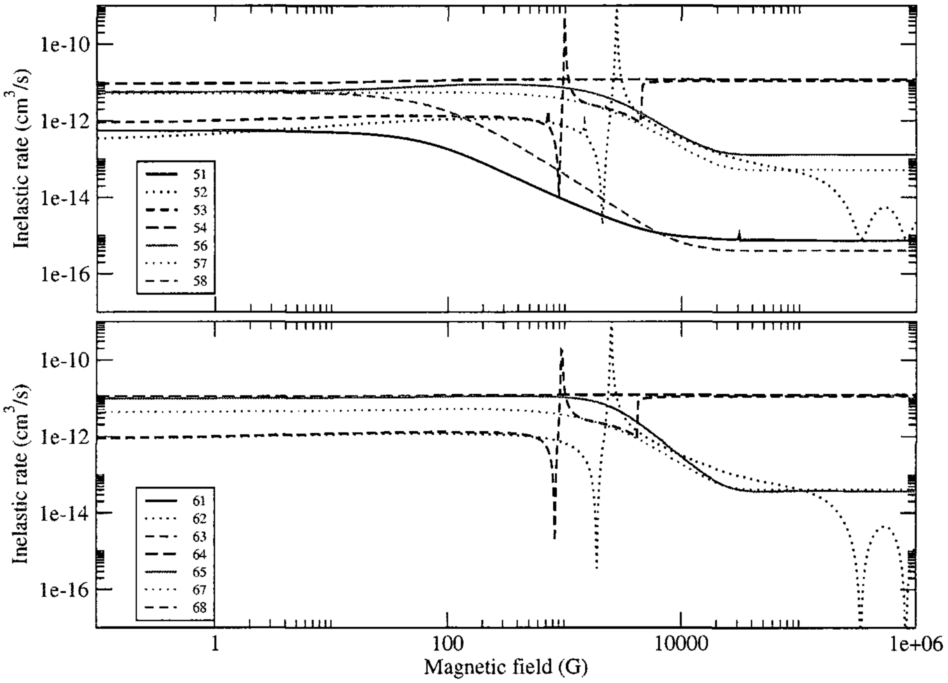

Fig. 3.22: Total inelastic rates $G_{\alpha\beta}$ for ^{6}Li+^{87}Rb for channels $|5x\rangle$ and $|6x\rangle$.

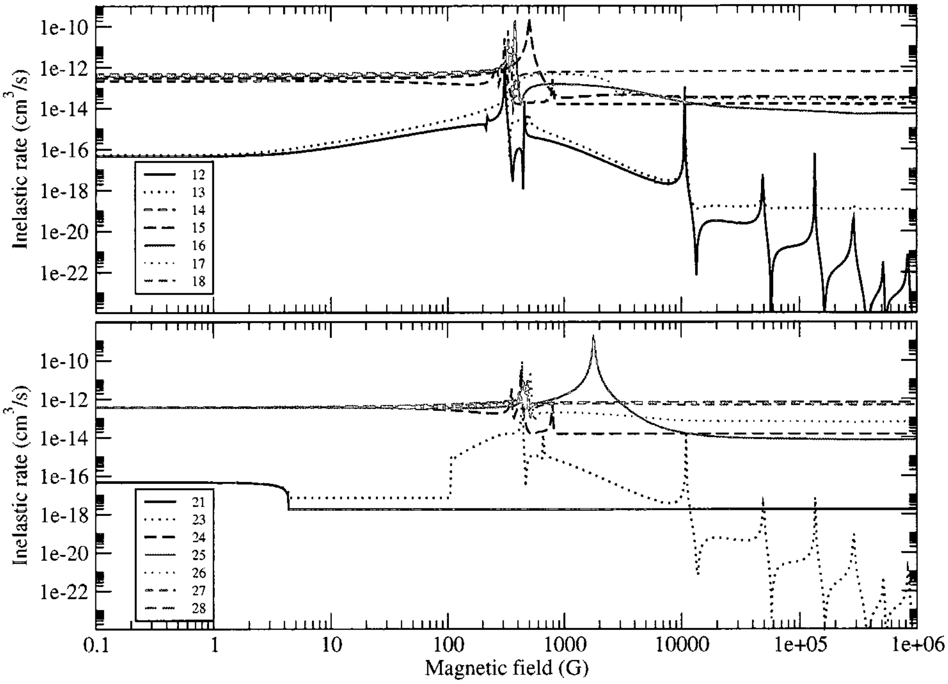

Fig. 3.23: Total inelastic rates $G_{\alpha\beta}$ for ^{7}Li+^{87}Rb for channels $|1x\rangle$ and $|2x\rangle$.

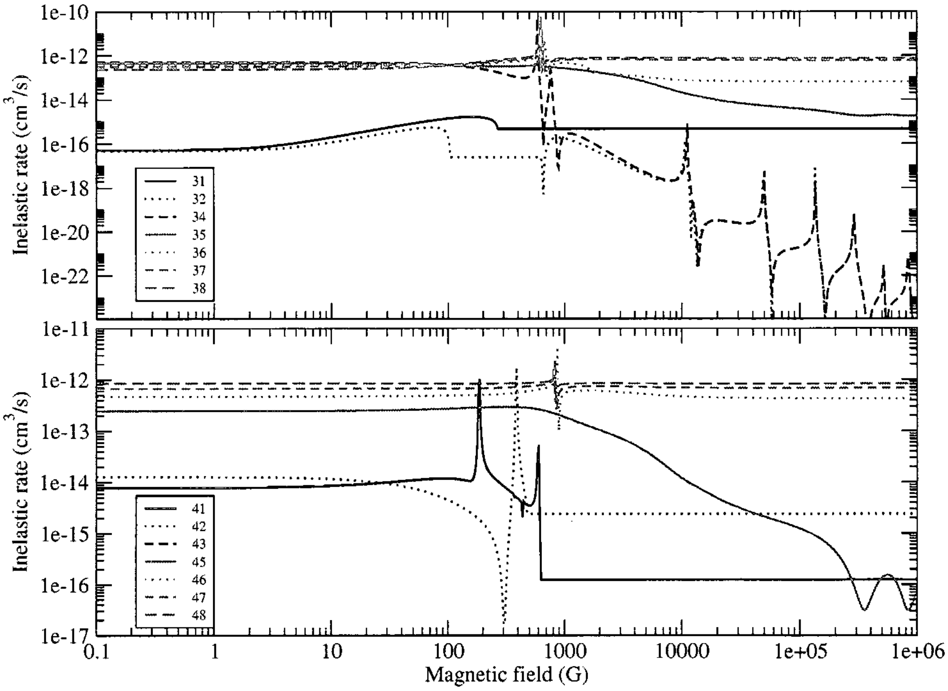

Fig. 3.24: Total inelastic rates $G_{\alpha\beta}$ for ^{7}Li+^{87}Rb for channels $|3x\rangle$ and $|4x\rangle$.

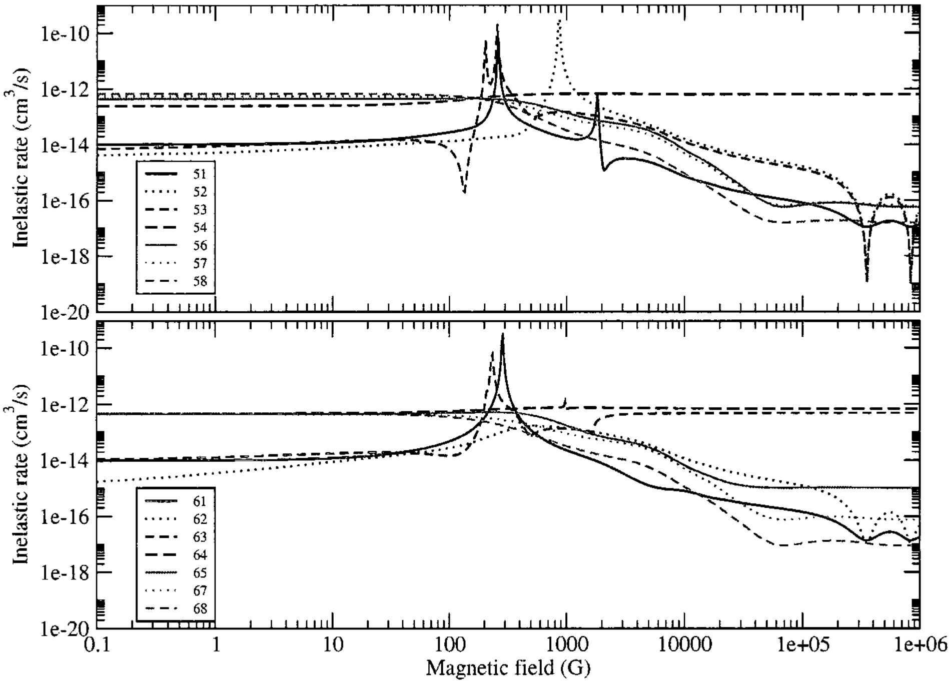

Fig. 3.25: Total inelastic rates $G_{\alpha\beta}$ for ^{7}Li+^{87}Rb for channels $|5x\rangle$ and $|6x\rangle$.

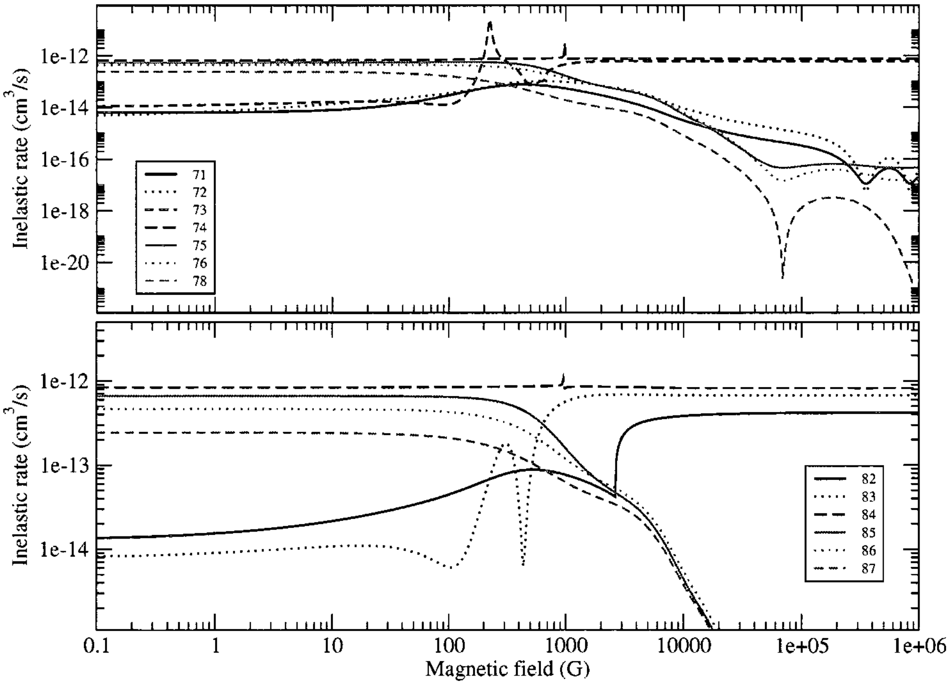

Fig. 3.26: Total inelastic rates $G_{\alpha\beta}$ for ^{7}Li+^{87}Rb for channels $|7x\rangle$ and $|8x\rangle$.

3.4 Temperature dependence of Feshbach resonances

Feshbach resonances are usually studied in the ultracold regime at near-zero energy. They also play a very important role in BECs, where the effective temperature of the system is below the condensation point [42,63,9]. In such studies, the scattering properties are assumed to be largely independent of temperature and the scattering cross section for a pair of atoms is taken to be the same as for a hypothetical hard-sphere, $\sigma = 4\pi a^2$ for distinguishable particles, where a is the s-wave scattering length.

In our calculations presented in the previous sections we assumed the temperature of 900 nanokelvin to closely match the experimental conditions near the degenerate regime at which Stan *et al.* [65] studied Li+Na mixtures. However, the experiments performed to determine properties of Feshbach resonances have been conducted at temperatures sometimes as high as 15 μK [74,94,100], due to the technical difficulties related to cooling. For example, in the mentioned experiments ^{6}Li is sympathetically cooled with ^{87}Rb atoms, and the small scattering lengths result in long cooling times. In such systems it is impractical to lower the temperature further via sympathetic cooling. The same authors observed collapse of the ^{7}Li atomic cloud below the critical temperature for condensation, $T = 1.5$ μK, which is related to the negative scattering length of ^{7}Li. Finally, experimental determination of the temperature of the gas cloud is often conducted independently of the trap loss measurements used to identify Feshbach resonances, resulting in a possible uncertainty in the reported temperature.

In order to assure that the scattering properties, including the positions of Feshbach resonances, remain invariant or change very little within the temperature range of < 10 nK to 100 μK, as is often assumed, we analyzed the scattering cross section as a function of temperature and magnetic field. In our analysis we took extra care to study the temperature dependence for nearly-resonant magnetic field, $B = B_0 - \epsilon$ Gauss, where ϵ is a small number such that the scattering length is increased a few orders of magnitude.

To study this dependence we first calculated the scattering cross section for ^{6}Li^{23}Na as a function of temperature for several values of the magnetic field B close to the Feshbach resonance at 795.6 G, as well as for $B = 0$. This particular resonance is the broadest in the entrance channel $|11\rangle$ which we analyzed, making the gradient of the scattering length in its vicinity smaller and more suitable for illustrating dependence on the magnetic field. Calculated s-wave cross sections are illustrated in Figure 3.27. From this graph we can see that for magnetic fields far from the resonance (thick black line) the cross section remains constant and is approximated well by the trivial hard-sphere model up to about 1 μK. As we approach the resonance, however, this approximation becomes invalid for lower temperatures. At $B = 795.5$ G, within 0.1 G of the resonance at 795.6 G, the temperature change from $T = 1$ μK to $T = 10$ μK results in reduction of the cross section by 5%, while at $T = 45$ μK the reduction increases to 14 %. At magnetic

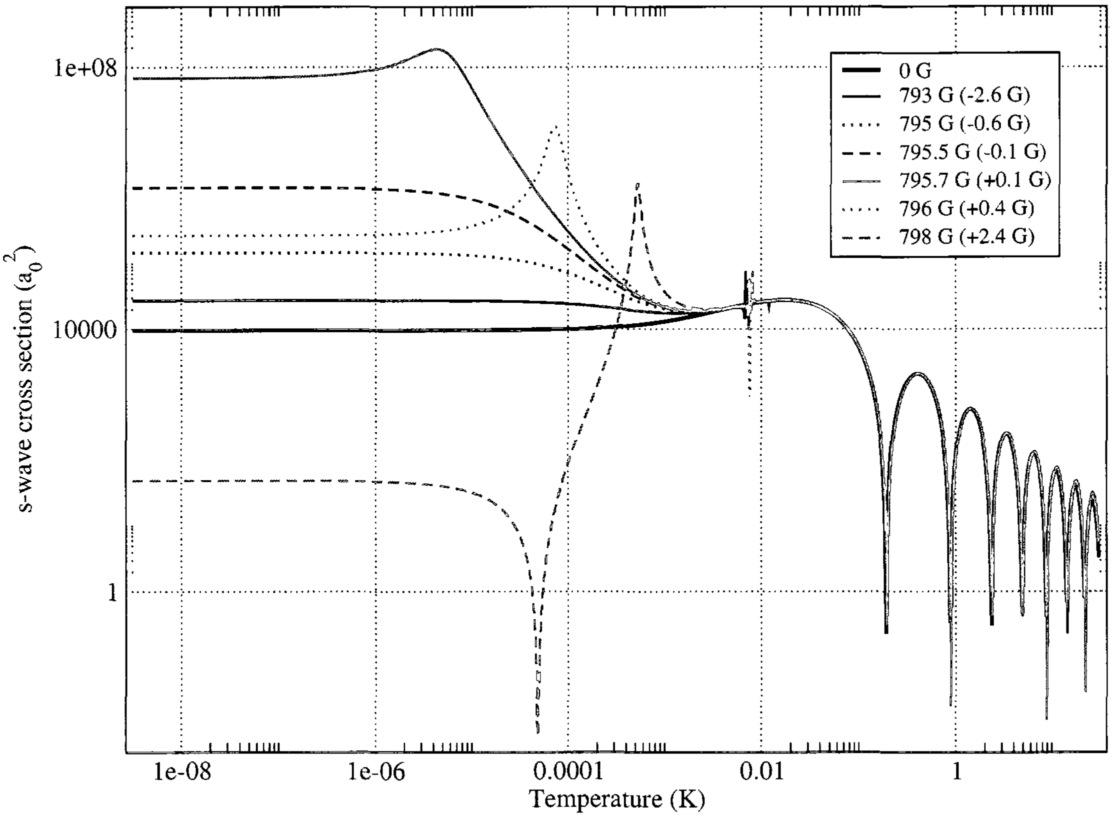

Fig. 3.27: s-wave cross section vs. temperature for ^{6}Li+^{23}Na, entrance channel $|11\rangle$. Cross sections were calculated for several values of magnetic field B in the vicinity of the Feshbach resonance at 795.6 G, and for $B = 0$ G.

fields slightly past the resonance the effect is even more pronounced (red curves in Figure 3.27). For such magnetic fields the cross section remains constant only up to about 0.01 μK, deep inside the ultracold regime. As the temperature increases from $T = 1$ μK to $T = 45$ μK, the cross section doubles. This could prove to be a non-negligible temperature-related property of Feshbach resonances which was not included, to the best of our knowledge, in any of the previous studies. For temperatures greater than about 10 mK, outside of the "cold regime", the cross section is unaffected by the magnetic field and exhibits a well-known behavior [38].

Next we consider the effect of higher partial waves in the ultracold regime. In Figure 3.28 the scattering cross section is shown for the first four partial waves of the same system. The cross sections were calculated for the zero-field case (solid curves) and for magnetic field $B = 795.5$ G (dashed curves), within 0.1 G of the Feshbach resonance. To simplify the calculation we neglected the dipole-dipole interactions which couple partial waves with $\Delta\ell = 2$, such as s- and d-wave, and perturbes their eigenenergies by several percent. Instead, we focus here on the temperature dependence of higher partial waves.

From Figure 3.28 we can easily see that the relative importance of partial waves in collisions at temperatures around 1-10 μK, at which Feshbach resonances are observed, is negligible. The p-wave cross section in this regime is about 1 part in 10^9 of the s-wave cross section and it increases to about 0.1 % of the

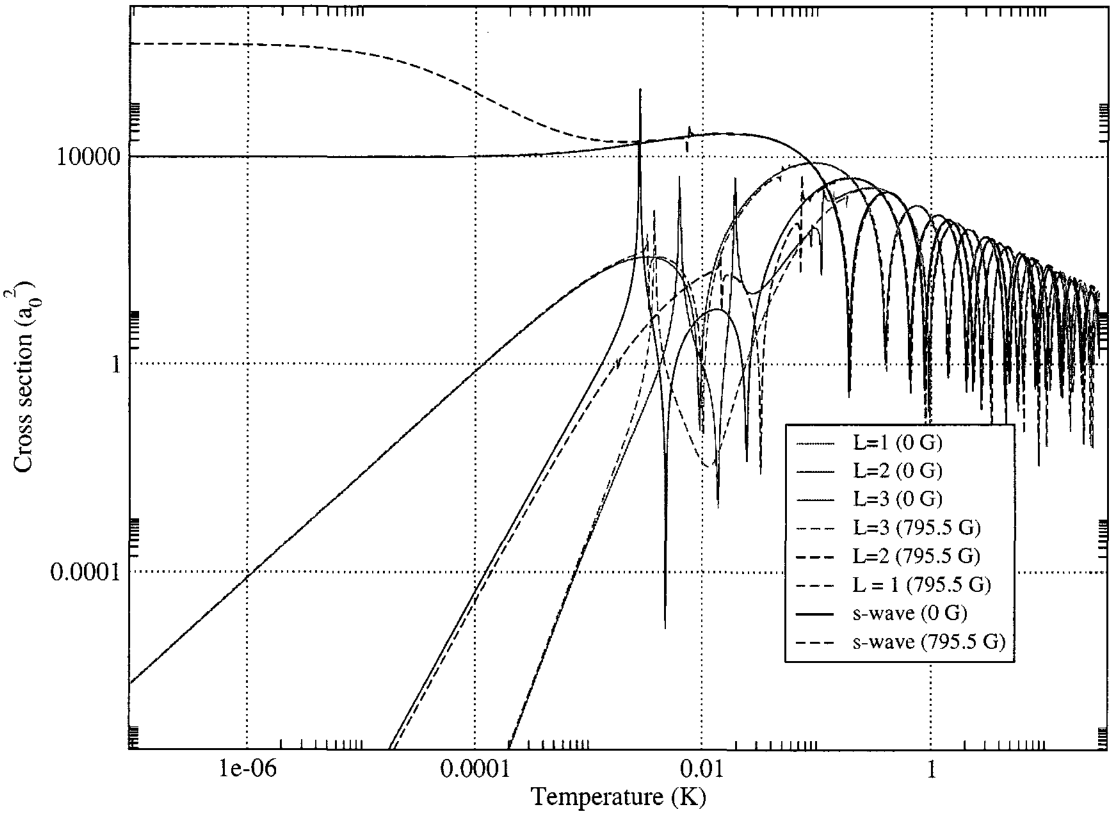

Fig. 3.28: Temperature dependence of scattering cross section for the first four partial waves in the lowest hyperfine channel of ^{6}Li+^{23}Na. The cross section for $B = 0$ G (solid lines) and $B = 795.5$ G (dashed curves) is shown.

s-wave cross section at 1 mK. Other partial waves play an even smaller role. Above 1 mK, their contribution becomes resonantly enhanced for a set of narrow temperature ranges, and above 0.1 K they start to contribute significantly to the total cross section. Close to the resonance at 795.6 G (dashed lines), the cross section of partial waves becomes strongly affected for temperatures between 1 mK and 100 mK, while remaining mostly unaffected in other regions. This is a different behavior than the one observed for the s-wave cross section, which is also illustrated in the same graph. This calculation has clearly shown that in the ultracold regime higher partial waves do not affect significantly collisional properties, even for nearly-resonant magnetic fields.

To directly explore the temperature dependence of Feshbach resonances we performed a direct calculation of s-wave scattering length for a range of temperatures. The results are illustrated in Figure 3.29. At the collision energy of 10^{-5} K or below there is no observable difference in the scattering length. The difference increases to about 2% at 100 μK, while at the temperature of 1 mK all resonances become shifted by about 4 G to higher magnetic fields. Finally, at 10 mK this shift becomes larger than 40 G. Based on the temperature dependence of the cross section (Figure 3.27), we expect the positions of the Feshbach resonances to be affected by the temperature. However, numerical results indicate that in the ultracold regime, at or below 10 μK for Li+Na, the scattering length and structure of Feshbach resonances remains unaffected by the temperature changes.

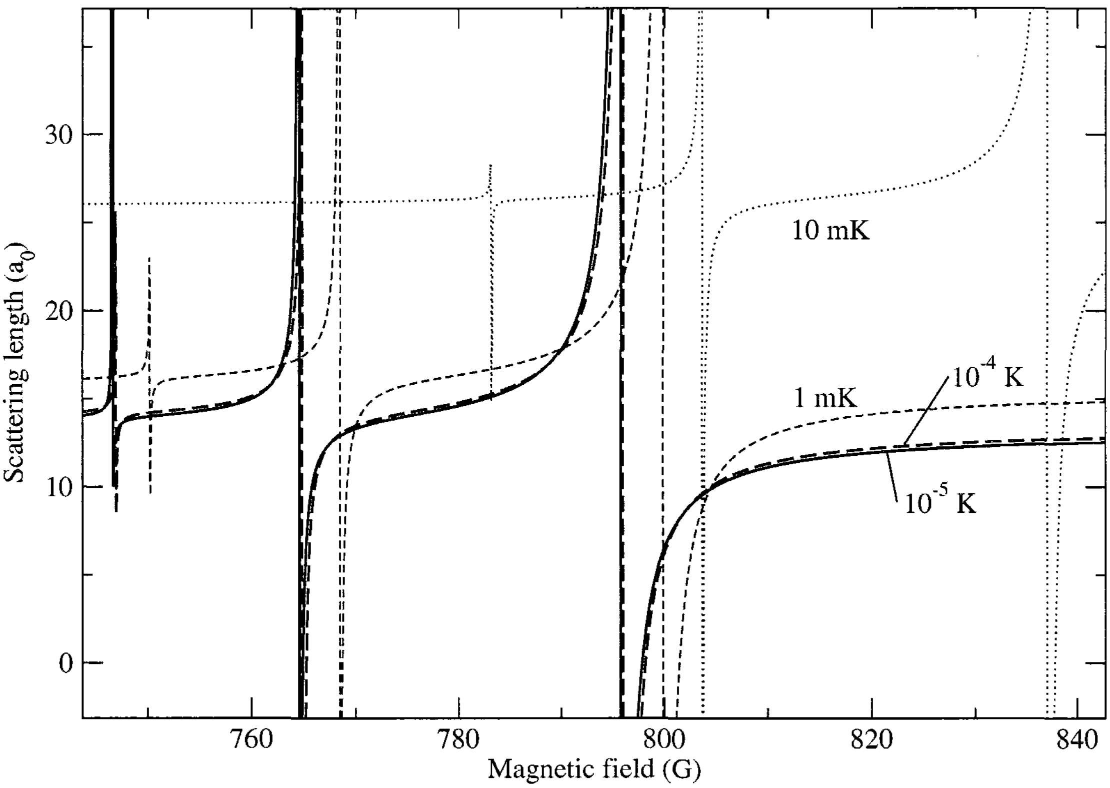

Fig. 3.29: Temperature dependence of the scattering length near Feshbach resonances in the lowest hyperfine channel of ^{6}Li+^{23}Na.

Finally, while we discussed temperature effects on Feshbach resonances and scattering properties in Li+Na, a similar analysis can be carried out for other alkali dimers. In our analysis of Li+Rb system, we originally considered the temperature of 900 nK or 1 μK. However, as we were trying to explain the disagreements of our results, obtained by mass scaling from ^{6}Li+^{87}Rb to ^{7}Li+^{87}Rb, and the reported Feshbach resonances [75], we varied the temperature over a broad range, up to 10 mK. We estimated that variations of at most 2 and 4 G for the first and second resonances in the channel $|11\rangle$, respectively, can be attributed to the temperature effects. Nevertheless, we believe that this is a measurable effect which should be taken into account in experiments with alkali dimers and similar mixtures at temperatures approaching 10 μK.

Chapter 4

Production of ultracold molecules using Feshbach-optimized photoassociation

In the previous chapter, we calculated positions and characteristics of Feshbach resonances in different heteronuclear mixtures and adjusted molecular potentials to correctly reproduce their scattering properties. From a theoretical perspective, it was sufficient to calculate the S-matrix for the collision. In this chapter, we instead focus on the wavefunctions of open and closed collisional channels, as our goal is to calculate photoassociative formation rates of molecules for different rovibrational levels.

We show that Feshbach-optimized photoassociation (FOPA) can be used to enhance photoassociative formation rates by several orders of magnitude and allow access to otherwise inaccessible rovibrational levels. We illustrate this on ultracold mixtures of Li+Na and Li+Rb, although the method is more general and applies to any system in which Feshbach resonances exist. Two different FOPA schemes are considered: the single-photon FOPA from the continuum and a 2-photon FOPA scheme. The 1-photon scheme can be used to directly access low-lying vibrational levels in the ground state of polar molecules, while the 2-photon scheme is more general and applicable to any molecule in which accessible Feshbach resonances exist.

A part of the work presented in this chapter was published in Ref. [67].

4.1 Techniques for creating ultracold molecules - an overview

Ultracold molecules offer a broad variety of applications, ranging from metrology to quantum computing. However, forming "real" ultracold molecules, *i.e.*, in deeply bound levels, remains a difficult proposition. In recent years several techniques, ranging from Stark decelerators to buffer-gas cooling, have been developed to obtain cold molecules [12]. Such molecules are interesting for a range of applications [68] in metrology, high precision molecular spectroscopy, or quantum computing [101]. However, forming stable ultracold molecules in deeply bound levels remains a challenge: most approaches produce temperatures still considered too hot (roughly 100 mK - 1 K). To reach the ultracold regime (below 1 mK), direct laser cooling of molecules is usually not effective due to their rich and complex level structure [102,103]. Instead, it is possible to create ultracold molecules starting from ultracold atoms, via photoassociation (PA) or "magnetoassociation" (MA). These approaches are different: PA occurs when two colliding atoms absorb a photon to form a molecule [68], while MA takes advantage of magnetically tuned Feshbach resonances to convert an entire atomic gas into a molecular gas and back [9].

Over the last decade, PA has been widely used to study long range molecular interactions and to probe ultracold gases [68]. Magnetoassociation has been used to realize molecular condensates [63,64,104,105] and investigate the BEC-BCS crossover regime [106–109]. However, both methods usually produce molecules in highly excited states. According to the Franck-Condon principle, electronic transitions in PA occur at large interatomic distances, leading to molecules in high rovibrational levels that can either decay by spontaneous emission or collisional quenching. To stabilize the molecules in their ground potentials, one could use two-photon schemes [69,110], or excited molecular states with long-range wells that increase the probability density at short range. The latter solution requires the existence of double-well molecular potentials [102] and cannot be easily generalized. In MA, molecules are produced by sweeping the magnetic field through a Feshbach resonance, which occur when the energy of a colliding pair of atoms matches that of a bound level associated to a closed channel. The molecules produced by MA are in the uppermost states near dissociation and thus very extended and fragile [9].

4.2 FOPA rates for forming ultracold $^{6}\mathrm{Li}^{23}\mathrm{Na}$ molecules

We describe our investigation of a novel Feshbach-optimized photoassociation scheme that employs a magnetic Feshbach resonance [9] to enhance the probability density at short range and allows transitions to deeply bound vibrational levels. Feshbach resonances are commonly found in both homonuclear and heteronuclear systems with hyperfine interactions. We focus our attention on heteronuclear systems for which the presence of a permanent dipole moment allows transitions from the continuum directly to a rovibrational level v of the ground electronic molecular states [70]. Such a PA scheme is shown in Figure 4.1.

Feshbach resonances and PA have been proposed to associate atoms [111] and convert an atomic into a molecular BEC [112]. However, in contrast with previous proposals [113,114], FOPA takes advantage of the entire wavefunction in a full quantum coupled-channel calculation, and is thus more general than the Franck-Condon principle.

Our choice of heteronuclear LiNa as a system to illustrate FOPA represents a continuation of our previous work: we studied scattering properties and magnetic Feshbach resonances in ultracold Li+Na heteronuclear mixtures (see Chapter 3). As a result, we have obtained adjusted molecular potentials that reproduce well both the scattering length and positions and widths of Feshbach resonances. We use these adjusted singlet and triplet potentials in the calculation of photoassociation rates conducted in this chapter.

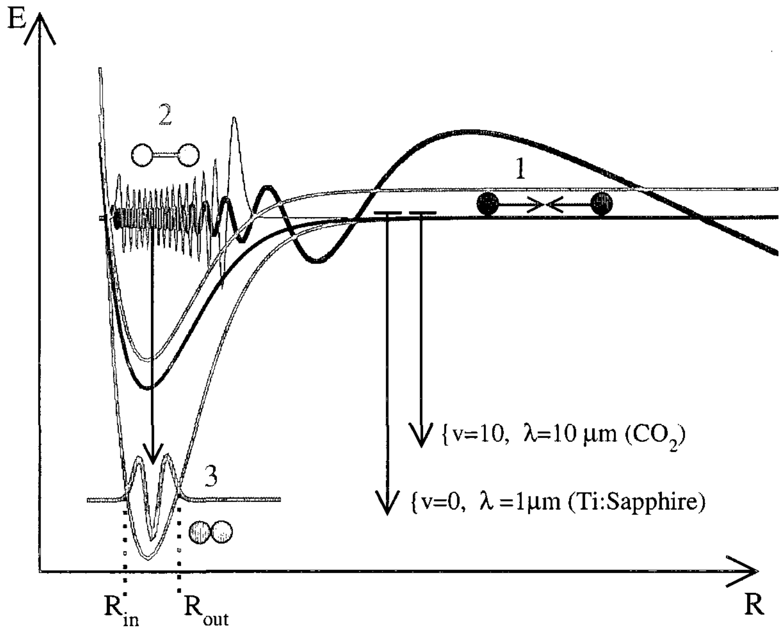

Fig. 4.1: FOPA scheme: colliding atoms (1) interact via open (blue) and closed (green) channels due to hyperfine interactions. A Feshbach resonance occurs when a bound level (2) (green wavefunction) coincides with the continuum state (blue wavefunction). A photon (wavelength λ) can associate the atoms into a bound level v (3) of the ground state potential (red) with inner and outer classical turning points R_{in} and R_{out}.

We consider the single-photon process illustrated in Figure 4.1, where two ultracold atoms described by the "Feshbach state" are photoassociated into a deeply bound heteronuclear molecule in its ground electronic state, $X^1\Sigma^+$. The continuum "Feshbach state" has an average energy of the surrounding gas and consists of one or more hyperfine components which are non-degenerate for $B > 0$. In general, the Feshbach state wavefunction is dependent on the magnetic field and in the vicinity of a resonance its structure changes dramatically, which we can exploit to enhance molecular formation rates.

To model this process and calculate the molecular formation rates for ^{6}Li^{23}Na molecules we rely on the theory presented in section 2.6. We assume that Li and Na atoms are initially in hyperfine states, $^6\mathrm{Li}(f = \frac{1}{2}, m_f = -\frac{1}{2})$ and $^{23}\mathrm{Na}(f = 1, m_f = -1)$. In the channel notation introduced earlier, this corresponds to the entrance channel $|\alpha = 2, \beta = 3\rangle$. We selected this particular entrance channel for illustrating Feshbach-optimized photoassociation since it has two broad, distinctly separated Feshbach resonances. The channel $|11\rangle$ would be a more likely choice in a photoassociation experiment, but the lowest-field resonance at about 746 G is very narrow and difficult to reproduce correctly in our calculation unless a very large number of grid points is used, which is possible but impractical. In the entrance channel $|23\rangle$ eight hyperfine channels with the total projection $m_f = -3/2$ are coupled, and there are two s-wave Feshbach resonances at 1081 and 1403 Gauss, as well as two p-wave resonance at 845 and 1053 Gauss (see Chapter 3, Figure 3.6 and Table 3.4). The s-wave resonances are, however, much wider and the p-wave resonances can be neglected.

Once we have obtained the continuum "Feshbach wavefunction," it is rather straightforward to calculate the photoassociation rate. The wavefunctions $|\psi_{v,J}\rangle$, for bound rovibrational target levels (v, J), can be calculated by diagonalizing a simple one-channel problem with an appropriate molecular potential. Our choice

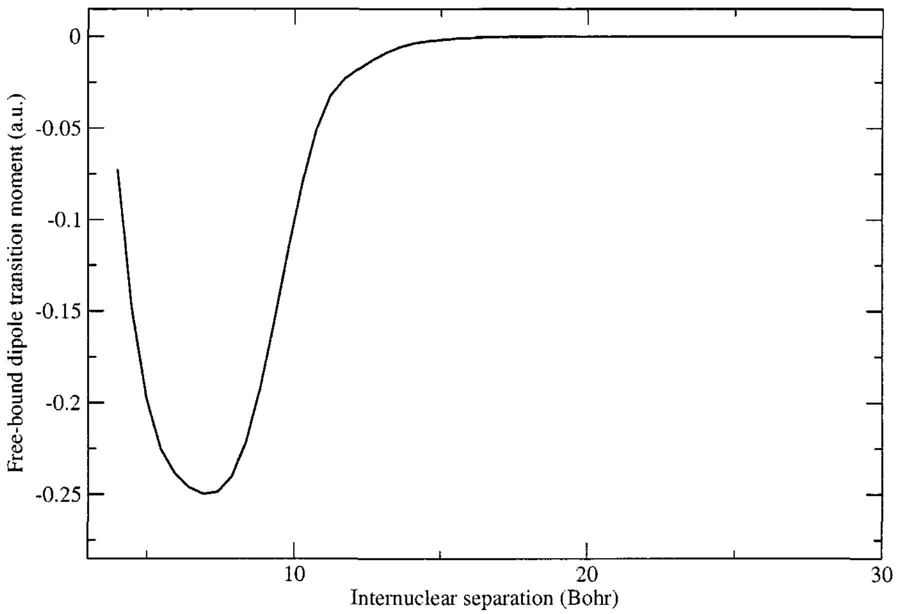

Fig. 4.2: Free-bound dipole moment $D(R)$ for the ground rovibrational state of LiNa molecule.

of the mapped Fourier grid method [73] is particularly suitable for this task, as it allows us to obtain an entire set of eigenvectors and eigenvalues in a single run.

To make the calculated FOPA rates more realistic, we use the transition dipole moments for LiNa molecule calculated by the Orsay group [115] (Figure 4.2). In general, transition dipole moments $D(R)$ are not known for majority of dipolar transitions in heteronuclear molecules. In the first approximation, it is often assumed that the free-bound dipole moment is a constant equal to the asymptotic (atomic) values. However, more realistic photoassociation rates can be obtained if the functional dependence of the dipole moment on the internuclear separation is known. This is particularly important for lower vibrational levels at small internuclear separations at which the dipole moment changes rapidly.

Figure 4.3 illustrates the PA rate $K_{\mathrm{PA}}^{v}(B)$ for the ground state of ^{6}Li^{23}Na at $T = 50$ μK and the PA laser intensity $I = 1$ W/cm^2. Near a resonance, K_{PA}^{v} is enhanced by up to five orders of magnitude, even for low-lying rovibrational levels ($v < 10$). For typical gas densities ($n_{\mathrm{Li}} = n_{\mathrm{Na}} \sim 10^{12}$ cm^{-3}) and an illuminated volume V of 1 mm^3, up to $N_v = n_{\mathrm{Li}} n_{\mathrm{Na}} V K_{\mathrm{PA}}^{v} = 2 \times 10^6$ molecules can be formed in $v = 0$ at 1403 Gauss. Here, we neglected the stimulated relaxation by the PA laser which can reduce the rate by up to 50% [69]), as well as the saturation effects [116], resulting, nevertheless, in an equally impressive enhancement.

The enhanced formation rates can be easily understood if we take a closer look at the wavefunctions. There is a sharp increase in the amplitudes of the radial wavefunctions ψ_α in the vicinity of a Feshbach resonance. We illustrate this in Figure 4.4 in terms of the total probability density $|\Psi_{\epsilon,\ell=0}(R)|^2$ as a function of B. As the magnetic field approaches either of the resonances at 1081 and 1403 Gauss, the total probability density increases by several orders of magnitude. This enhancement is proportionally the same in all coupled channels.

Figure 4.5 shows the total initial probability density $|\Psi_{\epsilon,\ell=0}(R)|^2$ on- and off-resonance ($B = 1400$ and 1200 G, respectively). The main effect of the resonance is the appearance of a large peak at shorter distance near 40 a_0 (see top panel, inset). The peak is located approximately at the classical outer turning point R_{out} of the bound state associated to the closed channel, usually one of the uppermost

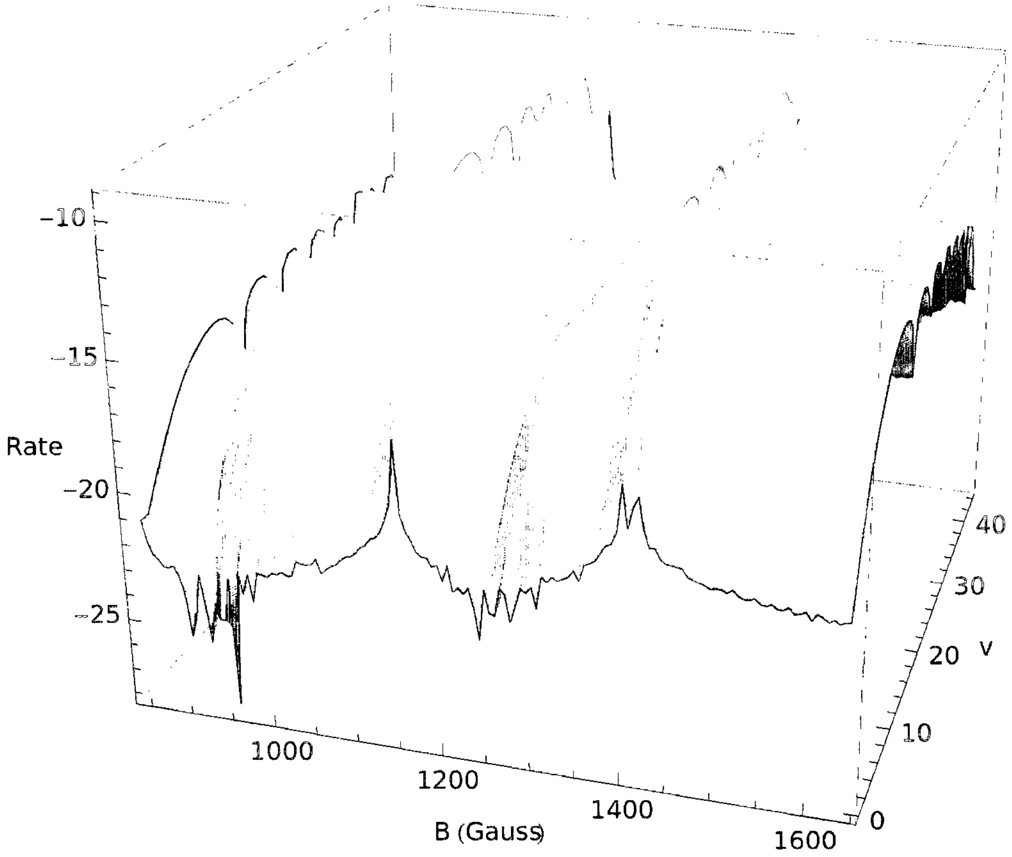

Fig. 4.3: Logarithm of the FOPA rate K_{PA}^{v} in $\mathrm{cm}^3\mathrm{s}^{-1}$ vs. magnetic field ($T = 50\ \mu\mathrm{K}$, $I = 1\ \mathrm{W/cm}^2$) for bound vibrational levels v of the LiNa $\mathrm{X}^1\Sigma^+$ potential. The atoms are initially in channel $|23\rangle$. Two Feshbach resonances at 1081 and 1403 Gauss enhance the PA rates by several orders of magnitude.

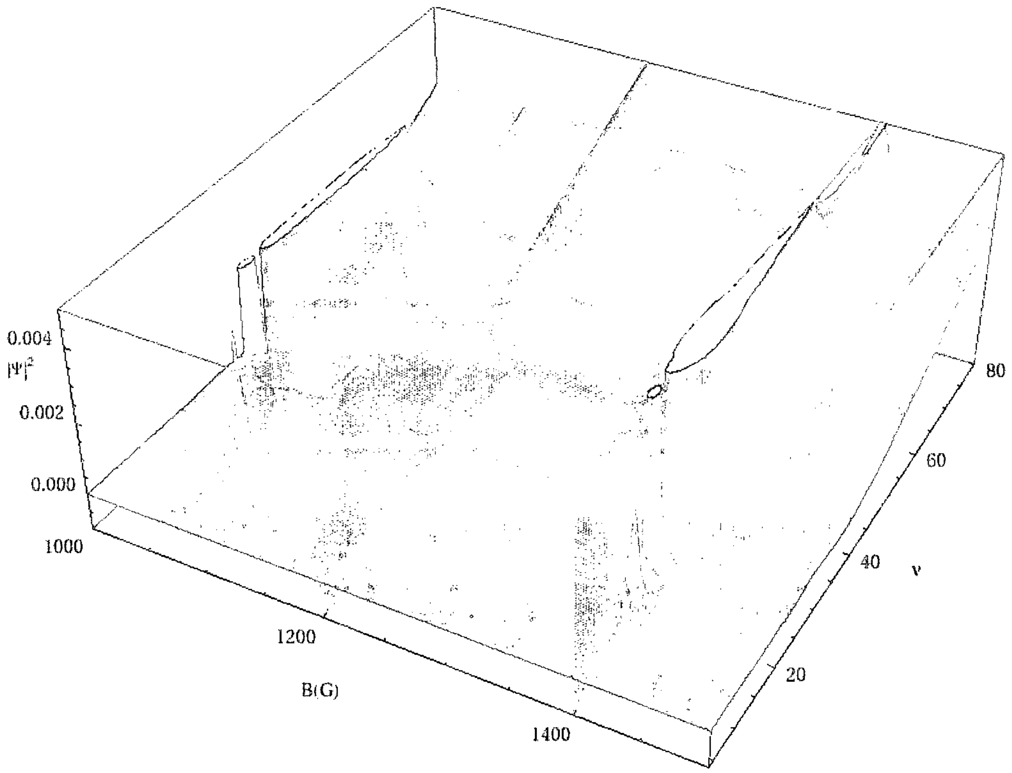

Fig. 4.4: Probability density $|\Psi_{\epsilon,\ell=0}(R)|^2$ vs. B. As B approaches a resonance, $|\Psi_{\epsilon,\ell=0}|^2$ increases sharply (truncated above 0.01). Examples of $|\Psi_{\epsilon,\ell=0}|^2$ off and on resonance (orthogonal planes at 1200 and 1400 Gauss, respectively) are shown in Figure 4.5.

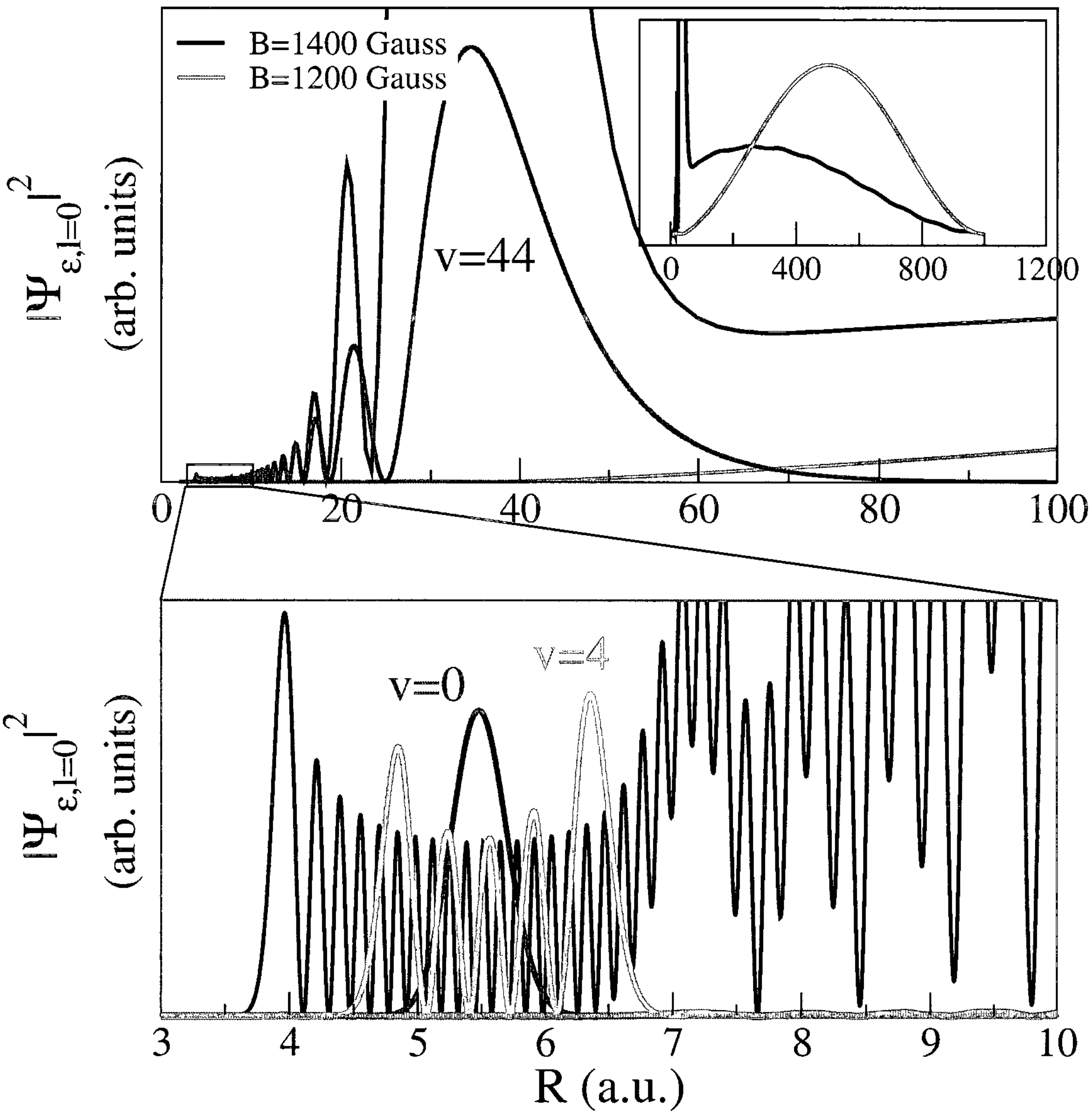

Fig. 4.5: Probability density on- (black) and off-resonance (red). The resonant probability density $|\Psi_{\epsilon,\ell=0}|^2$ has a maximum at $R \sim 35$ Bohr (top, inset). The upper bound level $v = 44$ of the singlet ground state is given for comparison. The bottom panel zooms in on the low-lying rovibrational levels v in the short range ($v = 0, 4$ are shown).

bound levels. This is apparent in the top panel, where this peak almost coincides with the outer lobe of $|\phi_{v=44,J=1}(R)|^2$, the uppermost bound level of $X^1\Sigma^+$. We also observe that the off-resonance probability density is greatly reduced when compared to the on-resonance one. This is a direct consequence of the reduced overlap of the wavefunctions for non-resonant magnetic fields which result in a destructive interference. The lower panel shows the small internuclear distances. Here, resonant probability density is significantly greater than for the off-resonant magnetic fields, leading to a substantial overlap integral in K^v_{PA} with deeply bound levels (*e.g.*, $v = 0$ or 4). We also note the more complicated nodal structure of $|\Psi_{\epsilon,\ell=0}(R)|^2$, a direct result of the hyperfine mixing of the entrance channel $|23\rangle$ with all other channels permitted by symmetry.

A generalization of Eq. (2.6.11) to several coupled channels is straightforward as we simply add their contributions. Furthermore, we found that only two or three channels contribute significantly to the enhanced formation rate coefficients. In Figure 4.6, we show K^v_{PA} for the ground vibrational level $v = 0$ with the same parameters as in Figure 4.3. The top panel depicts the scattering length a with the two Feshbach resonances and its analytical fit. The bottom panel compares the exact numerical results using eight coupled channels with the analytical expression (2.6.11). In both cases, the agreement is impressive. We verified that similar agreement was obtainable for other levels v, indicating the broad and general validity of Eq. (2.6.11).

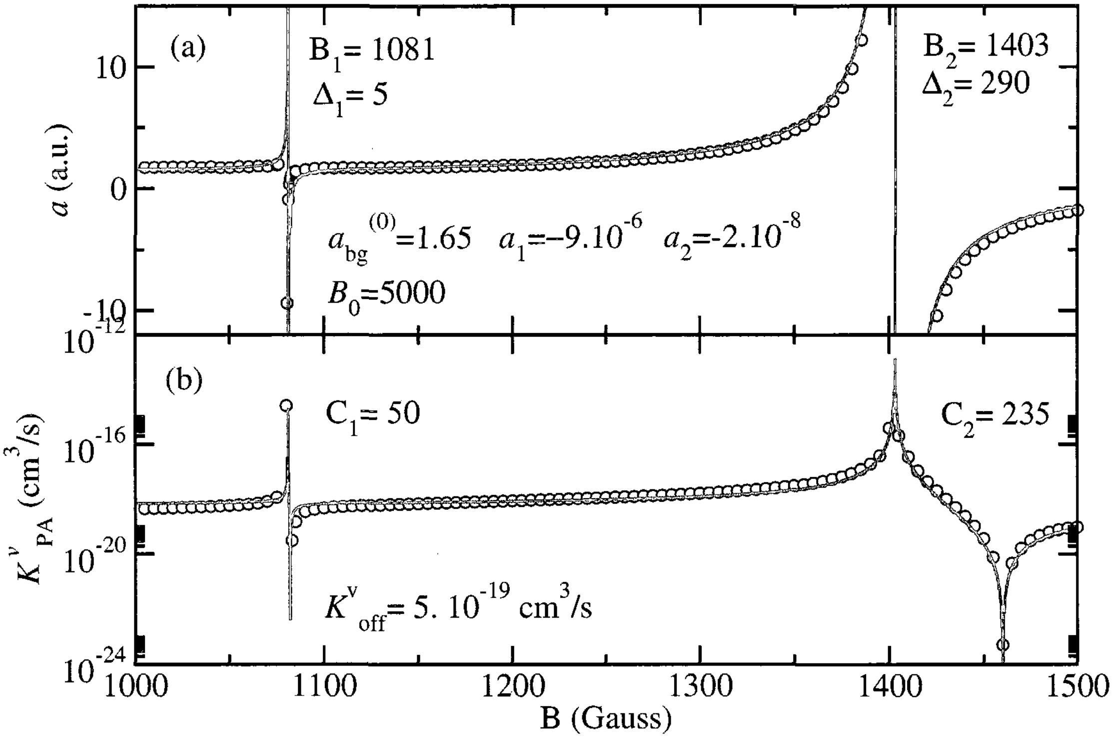

Fig. 4.6: Panel (a): scattering length a for the full coupled problem (circles) and the fit using $a = a_{\rm bg}(B)(1 - \frac{\Delta_1}{B-B_1} - \frac{\Delta_2}{B-B_2})$ with $a_{\rm bg}(B) = a_{\rm bg}^{(0)} + a_1(B + B_0) + a_2(B + B_0)^2$. Panel (b): $K^v_{\rm PA}$ for $v = 0$ at 50 μK and 1 W/cm^2 (circles) and the simple formula (2.6.11) using $\tan\delta = ka_{\rm bg}(B)(\frac{\Delta_1}{B-B_1} + \frac{\Delta_2}{B-B_2})$. Calculated numerical parameters for the fit are also shown.

4.3 Forming ultracold molecules using two-photon FOPA

The increase in photoassociation rate calculated in the previous section is not limited to the single-photon Feshbach-optimized photoassociation. A two-photon PA process can also benefit from the "Feshbach wavefunction." Increased amplitude of the initial Feshbach wavefunction at small internuclear separations can lead to larger Franck-Condon factors between the initial state and rovibrational levels in an excited state. As a result, a set of rovibrational levels inaccessible by the traditional photoassociation could be populated, leading to different possible applications [67].

For example, such an application could be creating stable ultracold molecules by two-photon photoassociation [117,11,13], where the Feshbach wavefunction is taken as the starting point. If a significant percent of the population can be transferred into an excited vibrational level which has a good Franck-Condon factor with $v = 0$, or with other low vibrational levels in the ground state, it will spontaneously decay and a part of the population will end up in the desired vibrational level. More control over the process can be achieved, while increasing the transferred amount, through stimulated emission from the excited state induced by the second PA laser. Such a two-photon FOPA scheme is illustrated in Figure 4.7.

Obtaining a significant increase of the molecule formation rates is not the only advantage of using the continuum "Feshbach wavefunction." The Feshbach wavefunction for a nearly-resonant magnetic field contains both singlet and triplet components mixed by the hyperfine interaction. Consequently, excited states of both singlet and triplet symmetries can be accessed. This is a significant advantage as it allows one to access the rovibrational levels that are otherwise forbidden due to symmetry. The traditional photassociation can overcome this problem by starting from either a singlet or a triplet bound state. The corresponding wavefunctions, however, have high amplitudes concentrated near classical turning points, which are, typically, far apart from each other and it is not always possible to find suitable vibrational levels. In such cases using FOPA could be a viable alternative.

4.3.1 2-photon FOPA rates for forming ultracold ^{6}Li^{87}Rb

To quantify the two-photon FOPA rates for higher excited states we consider photoassociation of a ^{6}Li^{87}Rb molecule starting from an ultracold Li+Rb mixture. In the previous chapter we have analyzed scattering properties of a Li+Rb pair in a magnetic field and located Feshbach resonances. We select the hyperfine channel $|11\rangle$ as the initial state for the PA. There are two s-wave Feshbach resonances at 1067 and 1278 Gauss, and two p-wave resonances at 883 and 1064 Gauss in that state. Moreover, channel $|11\rangle$ has the lowest energy in the magnetic field (see 3.1 in Chapter 3), resulting in only one open channel (itself) that is coupled to 7 closed channels with the same total projection of the magnetic quantum number m_f. This channel is particularly interesting since it has been produced in experiments

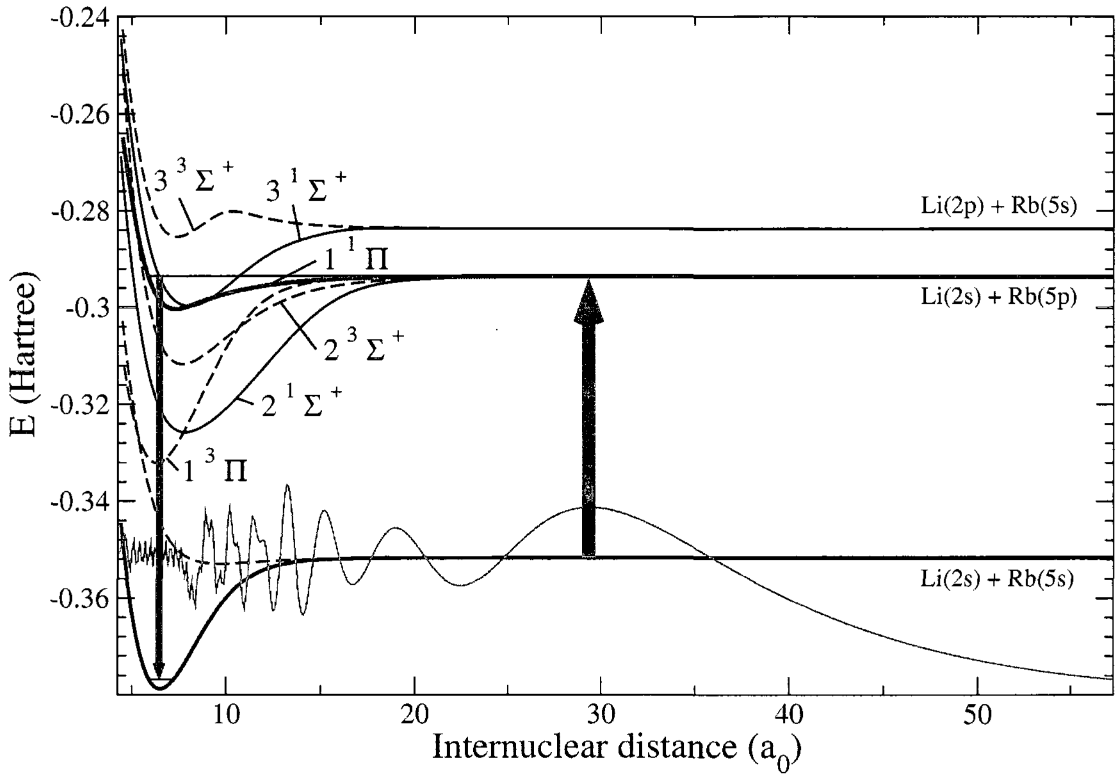

Fig. 4.7: Molecular potentials for the first three asymptotes in ^{6}Li^{87}Rb. Singlet and triplet Σ and Π states are shown. Two-photon stimulated photoassociation of the molecule through the $1\,^1\Pi$ state (blue curve) starting from the Feshbach wavefunction is indicated (green and red arrows represent PA lasers).

[74], while lack of other open channels simplifies the interpretation of the results.

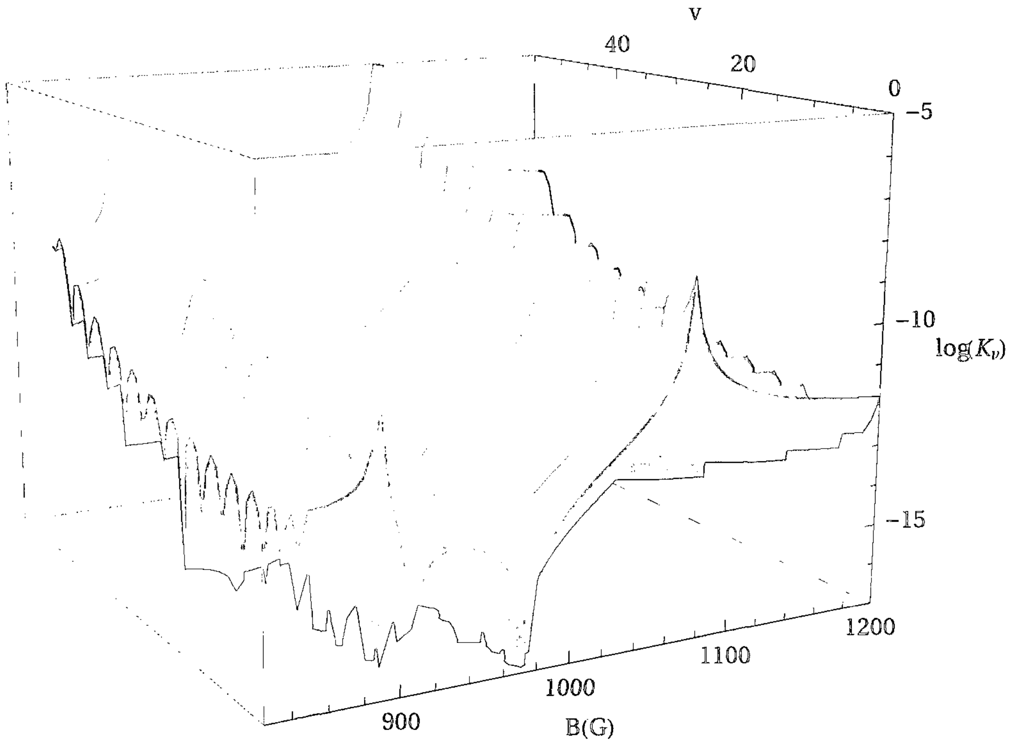

Fig. 4.8: FOPA rate for formation of the ^{6}Li^{87}Rb molecules in the 1 $^1\Pi$ state.

Ab-initio molecular potentials for excited states of ^{6}Li^{87}Rb molecule [98] (only Σ and Π states going to $S + P$ and $P + S$ asymptotes are shown), as well as a schematic representation of 2-photon FOPA, are presented in Figure 4.7. Classical turning points, where the amplitudes of the bound-state wavefunction is the highest, do not seem to be favorable for forming molecules in the ground rovibrational level for any of the singlet excited states. To overcome this, we use 2-photon stimulated FOPA, while relying on the fact that the "Feshbach wavefunction" (shown in red) has a significantly larger amplitude (fast oscillations visible in Figure 4.7) than bound-state wavefunctions for $R < 7\ a_0$.

The first step is to calculate the dependence on the magnetic field of the 1-photon FOPA formation rate K^v_{PA} for the 2 $^1\Sigma^+$ molecular potential. We expect the maximum increase in rate around the broader s-wave Feshbach resonance at 1067 G. For simplification, we consider a constant transition dipole moment $D(R)$, which we take to be equal to the atomic values. In addition, we assume the same PA laser intensity and gas densities as in the previous section. The obtained formation rate for the first 40 vibrational levels is illustrated in Figure 4.8. As before, when we considered transition from the Feshbach state into the ground state of LiNa (Figure 4.3), the rate K^v_{PA} was increased by several orders of magnitude near the resonances. The periodic increase and decrease of the rate as the v changes is easily explained by repeating constructive and destructive interference of the initial and target wavefunctions. The maximum enhancement is obtained for $B = 1067$ G, which is very close to the Feshbach resonance at $B = 1067.13$ G.

Next, we consider two excited potential curves for the intermediate step in the 2-photon process: 1 $^1\Pi$ (31 bound vibrational levels) and 2 $^1\Sigma^+$ (83 bound vibrational levels). Franck-Condon factors (FCFs) for the two 1-photon processes

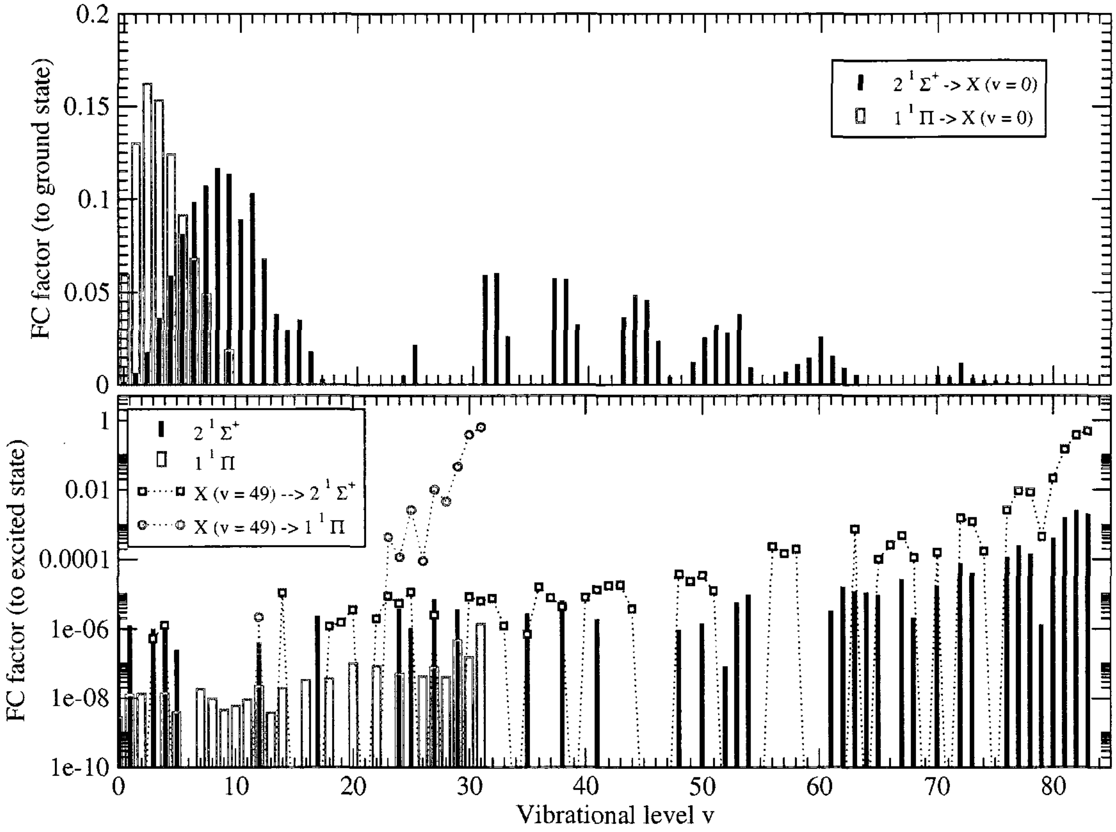

Fig. 4.9: Franck-Condon factors (FCF) for 2-photon FOPA in ^{6}Li^{87}Rb.

Bottom: FCFs between the Feshbach wavefunction at 1067 G and the $2\ ^1\Sigma^+$ (solid black bars), and $1\ ^1\Pi$ states (red bars). FCFs between the last bound level ($v = 49$) of $X\ ^1\Sigma^+$ and the excited states, $2\ ^1\Sigma^+$ (blue squares), and $1\ ^1\Pi$ (green circles) states, are given for comparison. *Top:* FCFs between vibrational levels of $2\ ^1\Sigma^+$ (solid black bars) and $1\ ^1\Pi$ (red bars) and $v = 0$ of $X\ ^1\Sigma^+$.

are shown in Figure 4.9. The bottom panel shows FCFs from the Feshbach state to the excited states (black and red bars), and the top panel shows the FCFs for the second step of the process, a bound-bound transition between the excited states and the ground state. From the top panel, we can see that the overlap with the $X\ ^1\Sigma^+(v=0)$ peaks at low vibrational levels, $v=2$ for the $1\ ^1\Pi$ and $v=8$ for the $2\ ^1\Sigma^+$ potential, indicating that the most efficient molecule formation in the $v=0$ of the ground state would require populating these states. In addition, the rate is higher for the $1\ ^1\Pi$ potential. However, populating these low vibrational levels in the first step is not very efficient, as it can be seen from the bottom panel of Figure 4.9. Namely, the FCFs between the near-resonant Feshbach wavefunction are rather small for low vibrational levels of both excited potentials, ranging from roughly 10^{-8} for accessing $v=1,2$ up to about 10^{-9} for $v=0$ of the $1\ ^1\Pi$ state. The enhancement is larger, about 10^{-6}, for $v=0,1$ for the $2\ ^1\Sigma^+$ potential. For comparison, we also show the FCFs for bound-bound transitions between the last bound vibrational level, $v=49$, in the ground state, and the two excited states (bottom panel, blue squares for the $2\ ^1\Sigma^+$ state, and green circles for the $1\ ^1\Pi$ state).

While none of these pathways seem to be particularly suitable for highly efficient formation of ultracold $^6\mathrm{Li}^{87}\mathrm{Rb}$ molecules in $v=0$ of their ground state, it is certainly possible to find more efficient 2-photon schemes in this or similar heteronuclear systems.

v'	$K^2_{v=0,v'}$ 10^{-18} cm^3/s
0	0.59437
1	5.35983
2	6.20424
4	6.70457
5	1.27794
7	1.04711
16	0.02041

Table 4.1: 2-photon FOPA formation rates for ^{6}Li^{87}Rb molecules in $v = 0$ of the ground state. Levels v' are vibrational levels of the intermediate $1\ ^1\Pi$ molecular state and the starting point is the open-channel Feshbach wavefunction calculated for $B = 1067$ G.

Finally, we evaluate the total formation rate for the most efficient pathways. The 2-photon stimulated PA rate can be calculated by considering a sequence of two single-photon processes. Instead of repeating the derivation here, we refer the reader to Refs. [110,117]. The final expression, assuming sufficiently large separation between the levels to avoid complications due to excitations of multiple vibrational levels [118], is:

$$K^{(2)}_{vv'}(T) = A(I_1, I_2, T)|\langle\phi_{v',J=1}|D'(R)|\Psi_{\epsilon,\ell=0}\rangle|^2|\langle\phi_{v,J=0}|D(R)|\phi_{v',J=1}\rangle|^2, \quad (4.3.1)$$

where

$$A(I_1, I_2, T) = \frac{64\pi^6}{h^4}\frac{I_1 I_2}{c^2}\frac{e^{-1/2}}{Q_T}\sqrt{\frac{k_B T}{2}}. \quad (4.3.2)$$

Here, I_1 and I_2 are the laser intensities. Using the Eq. (4.3.1) we have calculated two-photon FOPA formation rates for $v = 0$ in the ground state via the 1 $^1\Pi$ molecular state. We assumed laser intensities $I_1 = I_2 = 1000$ mW/cm^2 and temperature $T = 1\mu$K. The rates are tabulated in Table 4.3.1.

The 2-photon formation rates are smaller than the rates obtained in a direct single-photon FOPA process (see previous section, Figure 4.3). However, we believe that the 2-photon process is more convenient to realize experimentally. One reason for that are practical limitations imposed by laser wavelengths. Since photoassociation of ultracold molecules has been used extensively in spectroscopy, the existing equipment is well adapted for transitions to the excited states of alkali molecules. In that sense, the 2-photon FOPA process requires the same wavelength region as conventional PA spectroscopy. Another advantage is additional control over the process introduced by adding the second laser. In addition, a time-dependent FOPA scheme, where short laser pulses are used to transfer the population from the resonant Feshbach state into an excited state, also requires a 2-photon setup [119].

Chapter 5

Application of Feshbach-optimized photoassociation to precision measurements

In the previous chapter we have introduced Feshbach-optimized photoassociation, a new method that can be used in molecular spectroscopy, as well as for realizing more efficient approaches to formation of stable ultracold molecules. Here, we continue to build upon the results from the last two chapters as we suggest another possible application for FOPA in the domain of precision measurements. Specifically, we discuss the sensitivity of the PA formation rate K_v^{PA} to the ratio of electron-proton mass, $\beta = m_e/m_p$, a fundamental physical constant.

5.1 Motivation: variability of physical constants?

Quasar absorption spectra hint that the fine structure constant α may have changed over the history of the universe [120–122]. If proved true, the fact that one or several physical constants change in time would have a major impact on physical theories: the equivalence principle in general relativity would be violated and our understanding of cosmology would be profoundly transformed. Grand unification models and quantum chromodynamics (QCD) predict that quark and electron masses, as well as the strong interaction constant, depend on the fine structure constant [122]. Consequently, its variation could be used to distinguish among the existing models and advance our understanding of elementary particle physics.

Besides astrophysical observations, limits on the rate of change of fundamental constants have been established independently from the Oklo natural nuclear reactor [123] and from Big Bang Nucleosynthesis [122], as well as from precision measurement experiments with ultracold atoms and molecules [124]. These experiments so far do not contradict each other since they probe very different epochs. A good overview of present day limits on temporal and spatial variation, as well as a detailed overview of how they were established, can be found in Ref. [121].

5.2 Introduction

Recent developments in ultracold atomic and molecular physics offer new possibilities for precision measurement experiments. A particularly suitable quantity to consider is the variation of dimensionless electron-proton mass ratio $\delta\beta/\beta$ [125], with $\beta = m_e/m_p$. This can be understood by considering the fact that molecules are bound by the electronic interaction (making molecular potential electronic in origin), while the mass of the individual atoms is mostly baryonic. Both scattering and spectroscopic properties of cold molecules, such as scattering length or position of the last vibrational energy level, are very sensitive to β.

The strongest astrophysical constraint of the variability of β available today comes from the inverse rotational spectra of ammonia and HC_3N molecules observed toward a quasar background [126,127]. Several precision measurement experiments that focus on the variation of electron-proton mass ratio in ultracold atomic and molecular systems have been proposed recently [128,129]. Such experiments could give an estimate of the limit of possible time variation on the order of $\dot{\alpha}/\alpha \sim 10^{-15}$ independently of limits obtained by atomic clocks [124].

Chin and Flambaum [125] have studied the variation of β near a Feshbach resonance and concluded that it is possible to relate the variation of the scattering length $a(B)$ to the variation of the electron-proton mass ratio, $\delta\beta/\beta$. They have calculated the proportionality factor between the two, and suggested a precision measurement experiment that could determine variation of the electron-proton mass ratio by measuring the relative variation of the scattering length near a Feshbach resonance. Moreover, their result can be easily generalized from magnetic Feshbach resonances in diatomic molecules to any system in which Feshbach resonances of any type exist.

We propose a new approach to measure the time variation of β. Feshbach-optimized photoassociation, presented in the previous chapter, predicts a large enhancement of the formation rate K_v^{PA} of diatomic molecules photoassociated from an ultracold atomic pair near a Feshbach resonance (see also Ref. [130]). Recent experimental work shows that the same holds true in a BEC [131].

Our analysis shows that the PA formation rate K_v^{PA} for diatomic molecules near a Feshbach resonance can be related to the variation of β with an even larger enhancement factor than was obtained for the scattering length [125]. Contrary to our intuition, such enhancement can be achieved at the *minimum* of the PA rate, far from a resonance. This turns out to be advantageous because such measurements would not be affected by the singular behavior of the scattering length and different many-body effects possibly present near the resonance would be avoided. In addition, performing measurements of the rate at its minimum would not be limited by the unitarity limit which is easily reached near a resonance [116].

5.3 Model

We consider one-photon photoassociation of two ultracold ($T < 1$ mK, ℓ=0) atoms in their ground state into an excited state of a diatomic molecule [11]. At the temperature T, and assuming a Maxwell-Boltzmann distribution of relative velocities in the gas, the PA rate for molecules in the vibrational level v of an excited state K_v^{PA} is [132]

$$K_v^{PA} = \frac{k_B T}{h Q_T} \int_0^\infty |S_v(\epsilon, k)|^2 e^{-\epsilon/k_B T} \frac{d\epsilon}{k_B T}, \tag{5.3.1}$$

where $Q_T = (2\pi\mu k_B T/h^2)^{3/2}$ is the translational partition function, $\epsilon = (\hbar k)/2\mu$ is the asymptotic kinetic energy of the colliding atoms, μ is the reduced mass, $S_v(\epsilon, k)$ is the S-matrix element for the channel that forms a molecular bound state v, and k_B is the Boltzmann constant.

At ultracold temperatures, the S-matrix element can be expressed as [117]

$$|S_v(\epsilon, k)|^2 = \frac{\gamma_v \gamma_s(\epsilon)}{(\epsilon - \Delta)^2 + \frac{1}{4}(\gamma_s + \gamma_v)^2}, \tag{5.3.2}$$

with the detuning $\Delta = E_v - \hbar\omega$, where E_v is the energy of the bound molecular level v. Here, I is the PA laser intensity, γ_s is the stimulated decay rate, and γ_v is the width of the targeted vibrational level v. For low laser intensities the stimulated rate γ_s becomes [110]

$$\gamma_s(\epsilon) \simeq \frac{4\pi^2 I}{c} |\langle v|D(R)|\epsilon\rangle|^2, \tag{5.3.3}$$

where $D(R)$ is the transition dipole moment. Here, $|\epsilon\rangle$ and $|v\rangle$ are the energy-normalized initial state and a molecular rovibrational state, respectively.

Expression (5.3.1) can be further simplified if we assume that atoms have well defined energies, and that $\gamma_v + \gamma_s(\epsilon) \approx \gamma_s(\epsilon)$, which is the case for low intensities of the PA laser. The PA rate is the highest for detuning $\Delta = k_B T/2$ [117,110], and it takes the form:

$$K^v_{\mathrm{PA}} = \frac{8\pi^3}{h} \frac{I}{c} \frac{e^{-1/2}}{Q_T} |\langle \epsilon|D(R)|v\rangle|^2. \tag{5.3.4}$$

Introduction of an external magnetic field will break the degeneracy of molecular hyperfine states and introduce a small Zeeman shift proportional to the magnetic field. A Feshbach resonance occurs if the energy of a bound level is shifted to match the asymptotic energy of the colliding atoms. In the presence of a single Feshbach resonance the real part of the scattering length will depend on the magnetic field B as [13]

$$a = a_{\mathrm{bg}} \left(1 + \frac{\Delta B}{B_0 - B} \right), \tag{5.3.5}$$

where ΔB is the width of the resonance and B_0 is the resonant magnetic field.

In the previous chapter we used a coupled-channel theory to accurately model photoassociation of an atomic pair into a molecule in the presence of an external magnetic field. However, such a problem can only be solved numerically in a general case. We do not follow such an approach here. Instead, we use the analytic two-channel model developed in the previous chapter to describe the Feshbach-optimized photoassociation of an atomic pair (see Section 2.6.1 for details).

The next step is to express the dipole matrix element $d = \langle v | D(R) | \epsilon \rangle$ in terms of the analytic solution obtained in the two-channel model. The stimulated width γ_s depends on d, and after the analytic solution is substituted, it can be expressed as [116]

$$\gamma_s(I, k, B) = \gamma_s^{\mathrm{off}}(I, k) |1 + C_1 \tan\delta + C_2 \sin\delta|^2, \tag{5.3.6}$$

where γ_s^{off} is the off-resonant stimulated rate, $C_1(k, v)$ and $C_2(k, v)$ are dimensionless ratios of dipole matrix elements between the open and closed channel defined in Eq. (2.6.13), and $\delta(k)$ is the phase shift. We are mainly interested in behavior of the dipole matrix element as the magnetic field changes. The $\gamma_s^{\mathrm{off}}(I, k)$ has a role of a constant; it depends on the laser intensity and energy, both of which are constant external parameters.

To the first order in k, the s-wave phase shift is related to the scattering length a as

$$\tan(\delta + \delta_{\mathrm{bg}}) = -ka, \tag{5.3.7}$$

where $\delta_{\mathrm{bg}} = -ka_{\mathrm{bg}}$, and a_{bg} is the background scattering length.

It follows that the formation rate coefficient K^v_{PA} can be expressed as

$$K^v_{\mathrm{PA}} = K^v_{\mathrm{off}}|1 + C_1\frac{k(a - a_{\mathrm{bg}})}{k^2 a_{\mathrm{bg}} a + 1} \pm C_2\frac{k(a - a_{\mathrm{bg}})}{\sqrt{1 + k^2(a - a_{\mathrm{bg}})^2}}|^2 \tag{5.3.8}$$

In order to relate the variation of the PA formation rate K_{PA} to the variation of β we vary Eq. (5.3.8) with respect to the scattering length a and background scattering length a_{bg}. We then relate their relative variations to the variation of electron-proton mass β, following the procedure outlined in Ref. [125].

For a transition from the continuum at the wavenumber k to a vibrational level v in the excited state we obtain

$$\frac{\delta K^v_{\mathrm{PA}}}{K^v_{\mathrm{PA}}} = -\frac{2C_1 ka}{1 + C_1 k(a_{\mathrm{bg}} - a)}\frac{\delta a}{a} + \frac{2C_1 k a_{\mathrm{bg}}}{1 + C_1 k(a_{\mathrm{bg}} - a)}\frac{\delta a_{\mathrm{bg}}}{a_{\mathrm{bg}}}. \tag{5.3.9}$$

Let us examine this expression more closely. As the first step, we neglected second order terms in k and terms proportional to the C_2 coefficient. The k^2 at ultracold temperatures introduces a negligible correction [125]. The terms proportional to C_2 are much smaller than $\tan\delta$ (in Eq. (5.3.8)) close to a Feshbach resonance, which is our region of interest. Consequently, it is safe to neglect these terms.

We can also neglect the second term in Eq. (5.3.9). The background scattering length a_{bg} changes slowly compared to the derivative of the scattering length a with respect to magnetic field evaluated near a Feshbach resonance (see Eq. 5.3.5). This leaves us with the relation which connects relative variations of the photoassociation rate K^v_{PA} and scattering length a in the vicinity of a Feshbach resonance:

$$\frac{\delta K^v_{\text{PA}}}{K^v_{\text{PA}}} = -\frac{2C_1ka}{1 + C_1k(a_{\text{bg}} - a)}\frac{\delta a}{a}. \tag{5.3.10}$$

Chin and Flambaum [125] have analyzed variation of the scattering length in a two-channel model for ultracold atoms near a Feshbach resonance and derived the expression

$$\frac{\delta a}{a} = \frac{M}{2}\frac{(a - a_{\text{bg}})^2}{a_{\text{bg}}a}\frac{1}{\rho(E_m)\Delta E}\frac{\delta\beta}{\beta}, \tag{5.3.11}$$

where M is the vibrational quantum number of the closed channel bound state, $\rho(E_m) = 1/D$ is the density of states at the energy E_m that can be estimated from the energy level splittings D of the adjacent levels. Feshbach resonances are typically caused by the last bound level in the molecular potential. In turn, M is equal to the number of bound vibrational levels that the molecular potential can support.

From Eqs. (5.3.10) and (5.3.11), and assuming a sufficiently large number of vibrational levels [125], we obtain the proportionality factor between the relative variations of the PA rate for the rovibrational level v and electron-proton mass ratio β. To better illustrate this, we define the *enhancement factor* κ^v as

$$\frac{\delta K^v_{\text{PA}}}{K^v_{\text{PA}}} = \kappa^v \frac{\delta\beta}{\beta}, \tag{5.3.12}$$

where

$$\kappa^v = \frac{M}{2}\frac{(a-a_{\text{bg}})^2}{a_{\text{bg}}a}\frac{1}{\rho(E_m)\Delta E}\frac{2C_1ka}{C_1k(a-a_{\text{bg}})-1}. \tag{5.3.13}$$

Comparison to Eq. (5.3.11) shows that we have gained an extra term that depends on C_1k, in addition to dependence on a and a_{bg}. This extra term expresses dependence of κ^v on the combined hyperfine and Zeeman coupling between the initial open channel and one or more closed channels.

To further analyze the behavior of κ^v near a Feshbach resonance we assume that the scattering length depends on the magnetic field in a standard way, given in Eq. (5.3.5). Relation for κ^v now reads:

$$\kappa^v = -M\frac{a_{\text{bg}}C_1k}{(B-B_0)(B-B_0+a_{\text{bg}}C_1k\Delta B)}\frac{\Delta B}{\rho(E_m)} \tag{5.3.14}$$

Eq.(5.3.14) shows that κ^v will diverge not only at the resonance but also for $B = B_0 - a_{\text{bg}}C_1k\Delta B$, giving rise to a *second maximum* that coincides with the *minimum* of the PA formation rate reported in [131,67]. This is of major importance for future experimental realizations: near its minimum the PA rate is not affected by saturation effects which would limit the intensity and the scattering length remains finite [116].

Another important feature is the dependence of κ^v on the coefficient C_1k. Coefficient C_1 is given by the ratio of wavefunctions of the initial and final state.

The extensive study of Feshbach-optimized photoassociation conducted in the previous chapter has shown that the photoassociative formation rate, $K^v_{\rm PA}$, is strongly dependent on the choice of target vibrational level v. Consequently, it is important to find a suitable transition that would result in large formation rate while remaining easily accessible experimentally.

To illustrate and quantify these effects and estimate the maximum attainable limits by a precision measurement of $K^v_{\rm PA}$, we need to apply the procedure outlined in this section to several realistic systems.

5.4 Enhancement of time-variation of β in realistic ultracold mixtures

In chapter 3 we studied Feshbach-optimized photoassociation of diatomic alkali molecules, namely ^{6}Li-^{23}Na and ^{7}Li-^{23}Na, from ultracold mixtures of atomic Li and Na. For the same system, we successfully applied the two-channel analytic model to reproduce the formation rate of Feshbach-optimized photoassociation (see 4.6). Pellegrini and Côté [116] have used the same model to analyze saturation effects near Feshbach resonances in ultracold $\mathrm{Li_2}$. However, both $\mathrm{Li_2}$ and Li-Na molecules are light and support a smaller number of bound levels than heavier molecules. From Eq. (5.3.14) we can see that the enhancement factor κ_v depends on the number of bound vibrational levels M, favoring heavier molecules. Nevertheless, these systems can serve as a good starting point for the calculation since the model parameters for some PA pathways are known.

5.4.1 Test system: ^{7}Li$_2$ ultracold mixture

We consider one-photon photoassociation of the $^7\mathrm{Li}_2$ molecule to $v = 83$ of $1^3\Sigma_g^+$ state in the external magnetic field B. To the best of our knowledge this is the only ultracold mixture for which photoassociation in a magnetic field has been studied experimentally [131]. The lowest energy singlet and triplet molecular potentials for the $^7\mathrm{Li}_2$ molecule are taken from Ref. [133], and additional adjustments to reproduce the correct scattering properties of $^7\mathrm{Li}$ pair were applied [131,134]. The excited state from Ref. [135] is used in the calculation. We take the lowest energy Feshbach state $|\alpha = 1, \beta = 1\rangle = |f_1 = 1, m_{\mathrm{f}_1} = 1\rangle|f_2 = 1, m_{\mathrm{f}_2} = 1\rangle$ to be the starting point for the photoassociation process. In this particular channel there is a broad Feshbach resonance at 736 G that can be characterized well by Eq. (5.3.5) with parameters $B_0 = 736$ G, $\Delta B = 200$ G, and $a_{\mathrm{bg}} = -18$ a$_0$ [116]. As is the case with the other Feshbach states, $|12\rangle$ is a mixture of the energetically lowest singlet and triplet electronic states with a predominant triplet component. Moreover, a large Franck-Condon factor between this initial state and the vibrational level $v = 83$ in the targeted molecular state exists.

The model and resulting coupled equations are constructed in the same way as it was done in the previous chapter. $^7\mathrm{Li}_2$ is a bosonic homonuclear molecule (nuclear spin of $^7\mathrm{Li}_2$ is $I = 3/2$) and we need to perform the symmetrization according to Eq. 2.3.7. The close-coupling equations are solved using the mapped Fourier grid method [73], and we calculate the molecular formation rate K^{v}_{PA} according to Eq. (5.3.1). The dipole moment $D(R)$ for the transition into the $1^3\Sigma_g^+$ molecular state is taken from Ref. [135]. Dimensionless coefficients C_1 and C_2 are determined from a numerical fit of the calculated rate with the form given in Eq. (5.3.8). The other parameters are $T = 10$ μK, $I = 1.6$ W/cm^2 and $\gamma_v = 12$ MHz [135,116]. Finally, the enhancement factor $\kappa_{PA}^{v=83}$ for the $1^3\Sigma_g^+$ state is calculated according to Eq. (5.3.14).

The photoassociation rate calculated using the model with the listed parameters is compared to the full calculation in Figure 5.1. Near the Feshbach resonance the coupling between collisional channels is strongly enhanced and the laser intensity required to reach the unitarity limit becomes small [116]. Consequently, the photoassociation rate becomes strongly dependent on the laser intensity, as is shown in Figure 5.2. The minimum of the PA rate at about 709 G, however, remains unaffected, as it depends on the intensity according to the Wigner law [13].

The enhancement factor κ^v for the same system is shown in Figure 5.3. Two maxima at 709 G and 736 G correspond to magnetic fields for which the photoassociation rate diverges, at the maximum of destructive interference between wavefunctions of the initial and final state, corresponding to the second pole of Eq. (5.3.14), and at the resonance. Close to the resonance the scattering length

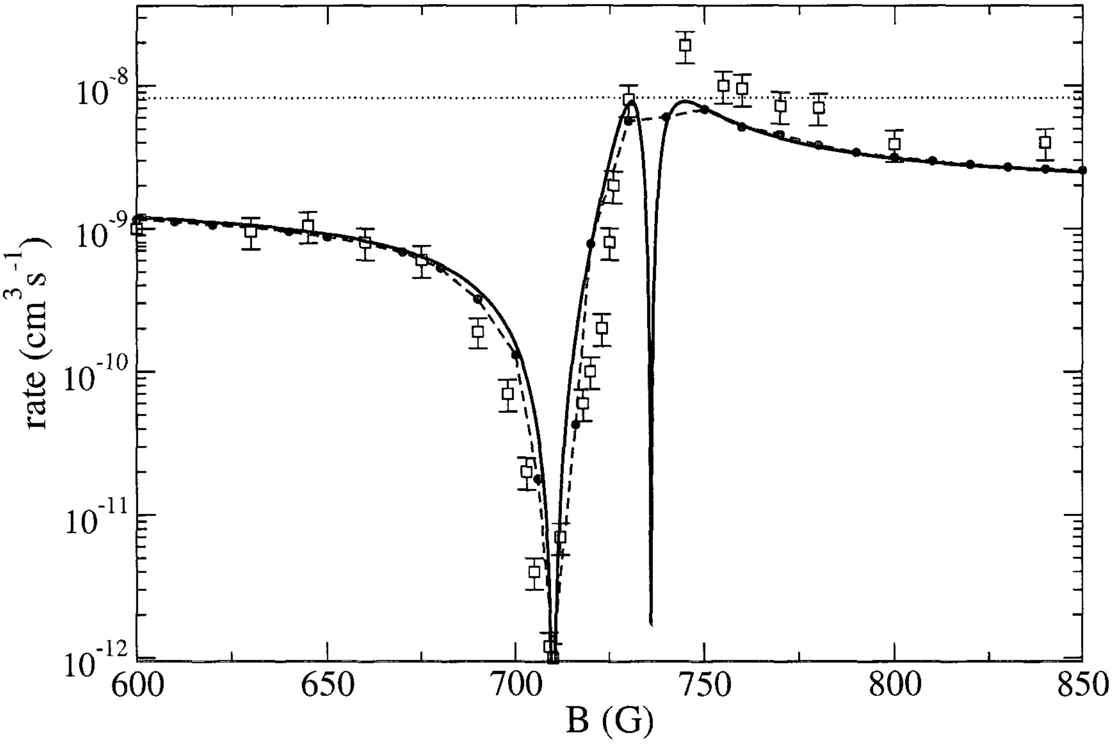

Fig. 5.1: Photoassociation rate K_{PA}^{v} for $^7Li_2$. Molecules are photoassociated into $v = 83$ of the $1^3\Sigma_g^+$ molecular state from the initial Feshbach $|f_1 = 1, m_{f_1} = 1\rangle|f_2 = 1, m_{f_2} = 0\rangle$ state. The dashed blue line corresponds to the numerical calculation, the solid black line is obtained using our two-channel model with $C_1 = 13$. The unitarity limit is indicated by the dotted line.

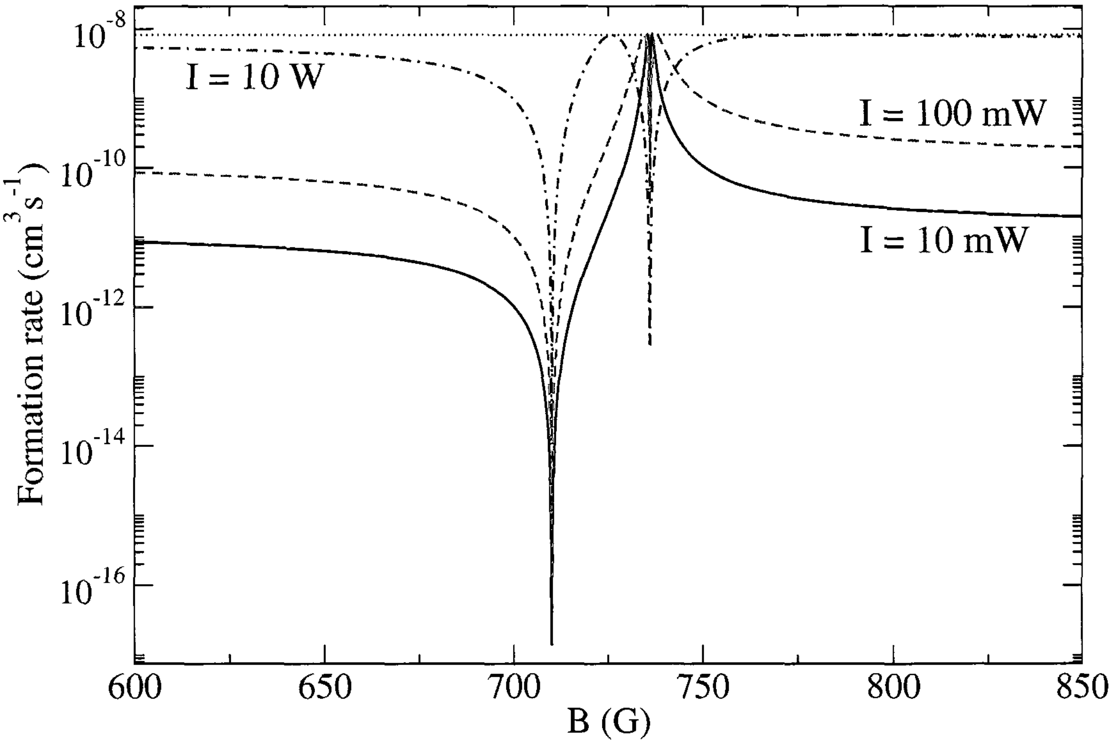

Fig. 5.2: Intensity dependence of the photoassociation rate in ^{7}Li$_2$ (same initial and final state as in Figure 5.1)

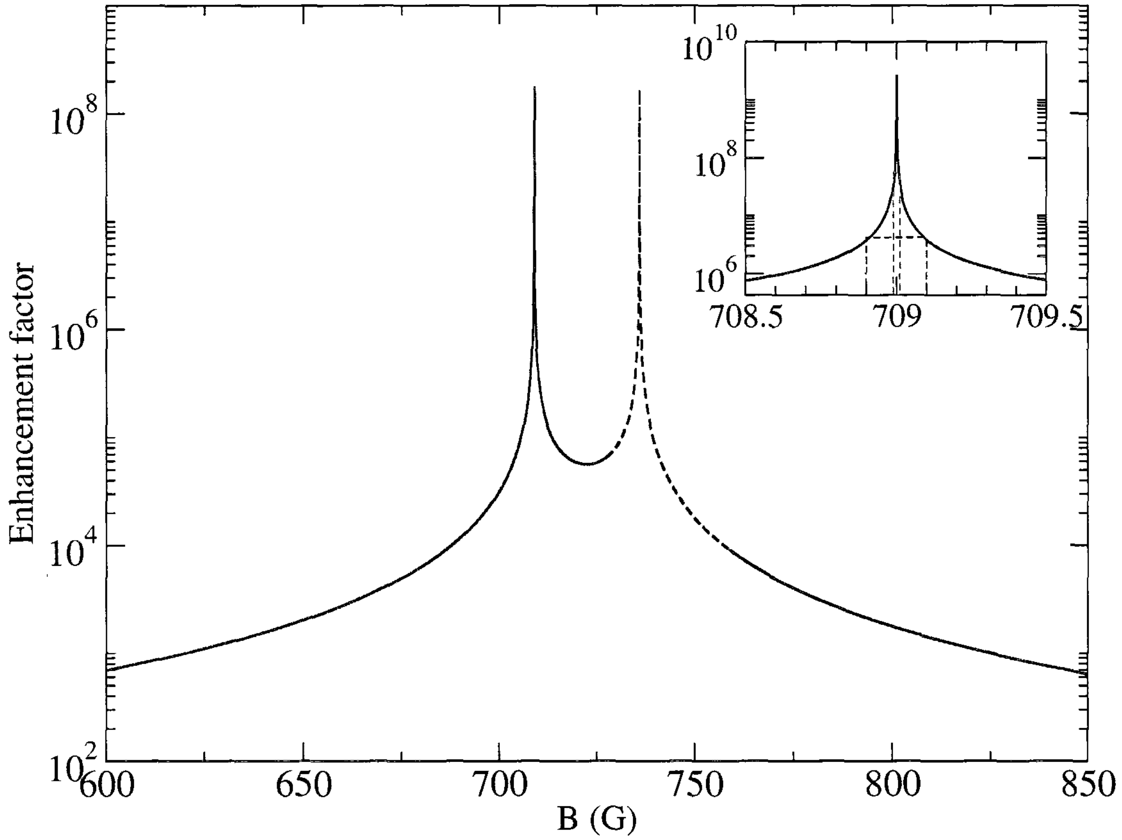

Fig. 5.3: Enhancement factor κ^v in $^7\mathrm{Li}_2$ (same initial and final states as above). The dashed line indicates the region that cannot be observed due to the saturation. *Inset:* Zoom in on the first peak. Sensitivities of 0.1 G and 0.01 G are indicated by dashed lines.

diverges and the system can no longer be treated as isolated and described by the two-channel model.

We proceed to analyze the first maximum at 709 G. Here, the attainable enhancement factor is not limited by the unitarity limit, but by the ability to form and detect a small number of molecules. To obtain the limit of variation $\delta\beta/\beta$, we assume that a typical density of ultracold gases in a trap is $n_{\mathrm{Li}} \approx 10^{12}$ cm^{-3}, the laser intensity of $I = 1$ W/cm^2 and an illuminated volume of $V = 1$ mm^3. At $B = 709.09$ G we predict the PA rate of $K^{v}_{\mathrm{PA}} = 9.4 \times 10^{-18}$ and the enhancement $\kappa^{v} \approx 2 \times 10^{8}$. If a measurement accuracy of 1% could be achieved while keeping the magnetic field stable to about 0.01 G at 709 G, detecting about 100 molecules out of 10^4 formed molecules would be sufficient to limit the maximum possible time variation of β to less than 5×10^{-11}. By using a higher laser intensity, the number of formed molecules could be increased (simplifying the detection), although better control of the magnetic field would be needed to further increase the sensitivity.

5.4.2 Enhancement factor for a narrow resonance in ^{6}Li-^{23}Na

According to Eq. (5.3.14), a better test of the time-variation of β could be performed by considering a narrow resonance in a heavier molecule. The Feshbach state $|\alpha = 1 \beta = 1\rangle$ in ^{6}Li-^{23}Na ultracold mixture [77], possesses a narrow Feshbach resonance for $B = 746.0$ G. We can parametrize it using the width $\Delta B = 0.044$

G and background scattering length $a_{\mathrm{bg}} = 14\ a_0$.

We can use this resonance to perform a calculation of the enhancement factor for a hypothetical Feshbach-optimized PA scheme to form ^{6}Li^{23}Na molecules in $v = 59$ of the $1^3\Sigma_g^+$ molecular state. In addition, if the laser intensity of $I = 10$ W cm^{-2} at wavelength $\lambda = 660$ nm is used for photoassociation, we can model the molecular formation rate using the two-channel model with parameters: $C_1 = -480$ and $K_{\mathrm{off}}^v = 4 \times 10^{-11}$. The number of bound vibrational levels in the closed channel in ^{6}Li^{23}Na is $M = 45$ [125]. According to the model, the minimum of the formation rates occurs for $B = 754.894$ G, resulting in the formation rate of about 1.8×10^5 molecules per second. Note the small separation between the maximum and minimum. Here, we assumed the same gas density and illuminated volume as for Li_2 molecules described in the previous section. If the stability of the magnetic field up to 1 mG could be realized, the maximum enhancement factor would be $\kappa \approx 1 \times 10^9$. Under assumption that the change in the formation rate of 10 molecules per second could be detected, the limit on the variation of β would be set to about 1 in 10^{-13}.

5.4.3 Enhancement factor for different systems

An even higher precision can be obtained if a heavier molecule such as Yb_2 or $^{133}Cs_2$ is photoassociated in the vicinity of a narrow Feshbach resonance. For example, an optical Feshbach resonance with externally controlled coupling strength

[136] or a g-wave magnetic Feshbach resonance in ^{133}Cs [137], are both very narrow, which would maximize the enhancement factor κ^v even before the channel-coupling term (the last term in Eq. (5.3.13)) is accounted for. Assuming the width of $\Delta B = 5$ mG [137], and the detection efficiency of molecules of 0.1 % at the minimum of the formation rate, a test of β on the 10^{-15} level could be performed. Such accuracy is comparable to the best available measurements of the variability of β.

These parameters are not unrealistic. Astability of 1 mG has been achieved near a narrow Feshbach resonance [138]. In fact, more optimistic values were assumed by other groups, who were optimistic about achieving astability of magnetic field on the level of 0.01 mG with adequate magnetic shielding [125,124].

In conclusion, based on the extreme sensitivity of variation of the molecular formation rate in an ultracold gas near a Feshbach resonance, we suggested a novel method for testing temporal variability of $\beta = m_e/m_p$. We show that it would be advantageous to perform such a precision measurement at the minimum of the PA rate, where the scattering length remains finite and the saturation effects are avoided.

Chapter 6

Theory of ion-atom charge-exchange collisions

In this chapter we briefly review a formalism that can be used to model CX collisions of fully stripped (completely ionized) ions with hydrogen atoms. The emphasis is placed on constructing molecular potentials for an equivalent ionic molecule. Such potentials describe the electronic interaction in a time-independent (molecular) picture which we used to treat the collisions of neutral atoms in the previous chapters. A more complete overview of existing semi-classical and quantum treatments of charge-exchange collisions can be found in Refs. [139–141].

6.1 Charge-exchange collisions of fully stripped ions with hydrogen

A charge-exchange collision between an ion and a hydrogen atom can be illustrated as

$$A^{q+} + H \rightarrow A^{*(q-1)+}(nl) + p^{+} \rightarrow A^{(q-1)+}(1s) + p^{+} + \gamma_1 + \gamma_2 + \ldots, \qquad (6.1.1)$$

where the relaxation after the electron capture results in emission of one or more photons (designated as γ_i). We discuss a case where the ion charge q is such that the ion is initially completely stripped of electrons.

A number of interesting astrophysical processes, such as chemical reactions in the early universe and charge-exchange collisions in astrophysical plasma, belong in this category [142]. We are particularly interested in investigating charge-exchange collisions between solar wind ions and heliospheric hydrogen and the properties of radiation emitted during their collisions.

As shown in the schematics, after the electron capture has occurred, the ion relaxes rapidly into its ground state, through either a series of de-excitations known as radiative cascade, or by a direct relaxation into the ground state. The emission spectra are determined by the initial excited state in which the electron was captured, as well as by the exact cascade pathway, while the population of the initial state depends on the relative energy at which the collision occurred. The average velocity of solar wind ions is about 400 km/s for the slow solar wind and about 750 km/s for the fast solar wind. This belongs in the regime of so-called slow collisions, where the relative velocity of hte colliding particles remains well below the Bohr velocity. While a semi-classical approach may work for slow collisions in some cases, the most accurate description of the process is usually obtained in a fully quantum coupled-channel model. Analogously to atom-atom collisions (see chapter 2), CX collisions can also be described in a time-independent molecular formalism.

6.2 Impact-parameter multistate molecular approximation

One way to model the charge-exchange problem is by invoking the straight-line impact parameter approximation [143,144]. To explain the idea behind this approach we first need to define the geometry for the problem. At collisional energies of interest, ranging between 0.1 keV and 10 keV, differential cross sections of elastic and inelastic collisions peak around the projectile direction of impact (forward-direction). In that regime, the particle trajectories can be described well by straight lines. Let us call the two nuclei, the proton and the incident ion, A and B, and $\vec{R}$ the position vector of B defined with respect to A. Let the position vector of the electron with respect to A be $\vec{r}_A$, and $\vec{r}_B$ with respect to B. The impact parameter approximation states that

$$\vec{R} = \vec{\rho} + \vec{v}t, \tag{6.2.1}$$

where $\vec{v}$ is the velocity of the incident particle and $\vec{\rho}$ is the component of $\vec{R}$ perpendicular to $\vec{v}$. Eq. (6.2.1) is, in fact, a defining equation for time t in terms of the velocity and internuclear distance.

For each value of $\vec{\rho}$ we need to solve the equation of motion

$$\left[H_{\mathrm{el}} - i\left(\frac{d}{dt}\right)_{\vec{r}_A}\right]\Psi(\vec{r}_A, t) = 0. \tag{6.2.2}$$

The operator $\left(\frac{d}{dt}\right)_{\vec{r}_A}$ indicates that the variables $(\vec{r}_A, t)$ are taken to be independent and used to express all other physical values.

In the molecular approximation, the total wavefunction Ψ can be expanded in terms of functions χ_v as

$$\Psi(\vec{r}_A, \vec{R}(t), t) = \sum_v a_v(t)\chi_v(r_A, R(t))e^{-is_v(t)} \tag{6.2.3}$$

with

$$s_v(t) = \int_{-\infty}^{t} \epsilon_v\left(|\vec{\rho} + \vec{v}t'|\right) dt', \tag{6.2.4}$$

where R is the magnitude of the vector $\vec{R}$.

The functions $\chi_v(r_A, R)$ are the eigenfunctions of the electronic part of the Hamiltonian

$$\left[H_{\text{el}} - \epsilon_v(R)\right]\chi_v(R) = 0. \tag{6.2.5}$$

Putting everything together, Eq. (6.2.3) leads to the system of coupled-channel equations

$$\frac{d}{dt}a_v(t) = -\sum_{v'} a_{v'}(t)\langle\chi_v|\left(\frac{d}{dt}\right)_{\vec{r}_A}|\chi_{v'}\rangle e^{-i[s_{v'}(t)-s_v(t)]}. \tag{6.2.6}$$

The appropriate initial condition on Ψ is

$$\Psi(r_A, t) = \lim_{t\to-\infty} \phi_0^{(A)}(r_A)e^{-i\alpha_0 t}, \tag{6.2.7}$$

where $\phi_0^{(A)}$ and α_0 are the atomic eigenfunction and eigenenergy. For our choice of the reactants, they correspond to the eigenvalues of the ground state of the hydrogen atom.

To evaluate the matrix element in Eq. (6.2.6), we need to solve the stationary Schrödinger equation for the problem, given in Eq. (6.2.5). The three-body

Schrödinger equation is separable in prolate spheroidal coordinates and it has an exact analytical solution which can be, in principle, evaluated up to the arbitrary precision. In literature, this particular equation has been thoroughly studied under the name of the two-center (or two-Coulomb-center) Schrödinger equation.

Before we proceed to discuss the two-center problem in more detail in the next section, we still need to show the way in which the charge-exchange cross section and the transition amplitude can be expressed from the defined quantities. Assuming that the electronic wavefunctions are known, we can integrate the coupled equations given by Eq. (6.2.6). The basis set is first truncated according to the charge-transfer process that we want to describe, and the coupled equations are integrated numerically using standard methods. For example, when truncating the basis set, keeping as few as three coupled molecular states is often sufficient to obtain a good agreement with experimental results [143,144].

The electron transition amplitude is extracted from the quantity $a_v(t)$ in the following way. By integrating Eq. (6.2.2) for $t \rightarrow \infty$, we obtain the total wavefunction for the electron bound to the particle A:

$$\Phi^A_{nl}(r_A, t) = \phi^A_{nl} e^{-i\alpha^A_{nl} t}. \tag{6.2.8}$$

Similarly, if the electron is bound to the particle B, we have

$$\Phi^B_{nl}(r_A, t) = \phi^B_{nl}(\vec{r_B}) e^{i\vec{v}\cdot\vec{r_A} - i\alpha^B_{nl} t} - \frac{i}{2} v^2 t, \tag{6.2.9}$$

where ϕ^A_{nl}, α^A_{nl}, ϕ^B_{nl}, and α^B_{nl} are the wavefunctions and energies of the atomic states (nl). Note that the wavefunction $\Phi^B_{nl}(r_A, t)$ is expressed in the coordinates centered on the *particle* A and the last term in Eq. (6.2.9) is simply the distance between the particles.

The transition amplitude between the total electronic wavefunction Psi and the electronic wavefunction of the particle A or B can be defined as

$$b^{A,B}_{nl}(\rho) = \lim_{t\to\infty} \langle \Phi^{A,B}_{nl}(r_A, t) | \Psi(\vec{r_A}, t) \rangle. \tag{6.2.10}$$

When the limiting behavior is carefully accounted for, it can be shown that the total charge-exchange probability within the impact-parameter molecular approximation becomes [143]

$$|b^B_T(\rho)|^2 = \sum_v |a^B_v(+\infty)^2 = 1 - \sum_{v'} |a^A_{v'}(+\infty)^2. \tag{6.2.11}$$

Finally, the total cross section for the charge-exchange is obtained by integrating over all incident paths

$$Q = 2\pi \int_0^\infty \rho d\rho |b^B_T(\rho)|^2. \tag{6.2.12}$$

Note that within the impact-parameter approximation the existence of momentum transfer is fully accounted for and the only approximation that remains is the truncation of the basis set.

6.3 Two-center Schrödinger equation

Let us examine more closely the two-center problem introduced in Eq. (6.2.5). The two-center Schrödinger equation for the $Z_A e Z_B$ system in the adiabatic ap-

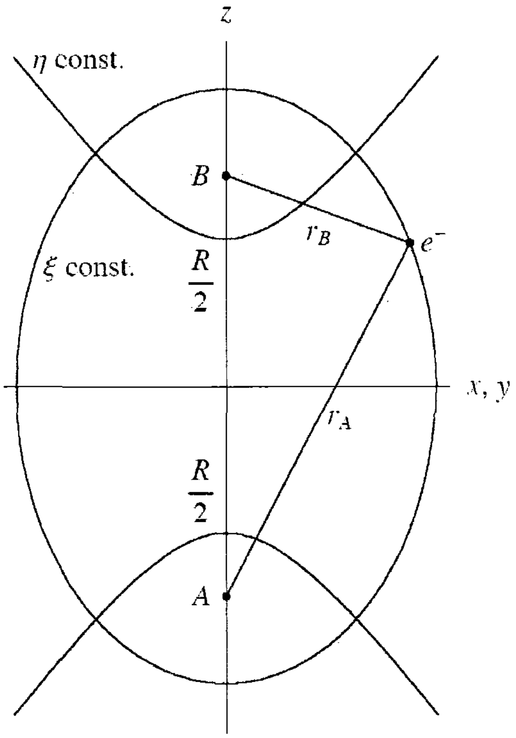

Fig. 6.1: Geometry of the two center problem.

proximation can be written as

$$\left(\frac{1}{2}\nabla^2 + \frac{Z_A}{r_A} + \frac{Z_B}{r_B} + E\right)\Psi = 0, \tag{6.3.1}$$

where r_A and r_B are the distances from the electron to the centers a and b, respectively, and E is the electron eigenenergy.

Eq. (6.3.1) is separable in prolate spheroidal coordinates [145]:

$$\begin{aligned} \xi &= \frac{r_A + r_B}{R}, \qquad (1 \leqslant \xi < \infty) \\ \eta &= \frac{r_A - r_B}{R}, \qquad (-1 \leqslant \xi \leqslant 1) \\ \varphi &= \arctan\left(\frac{y}{x}\right), \qquad (0 \leqslant \varphi < 2\pi) \end{aligned} \tag{6.3.2}$$

where R is the distance between the two Coulomb centers. Variables ξ and η are referred to as the radial and angular spheroidal variable, since, in the limit $R \longrightarrow 0$, they reduce to spherical polar coordinates. The product form of the wavefunction can be written as

$$\Psi = F(\varphi)G(\xi)H(\eta). \tag{6.3.3}$$

After the change to prolate spheroidal coordinates, Eq. (6.3.1) can be separated into a quasi-radial (in variable ξ) and a quasi-angular (variable η) equation

$$\begin{aligned} \frac{d}{d\xi}\left[(\xi^2-1)\frac{dG}{d\xi}\right] + \left(-\lambda + \alpha q\xi - q^2\xi^2 - \frac{m^2}{\xi^2-1}\right)G(\xi) &= 0, \\ \frac{d}{d\eta}\left[(1-\eta^2)\frac{dH}{d\eta}\right] + \left(\lambda - \beta q\eta + q^2\eta^2 - \frac{m^2}{1-\eta^2}\right)H(\eta) &= 0, \end{aligned} \tag{6.3.4}$$

and into a trivially solvable azimuthal equation

$$\frac{d^2F}{d\varphi^2} + m^2F(\varphi) = 0. \tag{6.3.5}$$

We have introduced the separation constants λ and m, and variables

$$q = R\sqrt{-\frac{E}{2}}, \qquad \alpha = \frac{(Z_A+Z_B)R}{q}, \qquad \beta = \frac{(Z_A+Z_B)R}{q}. \tag{6.3.6}$$

From the solution of Eq. (6.3.5)

$$F(\varphi) = \frac{1}{\sqrt{2\pi}}e^{im\varphi}, \tag{6.3.7}$$

and single-valuedness requirement, we have $m = 0, \pm1, \pm2, \ldots$. In this problem, the constant m plays the role of the magnetic quantum number.

Eqs. (6.3.4) are examples of the generalized spheroidal equation [146,147]. Special cases of the generalized spheroidal equation include the ordinary spheroidal equation (for $\alpha = 0$ or $\beta = 0$) and the Legendre differential equation ($\alpha = 0$ or $\beta = 0$ and $q = 0$). The generalized spheroidal equation also arises in general relativity [148] and within the theory of EM emitters [149].

6.3.1 Analytical solution

The solution of the quasi-angular part $H(\eta)$ of Eq.(6.3.4) can be found by factoring out the exponential part $e^{-q\eta}$ and expanding the remaining product into a series of associated Legendre polynomials:

$$H(\eta) = e^{-q\eta} \sum_{j=0}^{\infty} a_j P_{j+m}^{m}(\eta). \tag{6.3.8}$$

The real-valued coefficients a_j satisfy the three-term recurrence relation [150,147]

$$A_j a_{j+1} + (B_j - \lambda) a_j + C_j a_{j-1} = 0, \tag{6.3.9}$$

where

$$\begin{aligned} A_j &= \frac{q(2m+j+1)(2m+\beta+2j+2)}{2m+2j+3}, \\ B_j &= (m+j)(m+j+1) - q^2, \\ C_j &= \frac{qk(\beta - 2m - 2j)}{2m+2j-1}. \end{aligned} \tag{6.3.10}$$

From the requirement that the series is finite, $a_j \to 0$ as $j \to \infty$, it follows that the eigenvalues λ_{n_η} are the only allowed values of the separation constant λ. The corresponding eigenfunctions are $H_{n_\eta}(\eta)$. In addition, Sturm-Liouville theory states that the eigenvalues can only be real and that we can find the strictly increasing sequence of eigenvalues, which we denote η_0, η_1, $\eta_2, \ldots$.

From the normalization on the interval where η is defined,

$$\int_{-1}^{1} H_{n_\eta}(\eta)^2 d\eta = 1, \tag{6.3.11}$$

the following relation for the coefficients can be derived

$$\sum_{j=0}^{\infty} \frac{2(2m+j)!}{j!(2m+2j+1)} a_j^2 = 1. \tag{6.3.12}$$

A closed-form solution for the eigenvalues and eigenfunctions exists only when $Z_A = Z_B$ [147].

The quasi-radial equation can be expanded in a similar way in terms of Laguerre polynomials [151]. However, the computationally most efficient form is Jaffé expansion [152]

$$G(\xi) = e^{-q\xi}(\xi^2-1)^{\frac{m}{2}}(\xi+1)^{\frac{\alpha}{2}-m-1}\sum_{j=0}^{\infty} b_j x^j, \tag{6.3.13}$$

where $x = (\xi-1)(\xi+1)$.

The quasi-angular and quasi-radial wavefunctions have to be square integrable over all space. This implies that the solutions to the angular and radial equations cannot diverge at the poles $\eta = \pm 1$, $\xi = 1$, respectively. This gives us a range of values that the eigenenergy λ can take. Moreover, λ must have the same value in both the angular and radial equations, which in turn sets the energy E of the molecule.

Furthermore, we can define the operator Λ as [153]

$$\Lambda^2 = l^2 + \frac{1}{4}R^2 p_z^2 + Rz\left(\frac{Z_A}{r_A} - \frac{Z_B}{r_B}\right) \tag{6.3.14}$$

where l is the orbital angular momentum operator and p_z is the momentum. Operator Λ in the two-center problem has a function of the generalized orbital angular momentum. As $R \to 0$, we get $\Lambda^2 \to l^2$, as expected.

The natural choice of quantum numbers for the two-center systems are the nodal quantum numbers N_ξ and N_η, which are equal to the number of nodes in the quasi-radial and quasi-angular wavefunction. It follows that the molecular state can be defined in terms of (N_ξ, N_η, m) quantum numbers. The connection between the nodal and familiar atomic quantum numbers (n, l, m) can be established by analyzing their behavior in the united atom limit, $R \to 0$. The relation between the two sets is [154]

$$N_\xi = n - l - 1, \qquad N_\eta = l - m. \tag{6.3.15}$$

The states are designated in standard spectroscopic notation (using $s, p, d, f, \ldots$ for values of l, and $\sigma, \pi, \delta, \mu, \ldots$ for m; note that the *gerade* and *ungerade* (g and u) symmetry is meaningful for the homonuclear case only).

6.3.2 Asymptotic expansion

Construction of asymptotic formulae for the $(Z_A e Z_B)$ problem has been explored by several authors. While the earlier works focused solely on the H_2^+ ion, Ponomarev and Pusynina [155] carried out several calculations for a more general $(Z_A e Z_B)$ system. In addition, they identified the cases for which quasi-crossings of the potential energy curves occur. In a series of articles that followed, Komarov and Slavyanov with coworkers constructed asymptotic expansions for the electronic terms of the system in limits of small and large internuclear separation. They also found an analytical formula to compute the internuclear separation at which quasi-crossings occur. Their work is summarized in Ref. [156].

The asymptotic expression for the electronic energies at large internuclear separation is [156]

$$\begin{aligned}E_{N_\xi N_\eta m} &= -\frac{Z_A^2}{2n^2} - \frac{Z_B}{R} + \frac{Z_B}{2R^2 Z_A} n\Delta - \frac{Z_B n^2}{2R^3 Z_A^2}(6\Delta^2 - n^2 + 1) \\ &\quad + \frac{Z_B n^3}{16 Z_A^4 R^4}[Z_A \Delta(109\Delta^2 - 39n^2 - 9m^2 + 59) \\ &\quad - Z_B n(17n^2 - 3\Delta^2 - 9m^2 + 19)] + O(R^{-5}), \qquad (6.3.16)\end{aligned}$$

where $n = N_\xi + N_\eta + m$ is the principal quantum number and $\Delta = N_\xi - N_\eta$.

We calculated the electronic energies in the limit of large R using Eq. (6.3.16) and compared them to the numerically evaluated exact energy terms for several molecular ions. The results are given in Table 6.1. The asymptotic formula is particularly accurate in case of H_2^+ ion, for which the error becomes of the order of 10^{-4} a.u. at $R = 10$. Moreover, the formula yields much better agreement with the exact calculation for homonuclear ions. For the OH^{8+} and other heavier heteronuclear ions the convergence seems to be much slower, resulting in relatively good agreement at distances of $R = 100$ a.u. or larger.

A similar asymptotic expansion in a series of $\log R$ and powers of R has been constructed for small separations [156,157]. In addition, an expression for the

$R(a_0)$	$OH^{8+}(000)$	$OH^{8+}(500)$	$OH^{8+}(520)$	$He_2^{2+}(000))$	$H_2^+(000)$
5	1.40001	0.586092	1.97152	0.399485	0.0208203
10	0.7	0.502193	0.562412	0.200055	0.000353729
15	0.466667	0.372562	0.387422	0.133344	4.49405×10^{-6}
20	0.35	0.2946	0.302756	0.100004	1.96831×10^{-7}
35	0.2	0.180647	0.184209	0.0571432	4.97495×10^{-9}
50	0.14	0.130235	0.132305	0.0400001	5.51777×10^{-10}
100	0.07	0.0674702	0.0681087	0.02	8.04878×10^{-12}
200	0.035	0.0343558	0.0345332	0.01	1.21125×10^{-13}
500	0.014	0.0138958	0.013926	0.004	4.88498×10^{-15}

Table 6.1: Deviation ΔE of the large R asymptotic expansion from the exact calculation of electronic energies for different molecular ions in the state (nlm) (in a.u.).

phaseshift in the continuum based on the short-range asymptotics was obtained [157]. Again, the emphasis was put on the H_2^+ molecular ion for which an impressive agreement was reached in the aforementioned references, as well as in Ref. [158]. Finally, the asymptotic approach has been applied to calculations of the wavefunctions. Notably, Kereselidze *et al.* [159] (and references within) constructed the asymptotic form of quasi-angular and quasi-radial wavefunctions for both small and large internuclear separations. Instead of discussing the details of the listed works here, we refer the reader to the references.

6.4 Molecular potentials

Exact calculations of potential curves and coupling matrix elements from the two-center Schrödinger equation together with the multistate molecular expansion have been used in previous theoretical treatments of charge-exchange collisions corresponding to $(HeH)^{2+}$, $(OH)^{8+}$ and other ions [143,160–162].

We calculated electronic potentials of the molecular ions CH^{6+}, NH^{7+} and OH^{8+}, that can be used within the formulation of charge-exchange collisions that was outlined above. These particular ions play a significant role in CX collisions between the solar wind and hydrogen background that we investigate in chapter 7. Such collisions occur for ion impact velocities of about 0.05 to 1 a.u. Published cross sections [163] suggest that in this velocity range the electron capture occurs in highly excited molecular states, $n = 5$ to $n = 8$. Our calculations were performed for the same states.

Electron capture in slow collisions for multiply charged ions and neutrals (hydrogen) occurs through pseudo-crossings of the adiabatic potential energy curves [164,165]. Basically, the pseudo-crossings are caused by the Coulomb repulsion between the ions after the charge-exchange process has occurred. We identify such crossings in the electronic potentials illustrated in Figures 6.2 to 6.5 below.

To calculate the potentials we used the package *TwoCentre.m* for Mathematica 5.0 [166], that was adapted for the newer version of Mathematica. The package can compute generalized spheroidal harmonics up to arbitrary precision, as well as find solutions of the two-center problem. We illustrate the obtained electronic potentials for several molecular ions below.

6.4.1 $(\mathrm{OH})^{8+}$

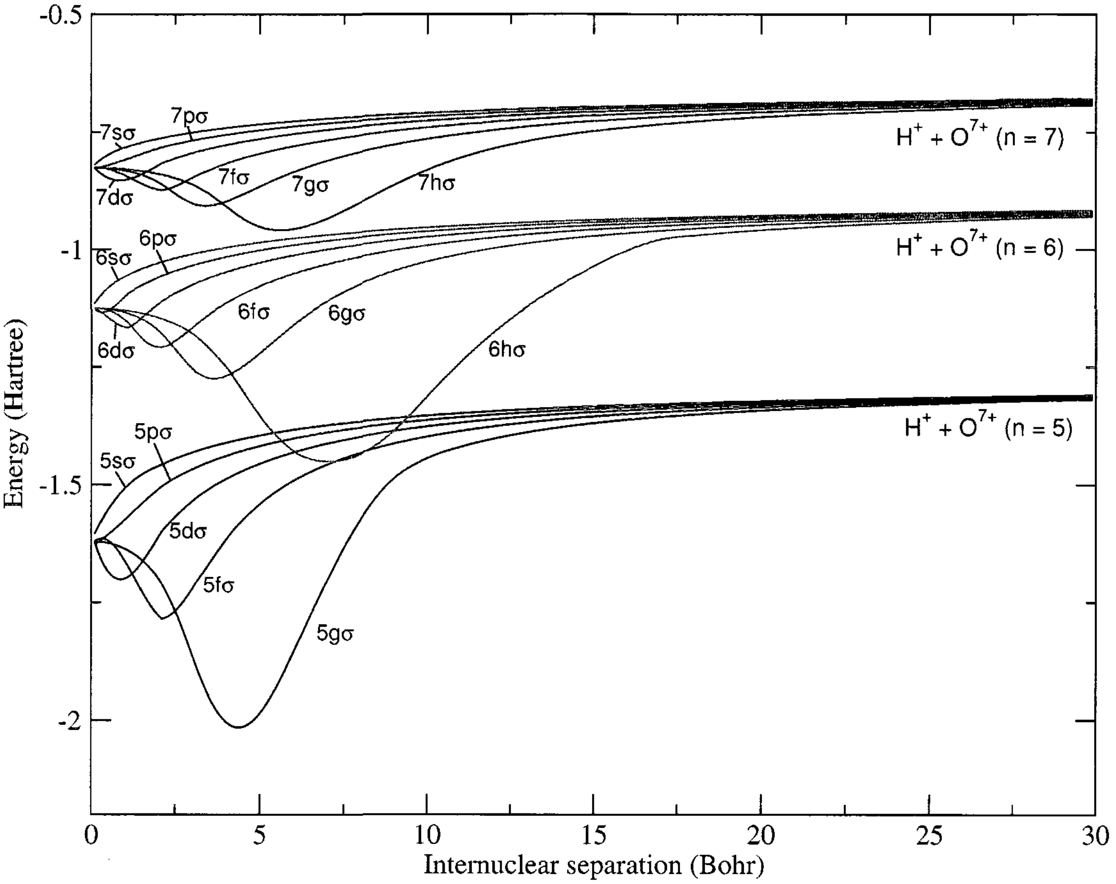

Fig. 6.2: Purely electronic energies as a function of internuclear distance for $n = 5$ to $n = 7$ of $(\mathrm{OH})^{8+}$. The $7i\sigma$ state is not shown.

Molecular potentials for $(\mathrm{OH})^{8+}$ have been calculated by Harel and Salin [143], who also calculated the charge-exchange cross section for the system, using two- and three-state models. We performed a similar calculation of the electronic potentials for all molecular states from $n = 5$ to $n = 7$, with the exception of the $7i\sigma$ state, for which the numerical package could not converge for $R < 11$ Bohr.

Our results match well those of Ref. [143] for the published curves.

The electronic potentials for $m = 0$ are illustrated in Figure 6.2. In the limit of small internuclear separation the energies correctly converge into atomic energy levels of the united atom, while for the large R they converge to the separated atom limit. There are three distinct groups of curves ($n = 5, 6, 7$), each with a subset of potentials for different orbital angular momenta l. The rightmost curves within each group, the one that has the minimum for the lowest energy, corresponds to the highest angular momentum. Only the electronic energies are shown and the Coulomb nuclear repulsion term should be included to obtain the total molecular potentials. Note the state $6g\sigma$ that intersects four states with quantum numbers $n = 5, l = 0$ to 3. A similar behavior is expected from all states with the highest orbital angular momentum for $n > 3$. Such curve crossings play an important role in charge-exchange collisions.

We have also calculated the electronic potentials for all existing orbitals for $n = 5$ case. The curves are illustrated in Figure 6.3. Note the additional crossings that appear. A similar structure is present for other principal quantum numbers.

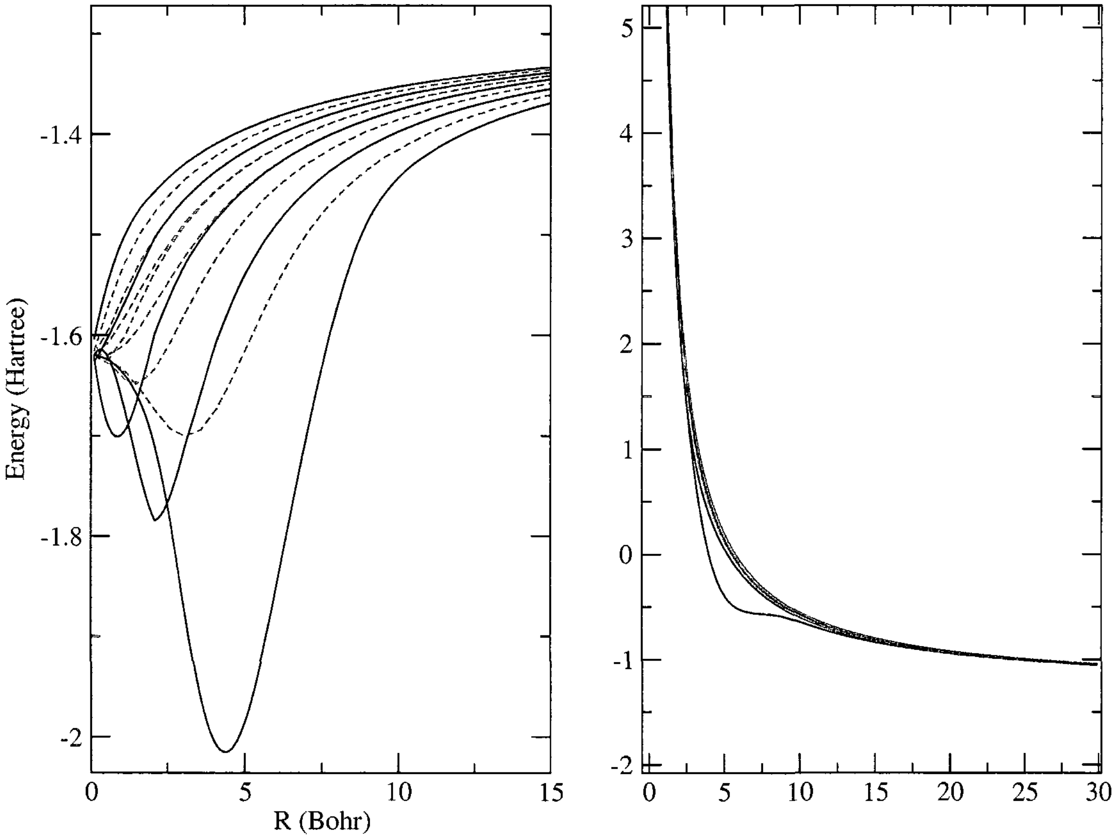

Fig. 6.3: *Left:* Purely electronic energies as a function of internuclear distance for higher orbital angular momentum states for $n = 5$ of $(\mathrm{OH})^{8+}$. *Right:* The total molecular energy, including the repulsive Coulomb term for the same states is shown. Note the inflection point for the $n = 5, l = 4, m = 4$ state.

6.4.2 $(CH)^{6+}$ and $(NH)^{7+}$

In analogy to the $(OH)^{8+}$ case, we have calculated the electronic potentials for $(CH)^{6+}$ and $(NH)^{7+}$ molecular ions. The results are presented in Figures 6.4 and 6.5. As for $(OH)^{8+}$, the electronic potential curves crossings of different types exist for the highest value of the angular momentum l for $n = 5$ and above. We have indicated the avoided crossings that contribute the most to the cross section on graphs.

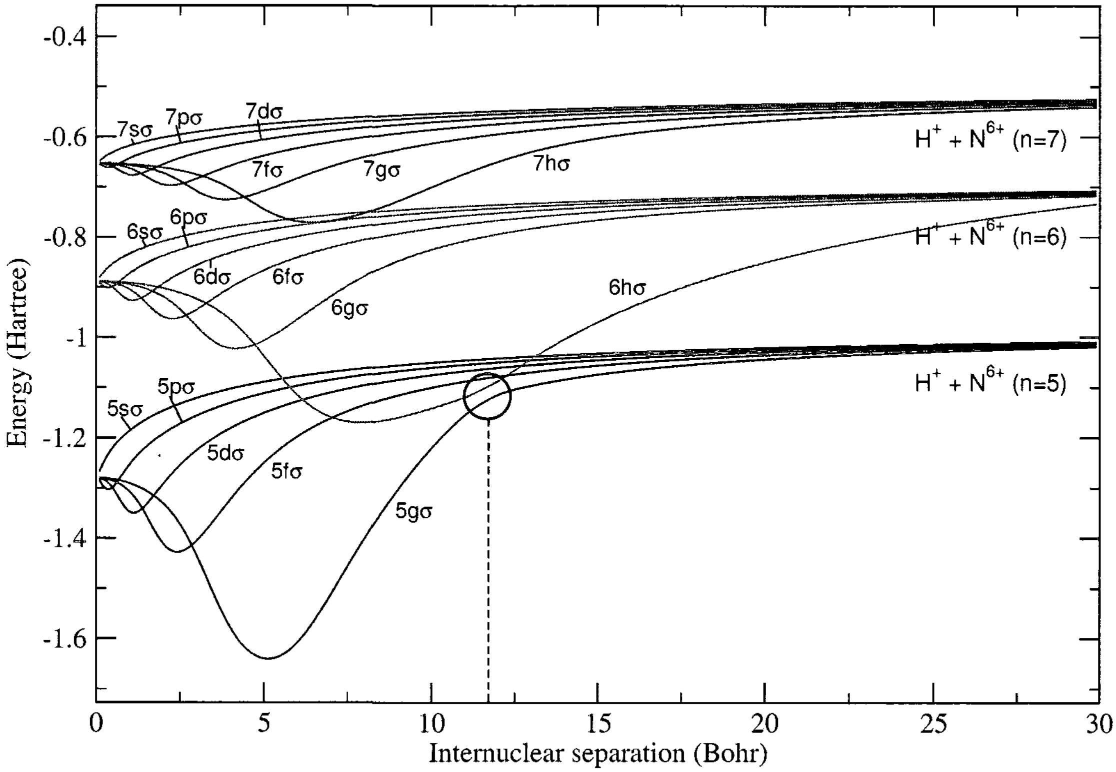

Fig. 6.4: Purely electronic energies as a function of internuclear distance for $n = 5$ to $n = 7$ of $(NH)^{7+}$.

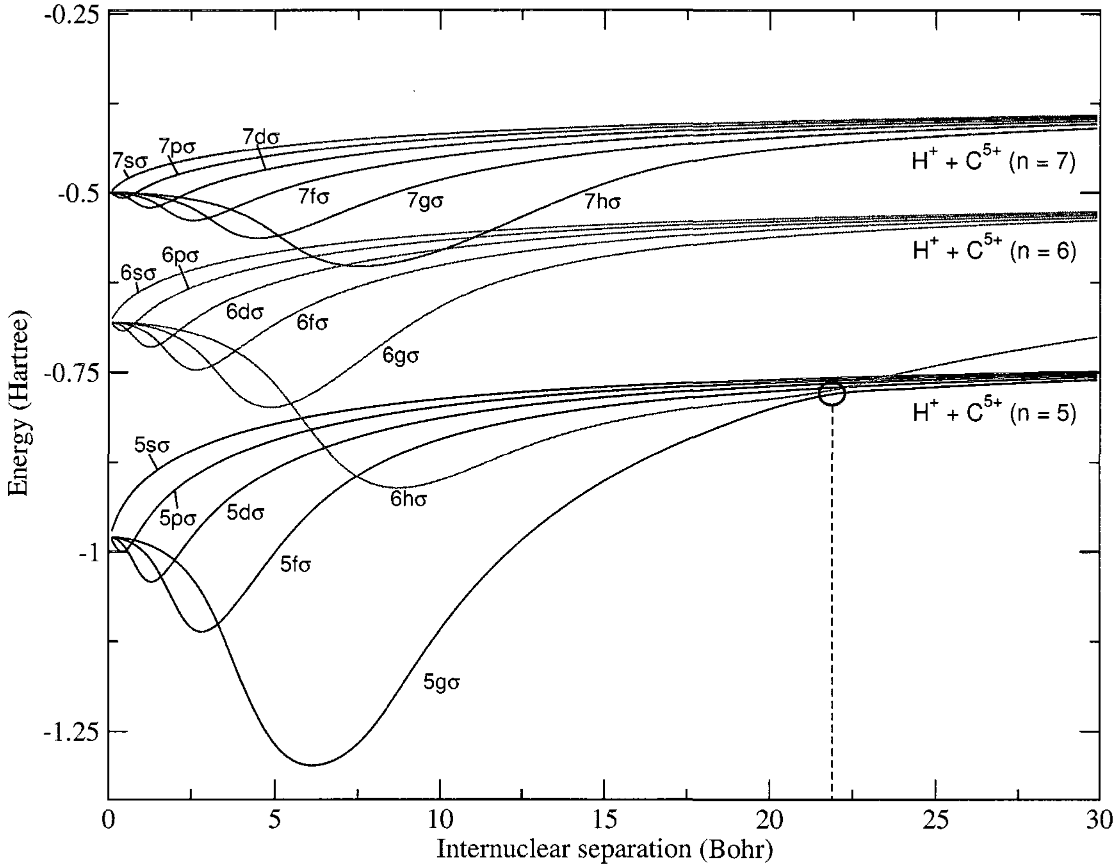

Fig. 6.5: Purely electronic energies as a function of internuclear distance for $n = 5$ to $n = 7$ of $(\mathrm{CH})^{6+}$.

6.4.3 Wavefunctions and matrix elements

The coupling matrix elements relevant for the calculation are given in Eq. (6.2.6). In the molecular formalism, the time derivative of the initial state is replaced by differentiation with respect to d/dR. In addition, we need to calculate the matrix element of the rotational coupling, which can be expressed as the orbital angular momentum operator. See Refs. [139,160] for details. The two matrix elements that need to be evaluated are [160] $\langle\chi_v|\frac{d}{dR}|\chi_v'\rangle$, and $\langle\chi_v|iL_y|\chi_v'\rangle$.

Molecular states that include curve crossings of any type carry the largest contribution to the charge-exchange process. Selecting only such states and truncating everything else is often sufficient to greatly simplify the calculation. For example, if we are interested in the charge-exchange cross section into the $5g\sigma$ state in $(\mathrm{CH})^{6+}$, the logical choice would be to consider the $6h\sigma$ state which has an avoided cross section with the $5g\sigma$ state at about $R = 22\ a_0$. In such a two-state expansion we would calculate the CX cross section using Eq. (6.2.11) with the matrix elements $\langle\chi_{5g\sigma}|d/dR|\chi_{6h\sigma}\rangle$ and $\langle\chi_{5g\sigma}|iL_y|\chi_{6h\sigma}\rangle$.

We first calculated the electronic wavefunctions for the molecular ion states up to $n = 8$. As an example, we illustrate the probability density for $n = 5, m = 0$, for all orbital quantum numbers, in Figure 6.6. The ground state probability density is included for comparison (f). It is clearly visible that the wavefunctions for the two highest angular momenta extend to the hydrogen nucleus (positive z-axis). In fact, for the highest l, the probability density surrounding the hydrogen

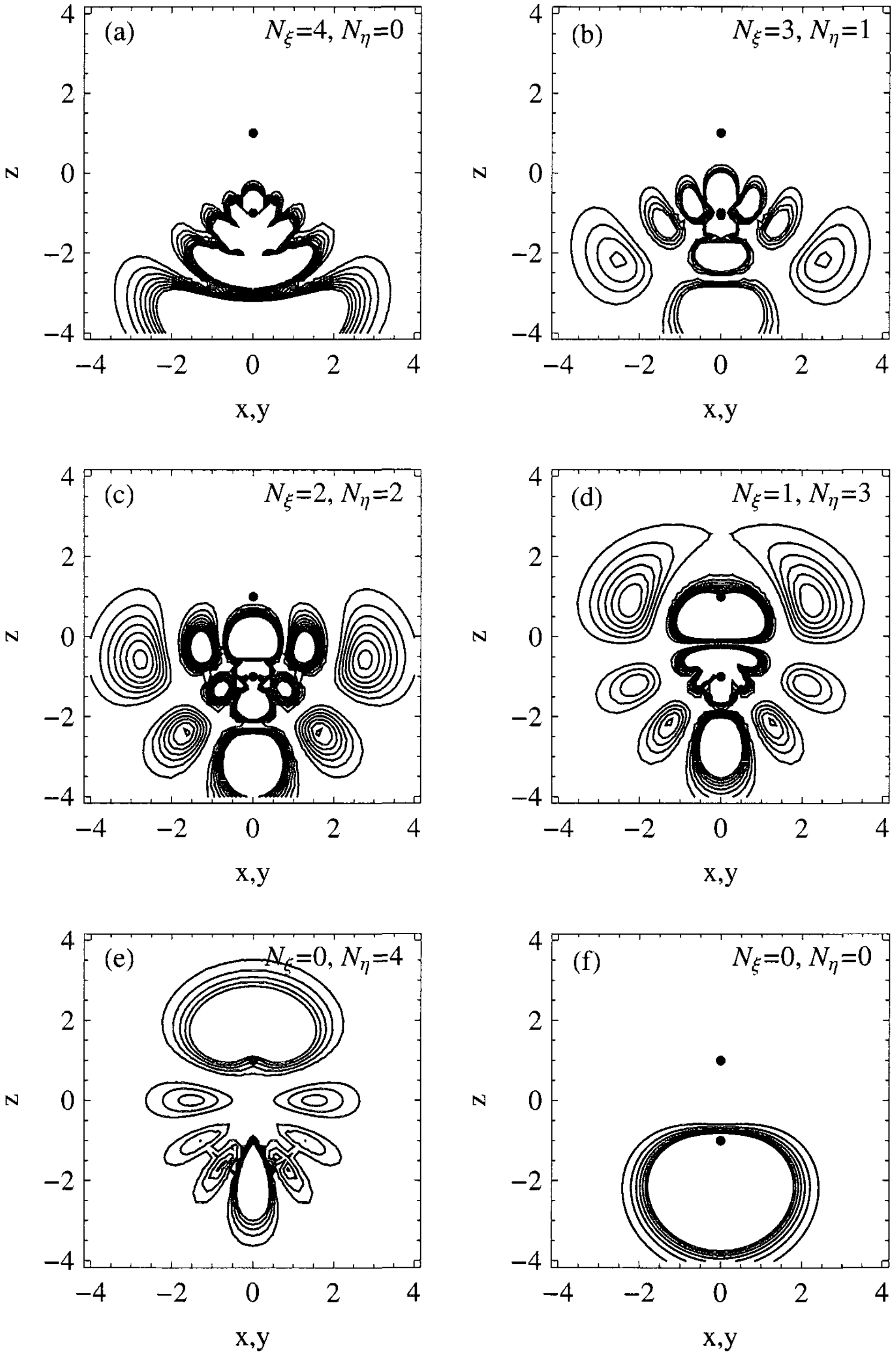

Fig. 6.6: Probability density for $\chi_{n=5,l,m=0}$ state (a-e), and for the $\chi_{n=0,l=0,m=0}$ state (f) of $(\mathrm{OH})^{8+}$. Parameters $E = -1$ and $R = 2$ (in a.u.) were used. Charges $Z_A = 1$ and $Z_B = 8$ are indicated by two dots at $z = 1$ and $z = -1$, respectively.

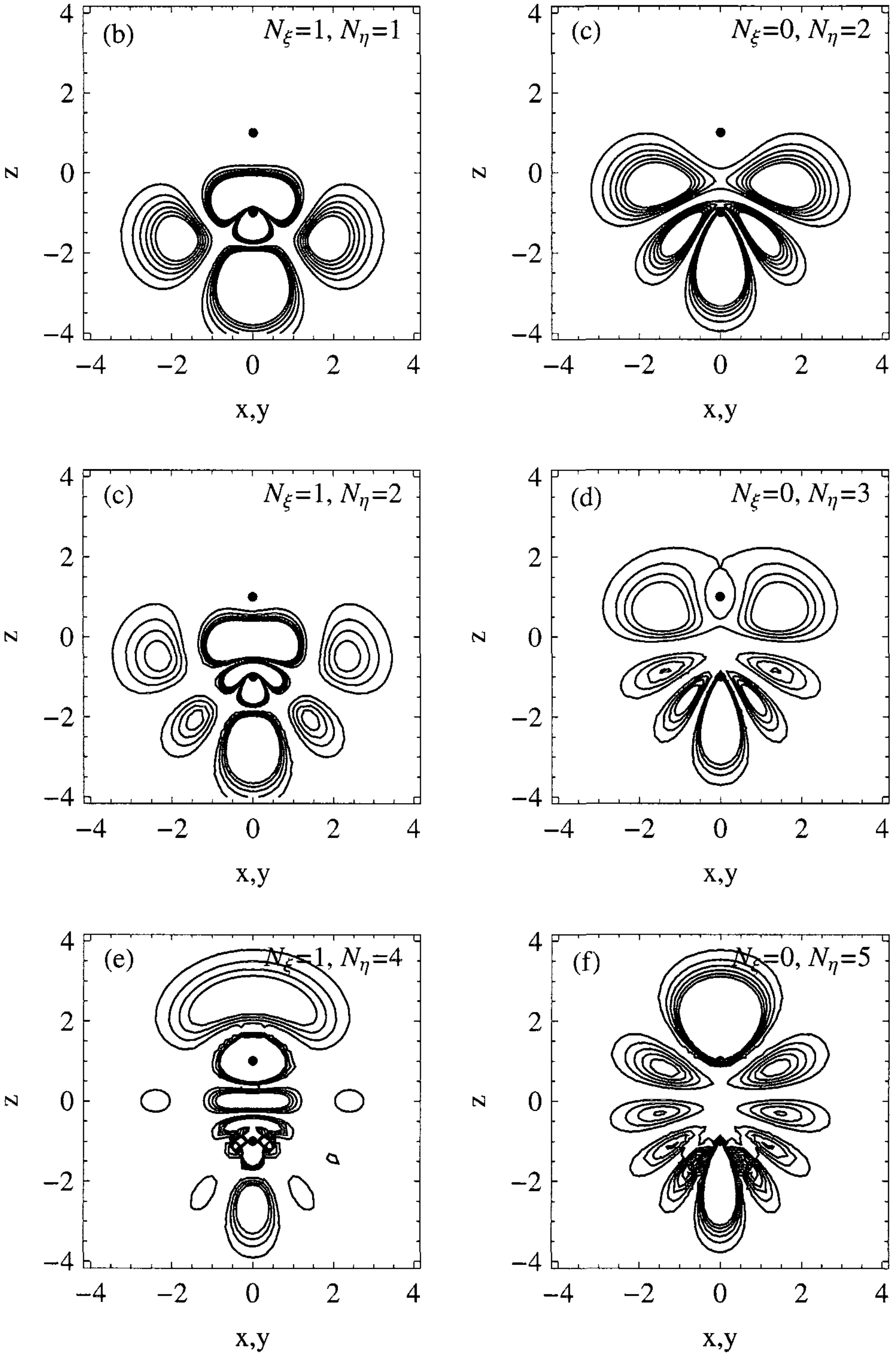

Fig. 6.7: Probability density for the last two l in $\chi_{n=3,4,5,l,m=0}$ of $(\mathrm{OH})^{8+}$. Parameters $E = -1$ and $R = 2$ (in a.u.) were used.

nucleus becomes dominant over that of the fully stripped ion. This can be related to the charge-exchange cross section. Qualitatively, in the stationary picture, if we calculate the spatial overlap of the electronic wavefunctions of the molecular ion with the electronic wavefunctions of the H atom before the CX has occurred, it will be the largest for high l. According to this simple picture, we expect the electron capture cross section to be the largest for the states which exhibit such behavior. Only the highest l state of $n = 4$ and none of the $n \leq 3$ states belong to that category (see Figure 6.7). We confirm this prediction by comparison with the published cross sections for $(OH)^{8+}$ [163].

However, when we attempted to calculate the matrix elements and CX cross sections for $(CH)^{6+}$ and $(OH)^{8+}$, we ran into difficulties related to convergence of numerically evaluated integrals. Because of that, we were not able to reproduce the cross sections published in Ref. [163]. As a result, we used the published cross sections in the calculation of the CX polarization of X-rays in chapter 7.

Chapter 7

Polarization of the charge-exchange X-rays induced in the heliosphere

In this chapter we present the results of a theoretical investigation of the polarization of X-ray emissions induced in charge-exchange (CX) collisions between fully stripped solar wind ions and neutral hydrogen atoms found in the heliosphere. In particular, we investigate the dependence of polarization on the velocity and the spatial distribution of solar wind plasma. Our main objective is to determine if such CX emissions in the Solar System are polarized. To do so, we need to combine the elements of the physics of atom-ion collisions with realistic astrophysical models of the solar wind plasma and neutral heliospheric gas. In chapter 6 we summarized a possible approach to calculating atom-ion charge-exchange cross sections. Here, we take the cross sections as the starting point and apply them to a particular astrophysical problem.

7.1 Introduction

Charge-exchange (CX) collisions between highly charged solar wind (SW) ions and neutral atoms present in heliospheric gas and the Geocorona were recently identified as an efficient mechanism for production of EUV and soft X-ray emissions [167]. There are indications that CX collisions yield between 50% and 80% of heliospheric soft (below 1 keV) X-ray photons [32,35,168], making the CX mechanism a significant contributor to the soft X-ray background (SXRB). Heliospheric CX X-ray emissions are sensitive to the parameters of SW plasma. For example, a strong correlation exists between variations in the SW intensity and composition, and intensity of the soft X-ray background. This has been observed and carefully analyzed [35,169]. These findings indicate that the heliospheric CX X-rays could be used for diagnostics of the solar wind composition and velocities, as well as an independent probe of spatial distribution of heliospheric neutral gas. There are already indications that the existing models of the Local Bubble and interstellar flow of neutral hydrogen may need to be revised to correctly account for charge-exchange emissions. [36,170,171]. Analyzing polarization of the CX emissions is one way to gain more insight into interactions of the SW plasma with neutral heliospheric gas.

While polarization of optical emissions is readily used in investigation of various astrophysical objects, detection of X-ray polarization remains a challenging technical feat. Currently available observational data do not contain information on polarization. However, it is realistic to expect that X-ray polarization will be investigated in future space missions. Consequently, an accurate theoretical consideration of these phenomena is necessary. As an alternative to space-based observations, polarization data are available from laboratory experiments in which CX collisions of atoms and ions of astrophysical interest were studied. In particular, polarization spectroscopy of $O^{5+}(1s^2 3p)$ produced in collisions of O^{6+} with He and H_2 showed that the CX X-rays are polarized and strongly dependent on the projectile velocity, which was varied in the experiment from 0.34 to 0.55 au [172]. It is reasonable to expect the CX X-ray emissions in astrophysical environments to be polarized and exhibit similar velocity dependence.

7.2 Model

A description of the charge-exchange induced X-rays in our Solar system and calculated emission spectra have been published previously [32,168,173,174]. We consider collisions between heavy SW ions and hydrogen gas of the form

$$\begin{aligned} \mathrm{X}^{Q+} + \mathrm{H} &\rightarrow \mathrm{X}^{*(Q-1)+}(np) + \mathrm{H}^+ \\ &\rightarrow \mathrm{X}^{(Q-1)+}(1s) + \mathrm{H}^+ + \gamma, \end{aligned} \tag{7.2.1}$$

where X can be any fully stripped SW ion which undergoes a single relaxation into the ground state of the ion after the electron capture and emits the X-ray photon γ. We assume that H is a major component of the heliospheric gas. This model can be easily extended to include He and other heavy elements.

The line-of-sight (LOS) intensity is given by [173]

$$I^{\mathrm{LOS}} = \frac{1}{4\pi} \int N_{\mathrm{X}^{Q+}}(r) n_{\mathrm{H}}(r) v_{\mathrm{rel}} \sigma_{\mathrm{H,X}^{Q+}} dr, \tag{7.2.2}$$

where $N_{\mathrm{X}^{Q+}}(r)$ is the density of solar wind ions, $n_{\mathrm{H}}(r)$ is the density of hydrogen, v_{rel} is the relative collision velocity and $\sigma_{\mathrm{H,X}^{Q+}}(v_{\mathrm{rel}})$ is the electron capture cross section. We set the upper integration limit to be equal to the heliopause as defined for particular distribution of heliospheric plasma and assume that $v_{\mathrm{rel}} \approx v$, where v is the SW ion velocity. The polarization of the heliospheric X-ray emission in LOS observations can be defined as

$$P = \frac{I_{\|} - I_{\perp}}{I_{\|} + I_{\perp}}, \tag{7.2.3}$$

where $I_{\|}$ and $I_{\perp}$ are the detected intensities which define the degree of polarization.

Projections of angular momenta of the electronic states of the excited SW ions produced in CX collisions are oriented along the local velocity direction of the SW plasma. Assuming that the detector on a satellite can analyze linear polarization of X-ray emissions, the intensity $I = I_{\|} + I_{\perp}$ of radiation, emitted from a selected small volume of the heliosphere and normalized to a single ion emission, can be expressed as [175]

$$I(\psi) = \frac{n_H v_{rel} \sigma_{\mathrm{H,X}^{Q+}}}{4\pi r^2} \left(1 - \frac{1}{2} h^{(2)} A_0^{det} + \frac{3}{2} h^{(2)} A_{2+}^{det}\right), \tag{7.2.4}$$

where r is the distance between the detector and the CX event and $h^{(2)}$ is the ratio of recoupling coefficients which contain elements of orthogonal transformations between the initial and final quantum state [175].

Here, A_0^{det} and A_{2+}^{det} are alignment parameters

$$\begin{aligned} A_0^{det} &= \frac{1}{2}A_0^{col}(3\cos^2\theta - 1), \\ A_{2+}^{det} &= \frac{1}{2}A_0^{col}\sin^2\theta\cos 2\psi, \end{aligned} \tag{7.2.5}$$

where A_0^{col} is the alignment tensor and θ is the angle between the ion velocity and detection axis. Angle ψ indicates orientation of linear polarization analyzer. We define the parallel and perpendicular polarization as $I_{\|} = I(\psi = 0)$ and $I_{\perp} = I(\psi = \pi/2)$. (see Figure 7.1 for details).

We consider a case in which the alignment tensor A_0^{col} is a scalar that can be expressed in terms of velocity-dependent partial cross section $\sigma(m_i, v)$ for electron capture into the atomic state $|j_i m_i\rangle$:

$$A_0^{col} = \frac{\sum_{m_i}\left[3m_i^2 - j_i(j_i+1)\right]\sigma(m_i, v)}{j_i(j_i+1)\sum_i \sigma(m_i, v)} \tag{7.2.6}$$

The parallel and perpendicular intensities in the detector frame are then

$$\begin{aligned} I_{\|} &= \frac{n_H v_{rel}\sigma_{\mathrm{H,X}^{Q+}}}{4\pi r^2}\left[1 - \frac{1}{2}h^{(2)}A_0^{col}(1 - 3\sin^2\theta)\right], \\ I_{\perp} &= \frac{n_H v_{rel}\sigma_{\mathrm{H,X}^{Q+}}}{4\pi r^2}\left(1 - \frac{1}{2}h^{(2)}A_0^{col}\right) \end{aligned} \tag{7.2.7}$$

Since the cross sections $\sigma(m_i, v_{rel})$ depend on the relative velocity of collisions v_{rel} [163], the polarization is also velocity dependent. We neglect cascading relaxation and consider emissions from highly excited states $4p$, $5p$ and $6p$ to the ground state.

In order to calculate the X-ray polarization along the LOS, we work in the planar geometry with the Earth, Sun and the CX event located in the ecliptic plane

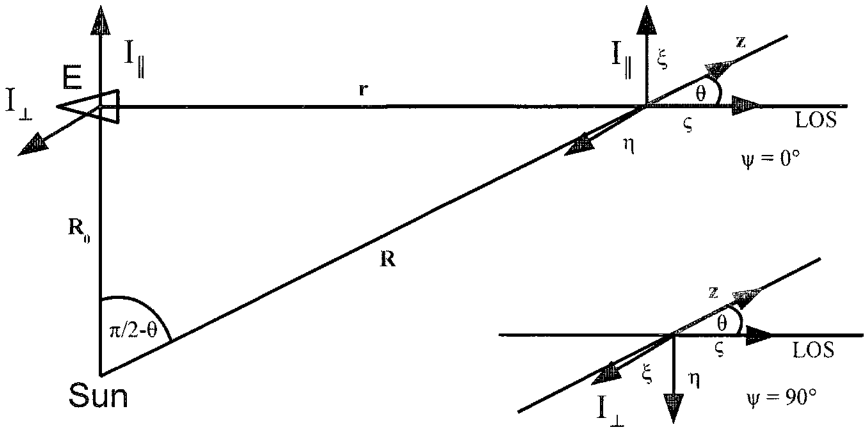

Fig. 7.1: Parallel and perpendicular intensities illustrated in the plane of observation for $\alpha = \pi/2$. Note the change in the direction of $I_{\parallel}$ as the detector is rotated from $\psi = 0$ to $\psi = \pi/2$.

and inside the heliosphere (see Figure 7.2). We consider the Earth (detector) to be at $R_0 = 1$ AU from the Sun in a crosswind direction. The LOS is restricted to the ecliptic plane and expressed by the angle α which increases counterclockwise, where for $\alpha = 0$ the LOS points in the direction of the Sun and for $\alpha = \pi/2$ in the upwind direction. By r and R we indicate distances from the Earth and the Sun to the CX event, respectively. This particular choice of geometry makes it possible to compare upwind and downwind directions of observation for slow SW from a detector on a satellite. The X-ray flux is about 3 times larger for slow SW, prevalent in the ecliptic plane, than for fast SW [32]. Similar geometry was used

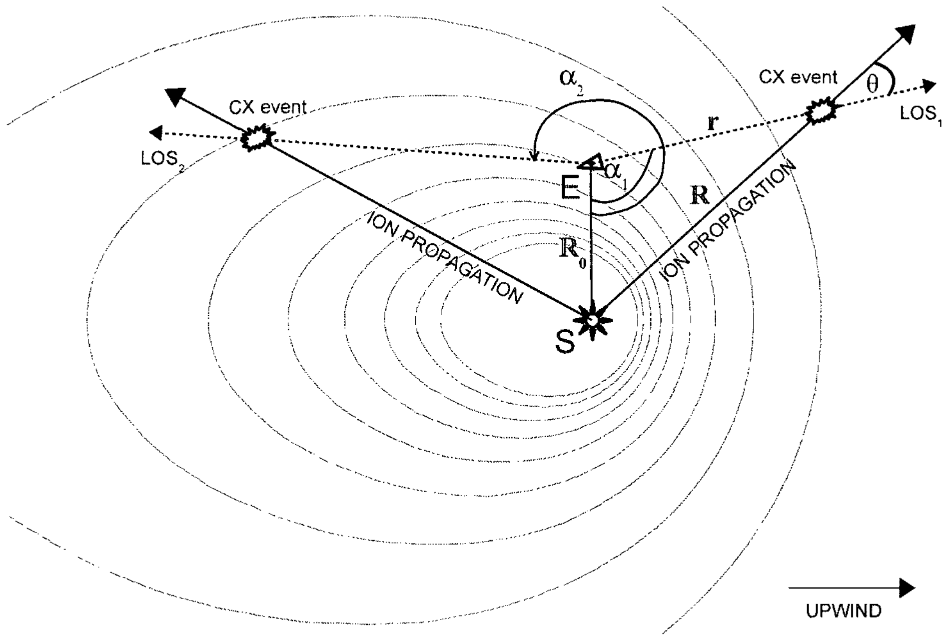

Fig. 7.2: Planar geometry with Earth, Sun and the CX event located in the ecliptic plane. Two different lines-of-sight are illustrated. Heliospheric hydrogen density is shown in the background.

to compare different models of the charge-exchange spectra to ROSAT data [35].

7.2.1 Polarization for the constant hydrogen density

We may easily estimate the scale of X-ray polarization using simplified assumptions about the heliospheric distribution of the SW plasma and neutral gas. If the heliospheric hydrogen density is assumed to be constant, $n_H(r) = n_H^{(0)}$ cm^{-3}, and distribution of SW ions to be isotropic, $N_{XQ+}(R) = N_{XQ+}^{(0)}(\frac{R_0}{R})^2$ cm^{-3}. Here, $N_{XQ+}^{(0)}$ and $n_H^{(0)}$ are densities of the SW ions and hydrogen at $R = 1$ AU from the

Sun, respectively [32]. We can integrate Eqs. (7.2.7) analytically along the LOS to obtain

$$\begin{aligned} I_{\perp}^{\mathrm{LOS}} &= K_0 R_0 \left(A_0^{col} h^{(2)} - 2\right) \alpha_0, \\ I_{\parallel}^{\mathrm{LOS}} &= \frac{1}{2} K_0 R_0 \left[\frac{6 A_0^{col} h^{(2)} R_0 \left(R_H - R_0 \cos\alpha\right)}{R_H^2 + R_0^2 - 2 R_H R_0 \cos\alpha} + \left(4 + A_0^{col} h^{(2)}\right) \alpha_0\right], \quad (7.2.8) \end{aligned}$$

where R_H is the limit to integration along the LOS, which is equal to distance from the Sun to the heliopause, $K_0 = N_{XQ+}^{(0)} n_H v_{rel} \sigma_{\mathrm{H,X^{Q+}}} / 16\pi$ and

$$\alpha_0 = \frac{1}{\sin\alpha}\left[\arctan\left(\frac{R_0 \sin\alpha}{R_0 \cos\alpha - r}\right) - \arctan\left(\frac{r + R_0}{r - R_0} \tan\frac{\alpha}{2}\right)\right]. \quad (7.2.9)$$

The listed intensities in Eq. (7.2.8) are given in units of cm^{-2} s^{-1}.

The analytic solution can be used to predict the qualitative behavior of polarization, though the calculated value is about three times larger than the one obtained for a more realistic model. To demonstrate this, we calculated the angular dependence of the X-ray polarization for emissions from O$^{*7+}(4p, 5p, 6p)$ into its ground state. The results are shown in Figure 7.3.

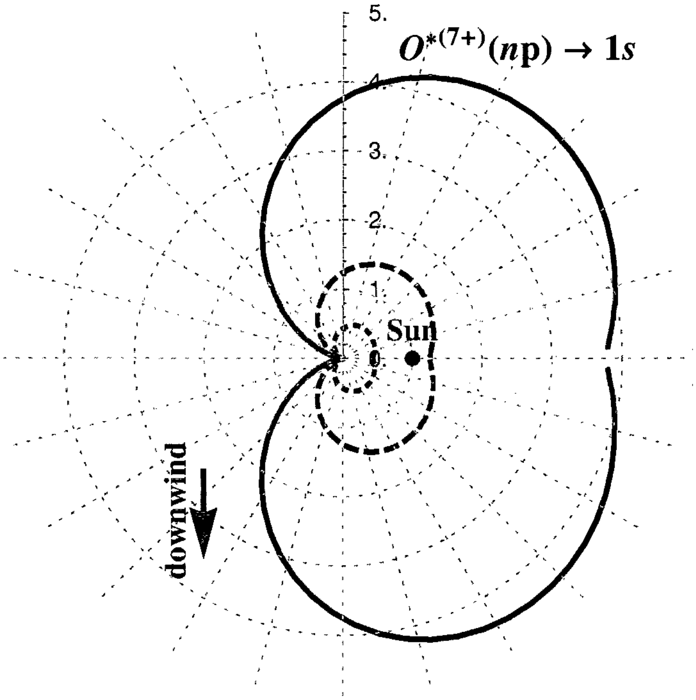

Fig. 7.3: The angular dependence of polarization of the CX X-rays emitted in a single-step deexcitation from $4p$ (solid lines), $5p$ (dashed) and $6p$ (dotted) excited states of $O^{*(7+)}$. Polarization is calculated using analytic formulae (Eq. 7.2.8) and represented by the radius-vector and Earth (observer) is in the origin. The axis for $\alpha = \pi/2$ (LOS in the upwind direction) is shown and the angle increases counterclockwise. Blue cones indicate regions within ±10° of the Sun (right side) or diametrically opposite (left).

7.3 Polarization for realistic distributions of heliospheric gas

7.3.1 Models of heliospheric plasma

The next step is to improve the calculation by replacing the constant hydrogen density with a more realistic distribution. We used two different models of heliospheric plasma in the calculation [34,176]. The model by Lallement [34] assumes simple trajectories in a hot gaseous environment and it is appropriate for describing density distribution of hydrogen and helium for solar maximum or averaged over short-term solar activity. However, the ion density distribution is not calculated within this model. In addition, the Lallement model does not take into account the boundaries between different regions, mainly the hydrogen wall and termination shock. Instead, the density of charged solar wind particles, including the ions of interest to us, is assumed to be isotropic, $N_{X^{Q+}}(R) = N^{(0)}_{X^{Q+}}(R_0/R)^2$, where $N^{(0)}_{X^{Q+}}$ is the ion density at $R = 1$ AU from the Sun. We illustrate this distribution for H and He in Figure 7.4. Note the Helium focusing cone in the downwind direction.

The model by Müller *et al.* [176], is more complex and capable of describing different regions within the Solar System. It is based on multifluid magneto-hydrodynamical (MHD) approach with four interpenetrating fluids. One 'fluid' represents protons of the interstellar and SW plasma and the three remaining components are used to model the neutrals (see [177] for details). We used density

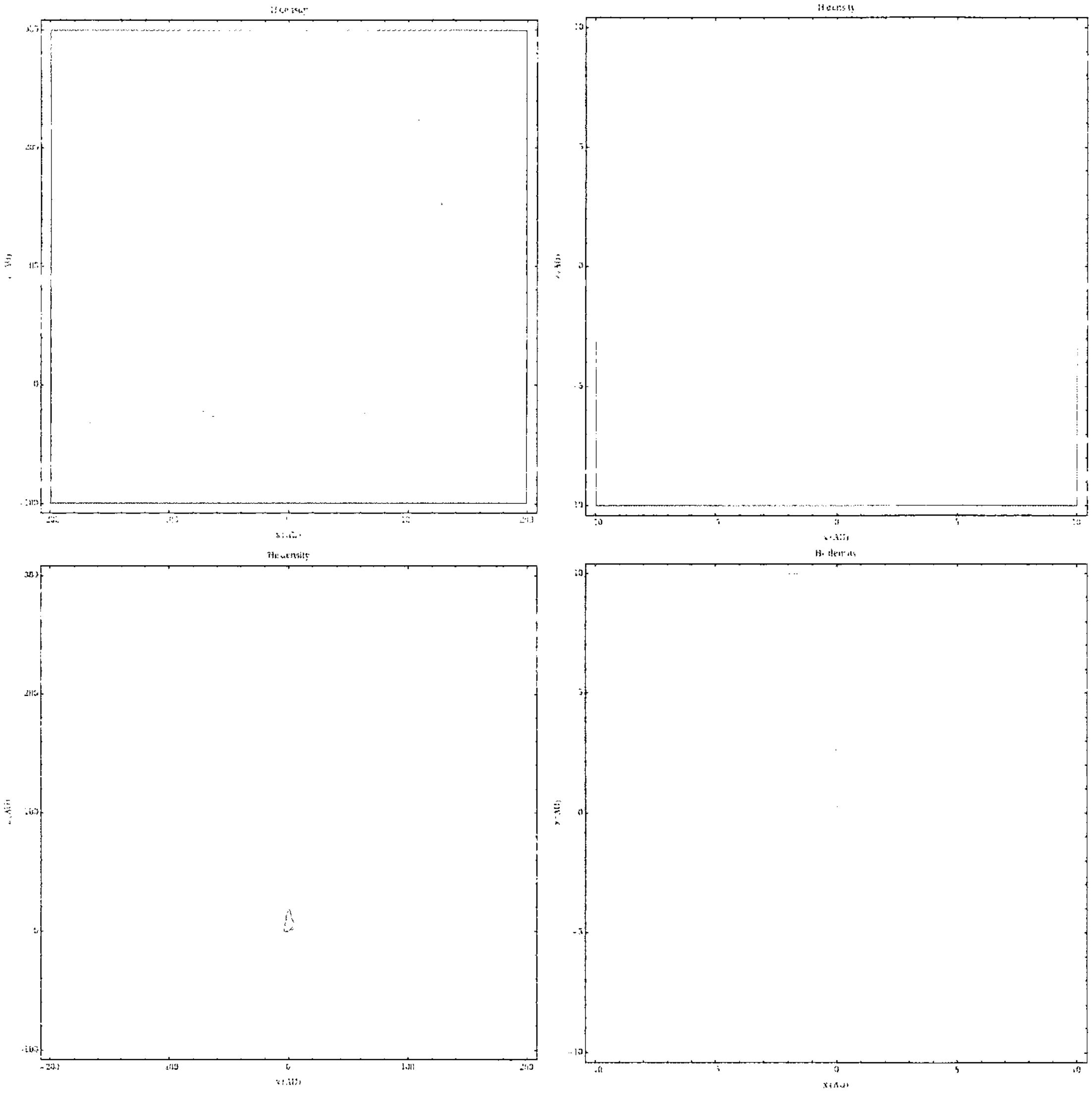

Fig. 7.4: Hydrogen (top) and helium (bottom) density distribution obtained using Lallement model. Darker colors indicate higher density, up to $n_{\rm H} = 0.15$ cm^{-3} for H and $n_{\rm He} = 0.0726$ cm^{-3} for He (in the cone). Upwind direction is pointing down.

distributions of heliospheric hydrogen and SW protons from the Müller model, calculated for conditions that correspond to a solar minimum (Figure 7.5). In fact, the density distributions computed for typical conditions of solar minimum and solar maximum do not seem to differ significantly within the ecliptic plane. On the other hand, variations in solar activity do affect the distributions in the direction perpendicular to the ecliptic plane. We illustrate this for hydrogen in Figure 7.6. As a result, there were no significant differences in polarization for various levels of solar activity.

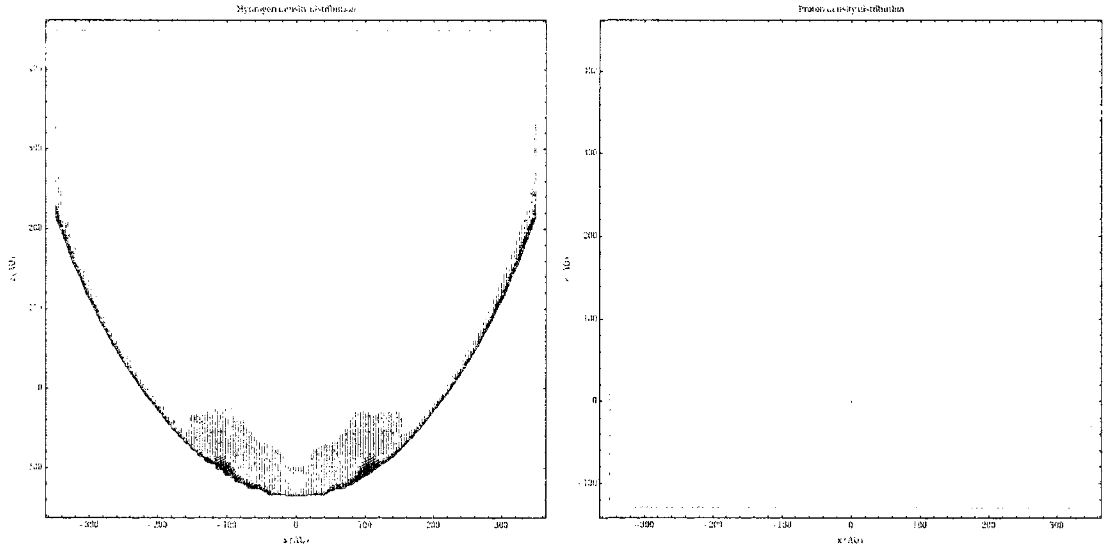

Fig. 7.5: Hydrogen (left) and proton (right) density distributions obtained using the Müller model. Lighter colors correspond to the lower density.

Within the Müller model, density distributions of C^{6+} and O^{8+} ions were obtained by scaling the proton density distribution by the composition factors

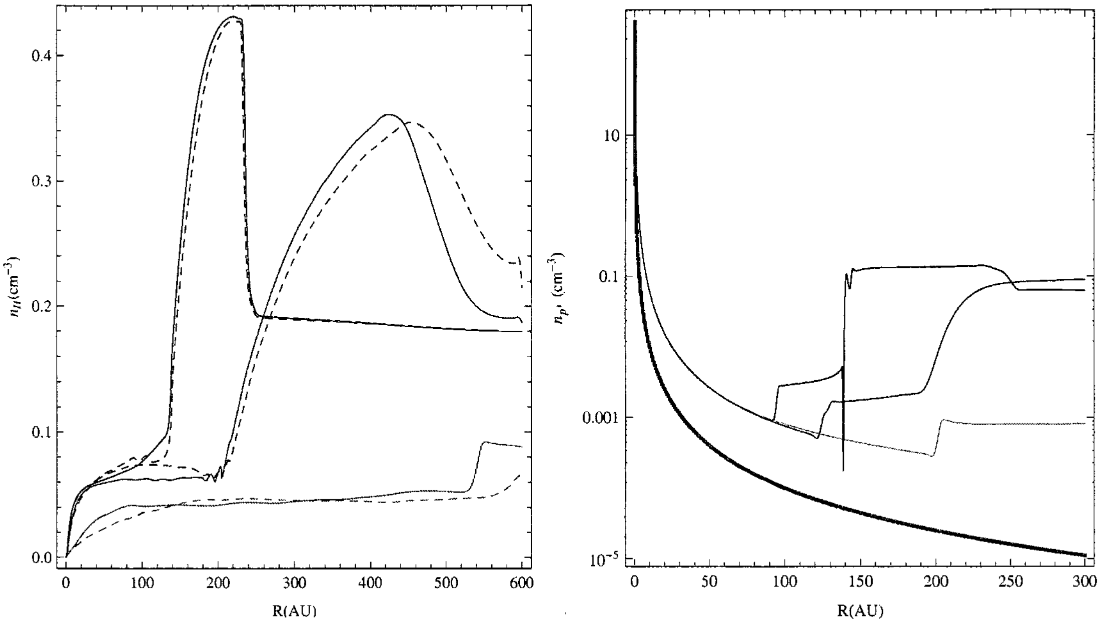

Fig. 7.6: Density distributions from the Müller model. *Left:* Hydrogen density in the upwind (black), downwind (red), and crosswind (blue) direction. Distributions for solar minimum (solid lines) and maximum (dashed lines) are shown. *Right:* Proton density in the upwind (black), downwind (green) and crosswind (blue) direction. The isotropic proton density $N_{p^+}(R) = N_{p^+}^{(0)}(R_0/R)^2$, where $N_{p^+}^{(0)}$ is the proton density at $R = 1$ AU from the Sun, is given for comparison (thick red).

given in [178,168].

For both models the X-ray photon yield was taken to be one and all external perturbations, such as heliospheric and interstellar magnetic fields, were neglected. The polarization was integrated from the detector to the heliopause, a region where the plasma velocity streamlines merge. In the Müller model, the heliopause was determined by a rapid increase in the plasma temperature to $> 10^5$ K, when compared to the interstellar medium. The Lallement model does not describe the heliopause and the limit of integration was set to 300 AU. The angle of observation was varied to cover the whole ecliptic plane ($\alpha = [0, 2\pi]$).

7.3.2 Polarization maps

We calculated the polarization of X-rays for single-photon relaxation from the $4p$, $5p$ and $6p$ excited states of $C^{*(5+)}$ and $O^{*(7+)}$ produced in CX collisions of C^{6+} and O^{8+} ions with heliospheric hydrogen. The probability to populate these excited states is at least an order of magnitude higher than the probability to populate other excited states [163], and selected ions characterize well the slow solar wind, which is dominant in the ecliptic plane [168,179]. The radiative cascade from the excited states was not included in the calculation. Electron capture cross sections depend on the relative velocity of colliding particles; we computed the polarization for solar wind ion velocities from 200-2000 km/s, using the cross sections by [163]. This range of velocities includes both the slow ($v = 400$km/s)

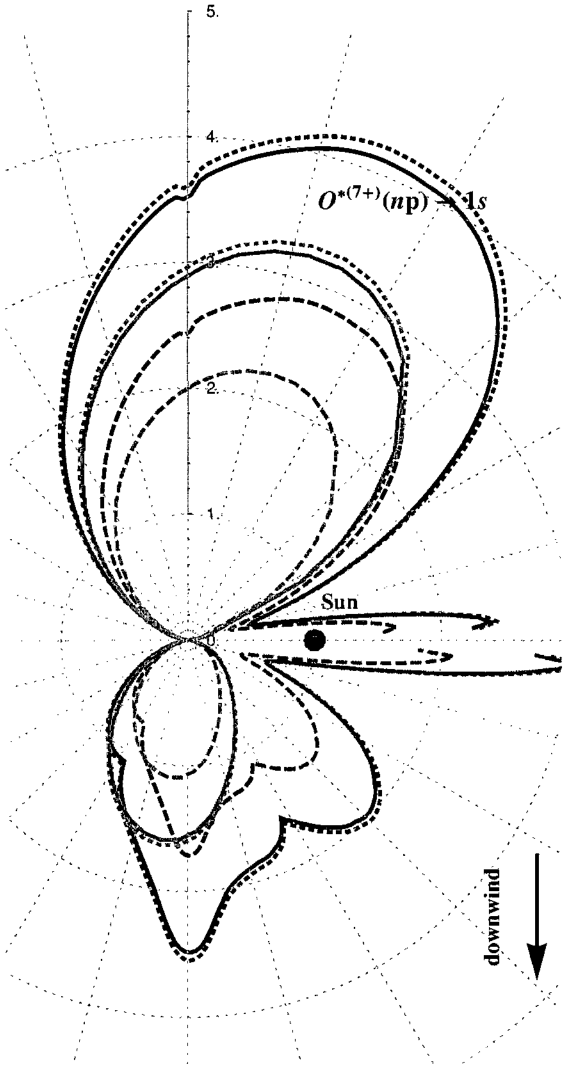

Fig. 7.7: Angular dependence of the polarization of CX X-rays emitted in a single deexcitation from 4*p* (solid lines), 5*p* (dashed) and 6*p* (dotted) excited states of $O^{*(7+)}$. Polarization is given by the radius-vector. The axis for $\alpha = \pi/2$ (LOS in the upwind direction) is shown and the angle increases counterclockwise. Blue cones indicate regions within ±10° of the Sun (right side) or diametrically opposite (left). Results for Lallement (red lines) and Müller (black lines) hydrogen distributions are shown (see text for details).

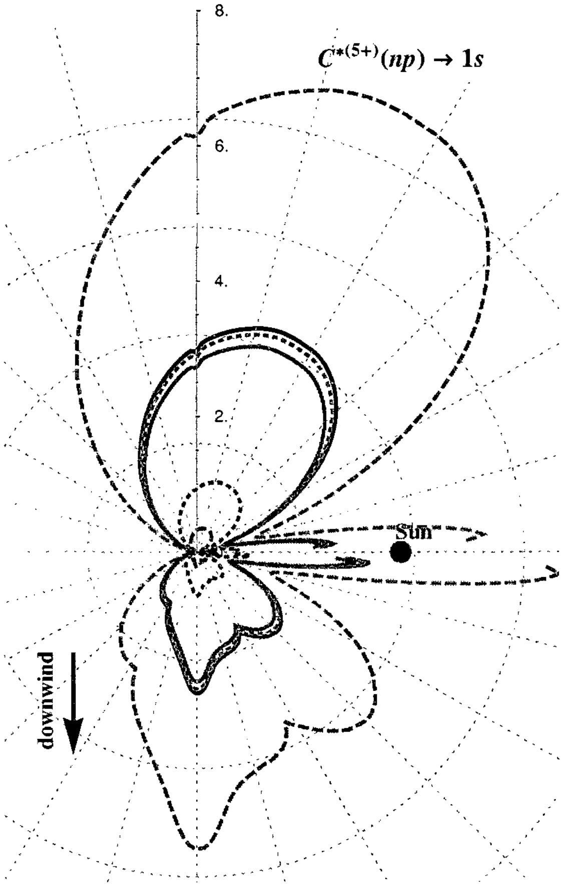

Fig. 7.8: Angular dependence of the polarization of CX X-rays from 4p (solid lines), 5p (dashed) and 6p (dotted) excited states of $C^{*(5+)}$. Polarization is given by the radius-vector as in Fig. 7.7. Polarization for the slow (black) and fast (green) SW ions calculated using Müller hydrogen distribution is shown.

and fast ($v = 750$km/s) solar wind [180]. Since O^{8+} ions are not present in the fast SW we do not show them in the graph. Figure 7.7 illustrates the angular dependence of polarization of the CX X-rays for $O^{*(7+)}$ ion. Results for both distributions are compared for the slow solar wind.

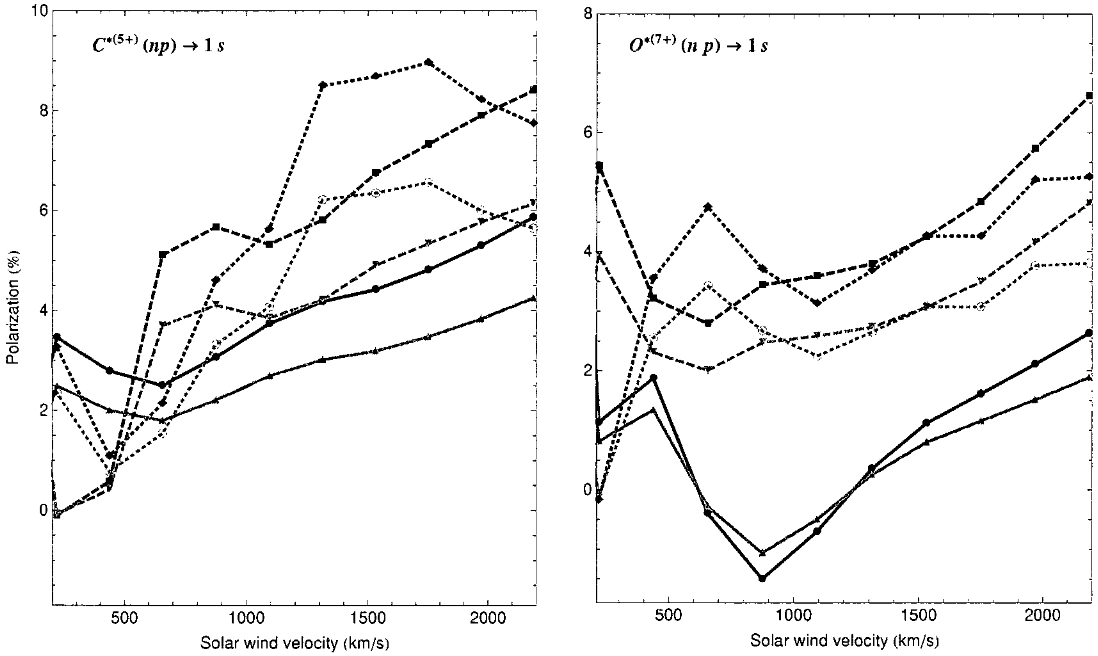

Fig. 7.9: Dependence of CX X-ray polarization on ion velocity for $C^{*(5+)}$ and $O^{*(7+)}$. Emissions from $4p$ (solid), $5p$ (dashed) and $6p$ (dotted) excited states for LOS in upwind (black lines) and downwind (green lines) are shown.

Using the Müller distribution, we calculated the polarization map for $C^{*(5+)}$ ions, for average values of the fast and slow solar wind (Figure 7.8). In case of the slow SW, which is dominant in the ecliptic plane, for emissions from $4p$

state we obtain the polarization of about 3% for the optimal $\alpha_{\rm LOS}$ in the upwind direction and less than 2% in downwind direction. The polarization of the X-ray photons radiated from $5p$ and $6p$ states is less than 1% for the optimal observation geometry.

The results are more promising for the fast SW ions. The highest polarization, $P = 7\%$, for the optimal $\alpha_{\rm LOS}$ in the upwind direction, is obtained for emissions from $5p$ state of $C^{*(5+)}$. Unfortunately, the fast SW is not present in the low heliographic latitudes (less than 20° within the ecliptic plane). Nevertheless, this result suggests that it may be possible to observe higher polarization of the CX X-ray emissions at higher heliographic latitudes, out of the ecliptic plane.

7.4 Discussion

We demonstrated that the X-rays emitted in the charge-exchange collisions between neutral heliospheric hydrogen and fully stripped oxygen O^{8+} and carbon C^{6+} ions are polarized. These ions are important constituents of the solar wind and participate in charge-exchange processes that produce X-rays. This includes the CX with heliospheric hydrogen and helium, as well as CX with the atoms present in planetary and cometary atmospheres. The polarization is found to be strongly dependent on the density of the neutral gas within several AUs of the Sun, as well as on the velocity of SW ions.

Two models were used to describe the heliospheric neutrals and ions. The

MHD model by Müller [176] is more realistic of the two, as it includes four components of the heliospheric plasma, and describes the local environment up to the termination shock. In our calculation of the polarization maps, we used hydrogen and proton density distributions for solar minimum conditions that were obtained from this model. We also constructed a polarization map using a simpler hydrogen density distribution from Lallement model, and found a good qualitative agreement between the two.

While the calculated polarization is small, $P < 10\%$ for the optimal choice of the observational geometry, it is not insignificant. If measured with the sufficient precision, the polarization could be a valuable complement to the X-ray spectra. For example, the polarization seems to be very dependent on the heliospheric gas density and it could be used to extract additional information about the distribution of neutral gas within the Solar System. Alternatively, the polarization can help distinguish between the CX emission spectra and extract information about the ion velocity distribution. In addition, polarization should be taken into account in accurate measurements of the CX emission intensity.

This study can be extended to include heliospheric helium as well as higher gas densities found close to the bowshock region of our Solar System. Moreover, using a 3D density distribution of heliospheric plasma would make it possible to calculate the polarization in the whole space. Finally, provided that the sufficiently accurate detection is possible, polarization could offer valuable information about other astrophysical CX processes and environments.

Chapter 8

Conclusion and future directions

This dissertation consists of two distinct parts unified by the underlying scattering theory. First part, following the brief summary of relevant theory presented in chapter 2, is dedicated to diatomic collisions of trapped, ultracold alkali metal atoms in external fields. Specifically, the focus is on detailed theoretical analysis of magnetic Feshbach resonances, and possible applications of their unique properties to physics of ultracold atomic gases. We used a multichannel scattering theory to find and characterize Feshbach resonances in Li+Na and Li+Rb ultracold mixtures. These results were used to produced new sets of molecular potentials that correctly reproduced the resonances and were the starting point for developing two novel applications of Feshbach resonances.

The first one, a technique that we named Feshbach-optimized photoassociation, was developed as we were exploring the effects of Feshbach resonances on the scattering wavefunction. We found that if a quasi-bound Feshbach state was used as the initial state for photoassociating two colliding ultracold atoms into a molecule, the formation rate was greatly enhanced. Photoassociation is a well-known and proven technique; it has been widely used in atomic spectroscopy from the days before the ultracold temperatures were attainable, and quickly adopted as an essential tool for forming cold molecules. We were very excited to realize that a simple addition of an external magnetic field tuned to a Feshbach resonance can lead to significantly enhanced photoassociative formation rate. Chapter 4 presents quantitative analysis of Feshbach-optimized photoassociation using 1- and 2-photon schemes in ultracold Li+Na and Li+Rb mixtures.

While working with Feshbach resonances and photoassociation rates, we realized that it is possible to find a connection between the Feshbach-optimized photoassociation rate and the electron-proton mass ratio $\beta = m_e/m_p$, which is a fundamental constant. Consequently, it may be possible to conduct a precision measurement experiment to determine the variations of the two quantities with the precision approaching the current experimental limits. Such an experiment would provide an independent test of the time-variation of β. An interesting property of measuring the rate, as compared to measuring the scattering length, is that it would be possible to perform measurements at its minimum and still benefit from the resonant enhancement while avoiding the saturation effects.

In the second part of this work, covered in chapters 6 and 7, we extended the study of the X-rays produced in charge-exchange atom-ion collisions between fully stripped solar wind ions and neutral heliospheric gas. The heliospheric X-rays were predicted and observed in the past decade, but the ratio of local (produced in charge-exchange processes or scattering in the Solar System) vs. extrasolar (mainly galactic) X-rays in that particular region of the spectrum remains uncertain. We relied on Fano-Macek theory [175] to model the polarization of the heliospheric charge-exchange X-rays, and on the current models of the heliospheric plasma [34,181] to calculate it. Our prediction, based on three characteristic solar wind ions, C^{6+}, N^{7+}, and O^{8+}, is that we can expect the polarization of the X-rays to be 5-10%. If the next-generation X-ray space telescope will include a polarimeter, it will be possible to measure the polarization and gain an extra piece of information about the underlying physical process.

There are different directions in which this work can be extended. Ultracold atomic and molecular physics is rapidly developing as a field, and accurate collisional cross sections for various processes are needed for further theoretical modeling. At the same time, a compendium of Feshbach resonances is still incomplete even for diatomic alkali metal atoms. Feshbach resonances are an invaluable tool in ultracold physics experiments and, clearly, there is a need to extend it to other diatomic mixtures. The other techniques proposed in this work are rather general. For example, Feshbach-optimized photoassociation could offer a way to produce stable ultracold molecules needed for experiments with optical lattices and realizations of platforms for quantum computing with neutral atoms.

On the astrophysical side, the fact that the charge-exchange X-rays induced by the solar wind are polarized is not restricted to the heliosphere. Our theory can be easily applied to other objects within our Solar System, such as the Jovian system, Saturn and Mars. In addition, perhaps even more interesting environments in which charge-exchange X-ray emission is likely to occur, are extrasolar planets of the hot Jupiter type and protoplanetary disks surrounding young stars.

Bibliography

[1] J. Dalibard and C. Cohen-Tannoudji, J. Opt. Soc. Am. B **2**, 1707 (1985).

[2] C. N. Cohen-Tannoudji, Rev. Mod. Phys. **70**, 707 (1998).

[3] W. Phillips, J. Prodan, and H. Metcalf, J. Opt. Soc. Am. B: Opt. Phys **2**, 1751 (1985).

[4] J. Weiner *et al.*, Rev. Mod. Phys. **71**, 1 (1999).

[5] W. D. Phillips, Rev. Mod. Phys. **70**, 721 (1998).

[6] W. Ketterle, Rev. Mod. Phys. **74**, 1131 (2002).

[7] F. Dalfovo *et al.*, Rev. Mod. Phys. **71**, 463 (1999).

[8] W. C. Stwalley, Phys. Rev. Lett. **37**, 1628 (1976).

[9] T. Köhler, K. Góral, and P. S. Julienne, Rev. Mod. Phys. **78**, 1311 (2006).

[10] H. R. Thorsheim, J. Weiner, and P. S. Julienne, Phys. Rev. Lett. **58**, 2420 (1987).

[11] W. Stwalley and H. Wang, J. Mol. Spectrosc. **195**, 194 (1999).

[12] J. Doyle *et al.*, Eur. Phys. J. D **31**, 149 (2004).

[13] K. M. Jones *et al.*, Rev. Mod. Phys. **78**, 483 (2006).

[14] A. J. Kerman *et al.*, Phys. Rev. Lett. **92**, 033004 (2004).

[15] J. M. Sage *et al.*, Phys. Rev. Lett. **94**, 203001 (2005).

[16] K.-K. Ni *et al.*, Science **322**, 231 (2008).

[17] S. Ospelkaus *et al.*, Nat. Phys. **4**, 622 (2008).

[18] I. Deutsch, G. Brennen, and P. Jessen, Fortschr. Phys. **48**, 925 (2000).

[19] P. Jessen, in *Scalable quantum computers: paving the way to realization*, edited by S. L. Braunstein and H.-K. Lo (Wiley-VCH Verlag, Berlin, Germany, 2001), p. 155.

[20] G. K. Brennen *et al.*, Phys. Rev. Lett. **82**, 1060 (1999).

[21] N. Balakrishnan and A. Dalgarno, Chem. Phys. Lett. **341**, 652 (2001).

[22] S. Ospelkaus *et al.*, Science **327**, 853 (2010).

[23] C. Zipkes *et al.*, Nature **464**, 388 (2010).

[24] A. T. Grier *et al.*, Phys. Rev. Lett. **102**, 223201 (2009).

[25] R. Côté and A. Dalgarno, Phys. Rev. A **62**, 012709 (2000).

[26] V. Krasnopolsky *et al.*, Science **277**, 1488 (1997).

[27] C. Lisse *et al.*, Science **274**, 205 (1996).

[28] T. Cravens, Geophys. Res. Lett. **24**, 105 (1997).

[29] V. Krasnopolsky *et al.*, Icarus **160**, 437 (2002).

[30] V. Krasnopolsky, J. Greenwood, and P. Stancil, Space Sci. Rev. **113**, 271 (2004).

[31] T. Cravens, Science **296**, 1042 (2002).

[32] A. Bhardwaj *et al.*, Planet. Space Sci. **55**, 1135 (2007).

[33] I. P. Robertson *et al.*, Space Sci. Rev. **97**, 401 (2001).

[34] R. Lallement, A & A **418**, 143 (2004).

[35] D. Koutroumpa *et al.*, Space Sci. Rev. **143**, 217 (2009).

[36] B. Y. Welsh and R. L. Shelton, AP&SS **323**, 1 (2009).

[37] S. L. Snowden, Space Sci. Rev. **143**, 253 (2009).

[38] N. F. Mott and H. S. W. Massey, *The Theory of Atomic Collisions*, 3rd ed. (Oxford University Press, New York, USA, 1987).

[39] J. Taylor, *Scattering theory: the quantum theory on nonrelativistic collisions* (Wiley, New York, 1972).

[40] R. Newton, *Scattering theory of waves and particles*, 2nd ed. (Dover Publications, New York, 2002).

[41] H. Friedrich, *Theoretical atomic physics* (Springer-Verlag, New York, 1998).

[42] S. Inouye *et al.*, Nature **392**, 151 (1998).

[43] H. Lefebvre-Brion and R. Field, *The spectra and dynamics of diatomic molecules*, 2nd ed. (Academic Press, New York, 2004).

[44] L. E. Ballentine, *Quantum Mechanics: A Modern Development* (World Scientific, Singapore, 1998).

[45] R. Zare, *Angular momentum: understanding spatial aspects in chemistry and physics* (John Wiley & Sons, New York, 1988).

[46] J. Burke Jr, Ph.D. thesis, University of Colorado, 1999.

[47] P. Bunker, J. Mol. Spectr. **28**, 422 (1968).

[48] M. Born and R. Oppenheimer, Ann. Phys. **84**, 457 (1927).

[49] A. Carrington, D. Levy, and T. Miller, Adv. Chem. Phys. **18**, 149 (1970).

[50] L. Piela, *Ideas of quantum chemistry* (Elsevier, Amsterdam, The Netherlands, 2007).

[51] B. Smirnov and M. Chibisov, JETP **21**, 624 (1965).

[52] K. Tang, J. Toennies, and C. Yiu, Int. Rev. Phys. Chem. **17**, 363 (1998).

[53] M. Marinescu, J. F. Babb, and A. Dalgarno, Phys. Rev. A **50**, 3096 (1994).

[54] E. Arimondo, M. Inguscio, and P. Violino, Rev. Mod. Phys. **49**, 31 (1977).

[55] E. Tiemann and J. Ogilvie, J. Mol. Spectr. **165**, 377 (1994).

[56] C. Cohen-Tannoudji, B. Diu, and F. Laloe, *Quantum mechanics* (John Wiley & Sons, New York, 1977).

[57] E. Tiemann *et al.*, Phys. Rev. A **79**, 42716 (2009).

[58] J. Jackson, *Classical Electrodynamics*, 2nd ed. (John Wiley & Sons, New York, 1975).

[59] C. C. Ticknor, Ph.D. thesis, University of Colorado, 2005.

[60] J. M. Brown and A. Carrington, *Rotational Spectroscopy of Diatomic Molecules* (Cambridge University Press, New York, 2003).

[61] E. Tiesinga, B. J. Verhaar, and H. T. C. Stoof, Phys. Rev. A **47**, 4114 (1993).

[62] E. Timmermans *et al.*, Phys. Rev. Lett. **83**, 2691 (1999).

[63] C. R. M. Greiner and D. Jin, Nature **426**, 537 (2003).

[64] S. Jochim *et al.*, Science **302**, 2101 (2003).

[65] C. A. Stan *et al.*, Phys. Rev. Lett. **93**, 143001 (2004).

[66] C. Chin *et al.*, Phys. Rev. A **70**, 32701 (2004).

[67] P. Pellegrini, M. Gacesa, and R. Côté, Phys. Rev. Lett. **101**, 053201 (2008).

[68] K. M. Jones *et al.*, Rev. Mod. Phys. **78**, 483 (2006).

[69] E. Taylor-Juarros, R. Côté, and K. Kirby, Eur. Phys. J. D **31**, 213 (2004).

[70] E. Juarros *et al.*, Phys. Rev. A **73**, 041403 (2006).

[71] A. J. Moerdijk, B. J. Verhaar, and A. Axelsson, Phys. Rev. A **51**, 4852 (1995).

[72] B. R. Johnson, J. Comput. Phys. **13**, 445 (1973).

[73] V. Kokoouline *et al.*, J. Chem. Phys. **110**, 9865 (1999).

[74] B. Deh *et al.*, Phys. Rev. A **77**, 010701 (2008).

[75] C. Marzok *et al.*, Phys. Rev. A **79**, 012717 (2009).

[76] Z. Li *et al.*, Phys. Rev. A **78**, 022710 (2008).

[77] M. Gacesa, P. Pellegrini, and R. Côté, Phys. Rev. A **78**, 10701 (2008).

[78] E. Tiesinga *et al.*, Phys. Rev. A **46**, R1167 (1992).

[79] J. Harriman, *Theoretical foundations of electron spin resonance* (Academic Press, New York, 1978).

[80] S. G. Karshenboim, Phys. Usp. **51**, 1019 (2008).

[81] R. M. C. Ahn, J. P. H. W. v. d. Eijnde, and B. J. Verhaar, Phys. Rev. B **27**, 5424 (1983).

[82] H. T. C. Stoof, J. M. V. A. Koelman, and B. J. Verhaar, Phys. Rev. B **38**, 4688 (1988).

[83] A. Bambini and S. Geltman, Phys. Rev. A **65**, 062704 (2002).

[84] B. R. Johnson, J. Comput. Phys. **13**, 445 (1973).

[85] C. E. Fellows, J. Chem. Phys. **94**, 5855 (1991).

[86] M. Aymar and O. Dulieu, J. Chem. Phys. **122**, 204302 (2005).

[87] A. Derevianko, J. F. Babb, and A. Dalgarno, Phys. Rev. A **63**, 052704 (2001).

[88] S. G. Porsev and A. Derevianko, J. Chem. Phys. **119**, 844 (2003).

[89] C. A. Stan, Ph.D. thesis, Cambridge, MA, USA, 2005.

[90] W. Ketterle, Private communication.

[91] E. Timmermans and R. Côté, Phys. Rev. Lett. **80**, 3419 (1998).

[92] M. Houbiers *et al.*, Phys. Rev. A **57**, R1497 (1998).

[93] M. Brown-Hayes and R. Onofrio, Phys. Rev. A **70**, 063614 (2004).

[94] C. Marzok *et al.*, Phys. Rev. A **76**, 052704 (2007).

[95] R. Côté, R. Onofrio, and E. Timmermans, Phys. Rev. A **72**, 041605 (2005).

[96] H. Ouerdane and M. J. Jamieson, Phys. Rev. A **70**, 022712 (2004).

[97] M. Korek, G. Younes, and S. Al-Shawa, J. Mol. Struct. **899**, 25 (2009).

[98] M. Korek *et al.*, Chem. Phys. **256**, 1 (2000).

[99] B. Marcelis *et al.*, Phys. Rev. A **70**, 012701 (2004).

[100] M. Anderlini *et al.*, Phys. Rev. A **71**, 061401 (2005).

[101] D. DeMille, Phys. Rev. Lett. **88**, 067901 (2002).

[102] A. Fioretti *et al.*, Phys. Rev. Lett. **80**, 4402 (1998).

[103] O. Dulieu and C. Gabbanini, Rep. Prog. Phys. **72**, 086401 (2009).

[104] M. W. Zwierlein *et al.*, Phys. Rev. Lett. **91**, 250401 (2003).

[105] K. Xu *et al.*, Phys. Rev. Lett. **91**, 210402 (2003).

[106] D. E. Miller *et al.*, Phys. Rev. Lett. **99**, 070402 (2007).

[107] A. Altmeyer *et al.*, Phys. Rev. Lett. **98**, 040401 (2007).

[108] M. Greiner, C. A. Regal, and D. S. Jin, Phys. Rev. Lett. **94**, 070403 (2005).

[109] G. B. Partridge *et al.*, Phys. Rev. Lett. **95**, 020404 (2005).

[110] E. Juarros, K. Kirby, and R. Côté, J. Phys. B **39**, S965 (2006).

[111] F. A. van Abeelen and B. J. Verhaar, Phys. Rev. Lett. **83**, 1550 (1999).

[112] S. J. J. M. F. Kokkelmans, H. M. J. Vissers, and B. J. Verhaar, PRA **63**, 031601 (2001).

[113] B. Laburthe Tolra *et al.*, Europhys. Lett. **64**, 171 (2003).

[114] F. A. van Abeelen, D. J. Heinzen, and B. J. Verhaar, Phys. Rev. A **57**, R4102 (1998).

[115] M. Aymar and O. Dulieu, Private communication.

[116] P. Pellegrini and R. Côté, New J. Phys. **11**, 055047 (2009).

[117] E. A. Juarros, Ph.D. thesis, University of Connecticut, 2007.

[118] J. L. Bohn and P. S. Julienne, Phys. Rev. A **54**, R4637 (1996).

[119] E. Kuznetsova *et al.*, New J. Phys. **11**, (2009).

[120] E. Reinhold *et al.*, Phys. Rev. Lett. **96**, 151101 (2006).

[121] V. Flambaum, Eur. Phys. J. **163**, 159 (2008).

[122] J.-P. Uzan, Rev. Mod. Phys. **75**, 403 (2003).

[123] S. K. Lamoreaux and J. R. Torgerson, Phys. Rev. D **69**, 121701 (2004).

[124] C. Chin, V. V. Flambaum, and M. G. Kozlov, New J. Phys. **11**, 055048 (2009).

[125] C. Chin and V. V. Flambaum, Phys. Rev. Lett. **96**, 230801 (2006).

[126] M. Murphy *et al.*, Science **320**, 1611 (2008).

[127] C. Henkel *et al.*, A & A **500**, 725 (2009).

[128] D. DeMille *et al.*, Phys. Rev. Lett. **100**, 043202 (2008).

[129] S. Kotochigova, T. Zelevinsky, and J. Ye, Phys. Rev. A **79**, 012504 (2009).

[130] M. Gacesa, P. Pellegrini, and R. Côté, Phys. Rev. A **78**, 010701 (2008).

[131] M. Junker *et al.*, Phys. Rev. Lett. **101**, 060406 (2008).

[132] R. Napolitano *et al.*, Phys. Rev. Lett. **73**, 1352 (1994).

[133] R. Côté, A. Dalgarno, and M. J. Jamieson, Phys. Rev. A **50**, 399 (1994).

[134] I. D. Prodan *et al.*, Phys. Rev. Lett. **91**, 080402 (2003).

[135] R. Côté and A. Dalgarno, Phys. Rev. A **58**, 498 (1998).

[136] M. Theis *et al.*, Phys. Rev. Lett. **93**, 123001 (2004).

[137] J. Herbig *et al.*, Science **301**, 1510 (2003).

[138] M. Mark *et al.*, Europhys. Lett. **69**, 706 (2005).

[139] B. H. Bransden and M. R. C. McDowell, *Charge exchange and the theory of ion-atom collisions* (Oxford University Press, New York, 1992).

[140] J. B. Delos, Rev. Mod. Phys. **53**, 287 (1981).

[141] E. E. Nikitin, Adv. Quantum Chem. **5**, 135 (1970).

[142] S. Petrie and D. Bohme, Mass Spectrom. Rev. **26**, 258 (2007).

[143] C. Harel and A. Salin, J. Phys. B **10**, 3511 (1977).

[144] R. McCarroll and R. D. Piacentini, J. Phys. B **3**, 1336 (1970).

[145] E. W. Weisstein, Prolate Spheroidal Coordinates. From MathWorld–A Wolfram Web Resource.

[146] C. Flammer, *Spheroidal wave functions* (Stanford University Press, USA, 1957).

[147] P. Falloon, P. Abbott, and J. Wang, J. Phys. A **36**, 5477 (2003).

[148] E. Leaver, J. Math. Phys. **27**, 1238 (1986).

[149] R. Soummer, C. Aime, and P. Falloon, A & A **397**, 1161 (2003).

[150] J. D. Power, Philos. Trans. R. Soc. London, Ser. A **274**, 663 (1973).

[151] E. Hylleraas, Z. Phys. **71**, 739 (1931).

[152] G. Jaffe, Z. Phys. **87**, 535 (1934).

[153] B. Judd and J. Hougen, Phys. Today **29**, 64 (1976).

[154] S. Sung and D. Herschbach, J. Chem. Phys. **95**, 7437 (1991).

[155] L. Ponomarev and T. Pusynina, Zh. Eksp. Teor. Fiz. **52**, 1723 (1967).

[156] I. Komarov, L. Ponomarev, and Y. S. Slavyanov, *Spheroidal and Coulomb spheroidal functions* (Nauka, Moscow, 1976).

[157] D. Abramov and S. Slavyanov, J. Phys. B **11**, 2229 (1978).

[158] M. Klaus, J. Phys. A **16**, 2709 (1983).

[159] T. Kereselidze, Z. Machavariani, and I. Noselidze, J. Phys. B **31**, 15 (1998).

[160] R. Piacentini and A. Salin, J. Phys. B **7**, 1666 (1974).

[161] R. E. Olson and A. Salop, Phys. Rev. A **14**, 579 (1976).

[162] A. Salop and R. E. Olson, Phys. Rev. A **19**, 1921 (1979).

[163] C. Harel, H. Jouin, and B. Pons, At. Data Nucl. Data Tables **68**, 279 (1998).

[164] J. B. Hasted, S. M. Iqbal, and M. M. Yousaf, J. Phys. B **4**, 343 (1971).

[165] E. Solov'ev, J. Phys. B **38**, R153 (2005).

[166] P. F. Falloon, Ph.D. thesis, University of Western Australia, 2001.

[167] R. Pepino *et al.*, ApJ **617**, 1347 (2004).

[168] D. Koutroumpa *et al.*, A&A **460**, 289 (2006).

[169] I. P. Robertson *et al.*, Eos Trans. AGU, 89(53), Fall Meet. Suppl. **89**, B1596+ (2008).

[170] R. Lallement *et al.*, Science **307**, 1447 (2005).

[171] D. B. Henley and R. L. Shelton, ApJ **676**, 335 (2008).

[172] H. Tanuma *et al.*, J. Phys. B **33**, 5091 (2000).

[173] V. Kharchenko, W. Liu, and A. Dalgarno, J. Geophys. Res. **103**, 26687 (1998).

[174] V. Kharchenko and A. Dalgarno, J. Geophys. Res. **105**, 18351 (2000).

[175] U. Fano and J. H. Macek, Rev. Mod. Phys. **45**, 553 (1973).

[176] H. Müller, G. P. Zank, and A. S. Lipatov, J. Geophys. Res. **105**, 27419 (2000).

[177] G. P. Zank and P. C. Frisch, ApJ **518**, 965 (1999).

[178] N. A. Schwadron and T. E. Cravens, ApJ **544**, 558 (2000).

[179] D. Koutroumpa *et al.*, ApJ **697**, 1214 (2009).

[180] E. J. Smith *et al.*, Science **302**, 1165 (2003).

[181] H.-R. Müller *et al.*, ApJ **647**, 1491 (2006).